

Spin Polarization Dynamics in Perovskite Nanocrystals

Simone Strohmail

München 2023



Spin Polarization Dynamics in Perovskite Nanocrystals

Dissertation

to obtain the doctoral degree of natural sciences (Dr. rer. nat.)



at the Faculty of Physics
of the Ludwig-Maximilians-Universität München

submitted by

Simone Strohmail

from Munich

Munich, 10 October 2023

First referee: Prof. Dr. Jochen Feldmann
Second referee: Prof. Dr. John Lupton
Chairman: PD Dr. Bert Nickel
Further member: Prof. Dr. Jan von Delft

Date of oral examination: 23 November 2023

Spinpolarisationsdynamiken in Perowskit Nanokristallen

Dissertation

zur Erlangung des Doktorgrades der Naturwissenschaften (Dr. rer. nat.)



an der Fakultät für Physik
der Ludwig-Maximilians-Universität München

vorgelegt von

Simone Strohmar

aus München

München, 10. Oktober 2023

Erstgutachter:	Prof. Dr. Jochen Feldmann
Zweitgutachter:	Prof. Dr. John Lupton
Vorsitzender:	PD Dr. Bert Nickel
Beisitzer:	Prof. Dr. Jan von Delft

Tag der mündlichen Prüfung: 23. November 2023

Publications and Conferences

Scientific Publications of Results Presented in this Work

- S. Strohmair, A. Dey, Y. Tong, L. Polavarapu, B. J. Bohn and J. Feldmann
Spin Polarization Dynamics of Free Charge Carriers in CsPbI₃ Nanocrystals
Nano Letters 20(7), 4724-4730 (2020)
- A. Dey, S. Strohmair, F. He Q. A. Akkerman and J. Feldmann
Fast electron and slow hole spin relaxation in CsPbI₃ nanocrystals
Appl. Phys. Lett. 121, 201106 (2022)

Additional Publications

- M. Kurashvili, I. Polishchuk, A. Lang, S. Strohmair, A. F. Richter, S. Rieger, T. Debnath, B. Pokroy and J. Feldmann
Disorder and Confinement Effects to Tune the Optical Properties of Amino Acid Doped Cu₂O Crystals
Adv. Funct. Mater. 32, 2202121 (2022)

Contributions to Conferences and Workshops

- *CeNS Workshop Venice 2018: Celebrating NanoScience* (Poster)
Venice, Italy, September 2018
- *7th International SolTech Conference* (Poster)
Würzburg, Germany, October 2018
- *Workshop on Optical Spectroscopy of New Materials 2019* (Talk)
Haigerloch, Germany, March 2019
- *20th International Conference on Physics of Light-Matter Coupling in Nanostructures: PLMCN20* (Invited Talk)
Moscow and Suzdal, Russia, July 2019
- *8th International SolTech Conference* (Talk)
Nürnberg, Germany, September 2019
- *Internet Conference for Quantum Dots: iCQD* (Talk)
July 2020

Zusammenfassung

Seit dem kürzlichen Aufkommen von kolloidalen Blei-Halogenid Perowskit Nanokristallen (LHP NCs) begeistern sie die Branche durch ihre faszinierenden optischen Eigenschaften. Sie besitzen daher großes Potenzial optische Anwendungen wie Strahler, Solarenergiekollektoren und Spintronik zu reformieren. CsPbI_3 , eine anorganische Verbindung unter LHPs, zeigt besonders ausgeprägte Spin-Bahn-Kopplung, was zu signifikanter Feinstrukturspaltung und folglich zu lediglich zweifach entarteten Valenz- (VB) und Leitungsbändern (CB) führt. Hierdurch bestehen perfekte Bedingungen für maximal effiziente optische Spinausrichtung (oS), wobei Ladungsträger durch zirkular polarisierte Strahlung in bekannte VB- und CB-Zustände angeregt werden. Im Gegensatz dazu stehen konventionelle II-VI und III-V Halbleiter, worin sich dieselben auf mehrere VB- und CB-Zustände aufteilen, was die erreichbare oS um 50% gegenüber LHPs verringert. Das Potenzial der enormen Induktion von zirkularem Dichroismus in CsPbI_3 und dessen Vielzahl an faszinierenden optischen Eigenschaften macht diese Verbindung zu einem Modellsystem für fundamentale Spinforschung. Das Wissen über Spindynamiken von Ladungsträgern ist ausschlaggebend für ein grundlegendes Verständnis elektronischer Prozesse in dieser Materialklasse.

In dieser Arbeit wird die Dynamik von Ladungsträger-Spinrelaxation (LSR) und dessen zugrundeliegenden theoretischen Mechanismen mittels zeitaufgelöster differentieller Transmissionspektroskopie (DTS) beleuchtet. Dabei stellt sich heraus, dass die intrinsisch achiralen NCs beträchtlichen zirkularen Dichroismus kurz nach Anregung durch zirkular polarisierte Laserpulse aufweisen. Darauf folgende LSR gleicht das präparierte Spin-Ungleichgewicht aus. Energetischere optische Anregung bewirkt ein Abkühlen der Ladungsträger zur Bandlücke durch Phononenemission. Dabei entsteht eine große Nicht-Gleichgewichts-Phononenpopulation, welche den Wirkungsquerschnitt der Ladungsträger-Phononenstreuung vergrößert. Der Elliott-Yafet- (EY) Mechanismus, den ich der maßgeblichen LSR in CsPbI_3 zuordne, besagt, dass LSR durch Ladungsträger-Phononenstreuung erfolgt. Die gemessene Ensemble-Spinpolarisation verringert sich dementsprechend erheblich mit erhöhter LSR während des Abkühlvorgangs der Ladungsträger. Temperaturabhängige DTS offenbart, dass die LSR-Geschwindigkeit bei Raumtemperatur derer bei kryogenen Temperaturen um eine Größenordnung übersteigt. Entsprechende Raten enthüllen einen klaren und adequaten Zusammenhang jeweils zur Phononenbesetzung und EY-Funktionalität. Der Entzug von Elektronen aus den CsPbI_3 NCs durch Beimischung eines Elektron-Absorbermoleküls erlaubt die fast ausschließliche Beobachtung der Loch-Spinrelaxation, welche sich als langsamer, als die der Elektronen erweist.

Abstract

Recently, colloidal lead halide perovskite nanocrystals (LHP NCs) have emerged and impress the community with their intriguing optical properties ever since. They demonstrate great potential to reform optical applications such as light emitting devices, solar energy harvesting and spintronics. Among LHPs, the all-inorganic compound CsPbI₃ exhibits particularly strong spin-orbit coupling, leading to significant fine structure splitting, which makes both, valence (VB) and conduction band (CB) only two-fold degenerate. This renders perfect conditions for maximally efficient optical orientation, whereupon charge carriers are excited into precisely known VB and CB states by circularly polarized radiation. This is in contrast to conventional II-VI and III-V semiconductors, where circularly photoexcited charge carriers are distributed among multiple VB and CB states, dropping their maximally achievable optical orientation by as much as 50% compared to LHPs. The potential of photoinducing tremendous circular dichroism into CsPbI₃ NCs through optical orientation, in combination with their multiplicity of intriguing optical properties, make them a model system for fundamental spin studies. The knowledge about the spin dynamics of charge carriers is crucial for a profound comprehension of electronic processes in this material class.

In this thesis, charge carrier spin polarization dynamics and underlying theoretical mechanisms are elucidated in colloidal CsPbI₃ NCs by employing time-resolved differential transmission spectroscopy (DTS). Thereby, the intrinsically achiral NCs are found to exhibit considerable circular dichroism shortly after excitation with a circularly polarized laser pulse. Subsequent charge carrier spin relaxation equilibrates the prepared spin imbalance. Elevated photoexcitation energy causes charge carriers to cool down to the band gap via phonon emission. Thereby, a large non-equilibrium phonon population develops, increasing the carrier-phonon scattering cross-section. The Elliott-Yafet (EY) mechanism, which I assign to govern spin relaxation in CsPbI₃ NCs, predicts that spin relaxation is a consequence of carrier-phonon scattering. Accordingly, the investigated ensemble spin polarization is measured to diminish significantly in the process of carrier cooling at an increased spin relaxation rate. Temperature-dependent DTS reveals that room temperature spin relaxation dynamics are one order of magnitude faster than at cryogenic temperatures. The corresponding rates reveal a clear and adequate correlation to phonon occupation and EY functionality, respectively. The removal of electrons from the CsPbI₃ NCs through admixture with an electron scavenger molecule permits the almost exclusive investigation of hole spin relaxation, which is revealed to occur slower compared to that of electrons.

Table of Contents

Zusammenfassung	vii
Abstract	ix
1 Introduction	1
2 Fundamentals	5
2.1 Lead Halide based Perovskites	5
2.1.1 Different Kinds and their Properties	6
2.1.2 CsPbI ₃ Crystal Structure and Symmetry	12
2.1.3 Electronic Band Structure	13
2.2 Light-Matter Interaction	19
2.2.1 Optical Absorption	19
2.2.2 Polarization of EM Waves and Photons	26
2.2.3 Selection Rules and Optical Orientation	30
2.3 Carrier-Phonon Coupling	33
2.4 Carrier Spin Relaxation in Semiconductors	41
2.5 Elliott-Yafet Spin Relaxation Theory	47
3 Materials and Experimental Methods	55
3.1 Sample Preparation	55
3.1.1 Synthesis of CsPbI ₃ Nanocubes	55
3.1.2 Mixing of CsPbI ₃ Nanocubes with PCBM	56
3.2 Linear Optical Spectroscopy	58
3.2.1 Absorption and Photoluminescence Spectroscopy	58

3.2.2	Polarization Dependent Spectroscopy	59
3.3	Differential Transmission Spectroscopy	62
4	Optical Characterization of CsPbI₃ Nanocubes	69
4.1	Static Absorption and Photoluminescence Spectra	70
4.2	Circularly Polarized Optical Spectra	72
4.3	Recombination Dynamics	73
5	Spin Relaxation in CsPbI₃ Nanocubes	75
5.1	Spin Relaxation Dynamics of Free Charge Carriers	75
5.2	The Role of Excitation Intensity	81
5.3	How LO Phonon Absorption and Emission Contributes to Spin Relaxation	84
5.3.1	The Role of Excess Energy	84
5.3.2	Freezing Out Phonon Scattering and Spin Relaxation	89
6	Distinction between Electron and Hole Spin Relaxation	99
6.1	Spin-Independent Characterization of CsPbI ₃ NCs versus CsPbI ₃ NC : PCBM	100
6.2	Extraction of Individual Spin Relaxation Rates for Electrons and Holes . . .	104
7	Summary and Conclusion	109
	References	I
	Appendix	XIII
A.1	Appendix A	XIII
A.2	Appendix B	XIII
	List of Figures	XVIII

List of Tables	XIX
List of Abbreviations	XXI
Acknowledgments	XXIII

CHAPTER 1

Introduction

Conventional charge based semiconductor applications have been highly successful, as testified by their impressive modern computing power and their omnipresence in our daily lives. Their persistent development and growth in popularity, however, concomitantly introduces new challenges. One challenge is that they have nearly reached their physical limits.¹ An indication for that is their continuously increasing lag behind Moore's "law", an empirical prediction that the transistor density on a computer chip doubles every two years. The reason for this are problems arising when downsizing transistors, such as large power dissipation due to enlarged leakage currents.^{2,3} Another challenge is to conjointly target both, a rising global energy consumption and intensifying environmental concerns. This could succeed for example through the use of electronics with improved energy efficiencies.^{1,4-6} This naturally brings the focus to spintronics, or spin-based electronics, which is the interconnection of information technology with quantum mechanics. Fundamental research in this field is concerned with spin generation, manipulation, and transport within applicable materials.⁷ In conventional semiconductor electronics information is carried by an electron's / hole's charge,⁸ while their spin properties have been mostly disregarded so far. Their spin properties, however, bear great potential to revolutionize a wide field of information technology, as spintronic applications target low power consumption, high-density and non-volatile memory and storage, as well as fast data processing.^{7,9,10} Actualizing spintronics in semiconductors would have the unique advantage of uniting the strengths of both, spintronics and the proven power of semiconductor logic, while addressing today's urgent challenges mentioned above. Moreover, semiconductor spintronics provides an interface to convert spin quantum information to photons and vice

versa. Charge-based and spin-based technology are thus compatible through spin-photon interfaces, enabling mutual data communication.^{11–13} Therefore, semiconductor spintronics bears the power of modernizing contemporary classical semiconductor information technology through both, its substitution and enrichment. Spintronic systems find their application furthermore in potentially ground-breaking fields, such as neuromorphic computing and quantum computing. The former aims for innovative hardware that is inspired by the brain, enabling energy efficient, fast, and sophisticated computation.¹⁴ The latter targets quantum information processing by utilizing entanglement and superposition of spin states, properties, which are not available to classical charge states.

Research in the field of spintronics finds its origin in 1988, when the Nobel Prize winners Albert Fert and Peter Grünberg¹⁵ discovered giant magnetoresistance (GMR).² Briefly, GMR describes the strong influence of parallel or antiparallel magnetization on the conductivity across a layered ferromagnetic/ non-magnetic structure. This discovery enabled efficient control of electric current with magnetization that revolutionized the technology of magnetic storage devices.¹¹ The work of Nobel Prize winner Alfred Kastler (1950) and Lampel (1968) founded a technique of spin injection that was and is of great importance in the field of spintronics: optical orientation.^{10,11,16} Optical orientation relates to the induction of a defined spin distribution within a material through photons. An alternative approach is electrical spin injection. The former, however, has demonstrated to be advantageous in some cases, as evidenced by the following examples. The speed of magnetization reversal with circularly polarized femtosecond light pulses, which is utilized for magneto-optical data storage, was reported in 1996 to be much faster than magnetization switching through electrical spin generation. In 2019, single pulse magnetization reversal has been demonstrated, paving the way to a next level of speed and energy efficiency in magnetic storage.⁹

A semiconductor material that has gained increasing attention throughout the last decade is lead halide perovskite (LHP). In particular, colloidal LHP nanocrystals (NCs) exhibit advantageous optical properties: a large absorption cross section,^{17,18} high photo- and electroluminescence emission quantum yields,^{19,20} as well as favourable charge carrier transport properties, such as large diffusion lengths.^{21–24} The synthesis is facile and inexpensive, as LHPs are solution and low-temperature processable.^{20,25–27} Their bandgap energies, and thus absorption and emission wavelengths, are highly tunable over the entire visible spectrum through compositional modulations of the halide ion, as well as through quantum confinement by a reduction of the NC size.^{20,28–32} In particular, LHPs exhibit strong spin-orbit coupling (SOC), which is a prerequisite for vigorous optical orientation.^{33–36} Furthermore, their in-

verted band structure compared to conventional semiconductors³⁶ allows for a theoretical 100% optical spin generation as opposed to 50% theoretical maximal optical orientation in the widely-used II-VI and III-V semiconductors.^{37,38} The multiplicity of interesting properties of LHPs make them appealing model systems for semiconductor spintronics³⁶ and fundamental spin studies.^{39,40} They are proposed to be extremely promising as spin-field effect transistor devices,³⁹ or spin photovoltaic applications^{1,40} and have been demonstrated as spin-light emitting diodes.⁴¹ For the use of LHPs in the field of spintronics, a profound comprehension about optical orientation and the spin dynamics obeyed by photoexcited charge carriers within these materials is essential, as it enables one to adjust the physical framework, e.g. temperature, pressure, material composition, and more, in order to achieve suiting material properties for a desired spintronic application.⁴² Nonetheless, contemporary research about spin phenomena in LHPs is still at an early stage.

In this work, charge carriers in CsPbI₃ perovskite NCs are optically oriented through helical ultra-short laser pulses and their subsequent spin dynamics are investigated. Chapter 2 covers the theoretical background of performed experiments and data evaluation. Polarization dependent, time-resolved DTS allows a precise detection of photoinduced spin imbalance and its decay. Chapter 3 describes the corresponding experimental setup and its working principle, alongside with that of linear (polarization dependent) spectroscopy and the procedure of sample preparation. Chapter 4 reveals emission and absorption properties of the CsPbI₃ NCs via PL- and (temperature dependent) linear absorption spectra, respectively. Moreover, the circular dichroism spectrum manifests the NC's achirality and DTS clarifies that recombination dynamics are independent of laser helicity and thus of intrinsic spin polarization. Chapter 5 displays and discusses the results of diverse DTS measurements, e.g. with excitation energy or temperature dependency. Furthermore, the reader is guided through their careful evaluation, which comprises of the use of rate equations and theoretical spin relaxation models. As the latter are based on distinct microscopic origins for spin relaxation, as outlined in Chapter 2, their assignment to the data leads to the discovery that spin relaxation of free charge carriers occurs via longitudinal optical (LO) phonon scattering and manifests that the Elliott-Yafet mechanism governs spin relaxation in CsPbI₃ NCs. With the aim of investigating spin dynamics of electrons and holes individually, Chapter 6 shows the spectral examination of the admixture of CsPbI₃ NCs with the electron scavenger molecule PCBM. The DTS spectra precisely follow appropriate rate equations, which allows to draw the conclusion that hole spin relaxation is slower than that of electrons. I finalize this thesis by summarizing all findings and offering my conclusions in Chapter 7. At last, I finish with an outlook on further interesting investigations and promising future applications.

CHAPTER 2

Fundamentals

2.1 Lead Halide based Perovskites

“Perovskite” identifies a crystal family with ABX_3 stoichiometry.²⁷ Already in 1839 Gustav Rose discovered the naturally occurring oxide perovskite $CaTiO_3$.⁴³ The pioneering report about synthetic, inorganic metal halide perovskites (including $CsPbI_3$) was published in 1893 by Wells.⁴⁴ The rich colours of these synthetic compounds inspired Møller to study their electronic properties in 1958, unravelling that they exhibit photoconductivity.⁴⁵ More than half a century elapsed until the great potential of halide perovskites was recognized for optoelectronic applications. It was their use as semiconducting photoactive layer for photovoltaic cells in 2009,⁴⁶ which sparked tremendous interest in these materials, leading to a still ongoing cascade of publications.^{27,47} Today, synthetic metal halide based perovskites are at the forefront of contemporary research and have been investigated for various technological fields. The most prominent applications are solid-state light emitters (light-emitting diodes (LEDs) and lasers),⁴⁸ light absorber ((tandem) solar cells,^{49–51} photocatalysis,⁵² (flexible) photodetectors^{53–55}), light converters (visible light communication⁵⁶), as well as transistors⁵⁷ and gas sensors⁵⁴.

2.1.1 Different Kinds and their Properties

The chemical stability of perovskites is subject to the ionic radii of its constituents.²⁷ This entails a constrained selection of A-,B- and X-site components. In metal trihalide perovskites (MHPs), A and B are monovalent and divalent cations, respectively, while X is a monovalent anion, i.e. A^+ , B^{2+} , X^- . The basic metal lead (Pb) fulfils the B-site requirements and institutes the category lead-based MHPs, i.e. lead trihalide perovskites (LHPs), which I want to focus on in this work. Within this category, hybrid organic-inorganic and all-inorganic LHPs are differentiated. The former have an organic A-site molecule, such as methylammonium (CH_3NH_3) or formamidinium ($HC(NH_2)_2$), while the latter have the inorganic alkali metal caesium (Cs) at the A-site. Halides like chlorine (Cl), bromine (Br) or iodine (I) fit the X-site criteria. Figure 2.1 a shows the spatial arrangement of the A (turquoise), Pb (gray), and X-site (purple) ions in a cubic representation of the perovskite crystal lattice. The high symmetry points Γ , M, X and R in its first Brillouin zone in reciprocal space is shown in Figure 2.1 b.^{58,59} Regarding the electronic properties, LHPs are semiconductors and contain a band gap defined by the upper VB and the lower CB. A theoretical calculation of the electronic band structure of $CsPbI_3$ across the high symmetry points is displayed in Figure 2.1 c.⁵⁸ The band gap is located at the R point. Band gap energy, E_g , and spin-orbit splitting, Δ_{SO} , are indicated.

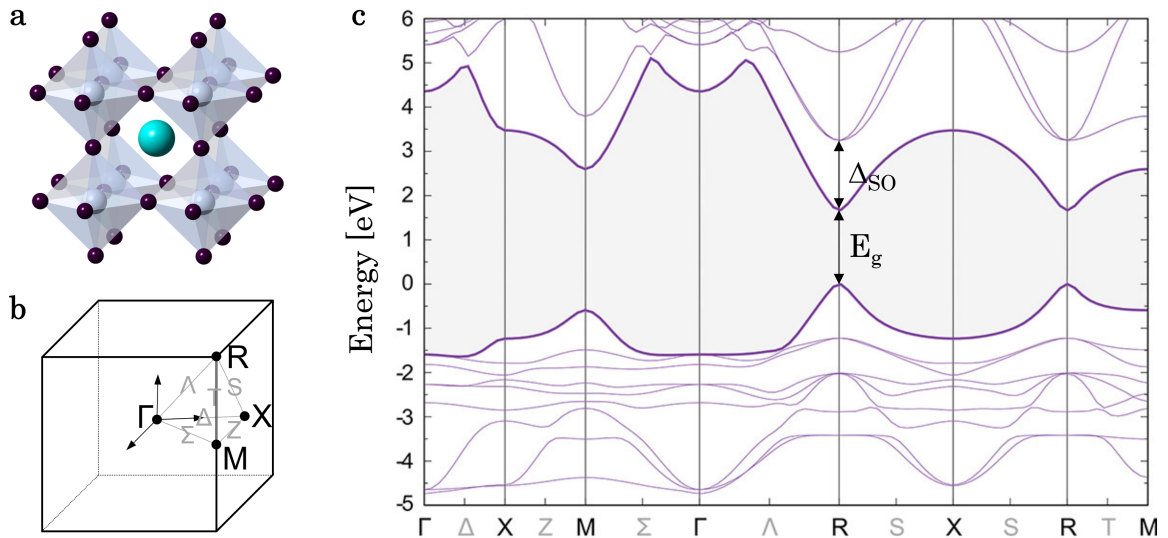


Figure 2.1: Cubic $APbX_3$. (a) Crystal structure. Turquoise, gray and purple spheres represent A-, Pb- and X-site ions, respectively. X-site ions span gray shaded octahedra, each enclosing one Pb cation. Every A-site cation is surrounded by 12 nearest halogen anions forming a cuboctahedral cage. (b) First Brillouin zone corresponding to (a) and its high symmetry points Γ , M, X and R, located at the respective coordinates $(0,0,0)$, $(\frac{1}{2}, \frac{1}{2}, 0)$, $(0, \frac{1}{2}, 0)$, and $(\frac{1}{2}, \frac{1}{2}, \frac{1}{2})$. (c) Calculated band structure of cubic $CsPbI_3$. Adopted⁵⁸ and adjusted.

Valence and conduction bands form due to hybridization of lead and halide outer atomic orbitals. The upper VB arises from Pb 6s and X np orbitals ($n = 3, 4, 5$ for X = Cl, Br, I, respectively), while the lower CB is predominantly generated by Pb 6p orbitals with a small admixture of X np orbitals.^{20,34,60} The band gap energy, E_g , in LHPs is therefore determined by the $(\text{PbX}_6)^{4-}$ octahedra and thus by the choice of halide anion.⁶¹ It decreases with rising halide atomic number, which is mainly a result of an energetic upshift of the VB. Thus, substitution of the halide anion enables band gap tuning, covering the entire visible spectrum.^{20,25,28,29}

LHP NCs, i.e. nanometer-sized monodisperse colloidal perovskite single-crystals, are achieved through colloidal synthesis, where organic ligands are used to control their size and morphology.⁶² LHPs in form of colloidal NCs exhibit some unique properties in contrast to their bulk and film counterparts: their photoluminescence quantum yield (PLQY) is intensely improved, making them interesting for light emitting applications.^{63,64} Moreover, NCs may be self-assembled into helical structures⁶⁵ or equipped with chiral ligands⁶⁶ to exhibit circular dichroism (CD) and circular photoluminescence (CPL) at the perovskite's band gap, which might be interesting for chiral optoelectronic and spintronic applications. LHP NCs exhibit the same crystal structure as their bulk and film counterparts, but may be synthesized with different morphologies, such as nanocubes, nanoplatelets, or nanowires,^{67,68} and tuned in size with supreme precision^{25,30,69}. This tunability of shape and size entails modifications in band gap, exciton binding energy and surface defects,^{28,30,32,69} which again affect various optoelectronic properties, such as the cooling and recombination rate of photoexcited charge carriers,⁷⁰ as well as absorption and emission spectra³⁰. The dependence of the optical properties on the NC size is a consequence of quantum confinement:⁷¹ Upon NC shrinkage, the band gap increases and, synonymously, the spectra blue-shift.⁷² Thus, the NC dimensions represent an additional parameter for precise colour tunability alongside with compositional modulation of the halide anion as mentioned above. To be precise, it is the kinetic energy E_{qc} of an otherwise free particle, which is most notably increased by quantum confinement. In a cube shaped NC with edge lengths L quantum confinement can be modelled by a 3D infinite quantum well (QW) with widths L. Otherwise free, non-interacting electron and hole within such a QW are described by the following Hamiltonian and ground state wave function,^{38,72,73}

$$\hat{H}_{QW} = \frac{\hat{p}_e^2}{2m_e^*} + \frac{\hat{p}_h^2}{2m_h^*}, \text{ which in position space reads } H_{QW} = -\frac{\hbar^2}{2m_e^*} \vec{\nabla}_e^2 - \frac{\hbar^2}{2m_h^*} \vec{\nabla}_h^2$$

$$\psi(x, y, z) = \psi_e(x, y, z) \psi_h(x, y, z), \text{ where } \psi_{e/h}(x, y, z) = \left(\frac{2}{L}\right)^{\frac{3}{2}} \cos\left(\frac{\pi}{L}x\right) \cos\left(\frac{\pi}{L}y\right) \cos\left(\frac{\pi}{L}z\right),$$
(2.1)

with the QW centred around the origin. The ground state eigenenergy of this system is found by solving the Schrödinger equation

$$\begin{aligned} H_{QW} \psi(x, y, z) &= E_{qc} \psi(x, y, z) \\ \Rightarrow E_{qc} &= \frac{3\pi^2 \hbar^2}{2m_e^* L^2} + \frac{3\pi^2 \hbar^2}{2m_h^* L^2}. \end{aligned} \quad (2.2)$$

From Equation 2.2 it can be seen, that a systematic reduction of NC size leads to an increase of confinement energy ($\propto L^{-2}$), which is responsible for the aforementioned band gap widening and correlated spectral blue-shift.

Electrons and holes have so far been regarded as free, non-interacting particles in the QW. However, it must be considered that they are oppositely charged and thus subject to an attractive Coulomb force acting between them. A bound electron-hole pair can be therefore described as a quasiparticle called exciton. Taking the Coulomb interaction between electron and hole into account, the Hamiltonian in Equation 2.1 must be equipped with the potential energy of the corresponding Coulomb field (third term in Equation 2.3).^{72,73}

$$\hat{H}_X = \frac{\hat{p}_e^2}{2m_e^*} + \frac{\hat{p}_h^2}{2m_h^*} - \frac{e^2}{4\pi \epsilon_{r,\text{eff}} \epsilon_0 |\hat{r}_e - \hat{r}_h|} \quad (2.3)$$

As a result of the high relative dielectric permittivity, $\epsilon_{r,\text{eff}}$ (= relative dielectric function (real part) $\epsilon_r(\omega)$ at specific frequency ω corresponding to the exciton), in LHPs, the associated excitons are of Wannier-Mott type, i.e. they extend over many lattice constants and their Coulombic binding energies are comparably small.⁶⁰

It is this distance between the electron and hole in the third term of Equation 2.3, which gives rise to the differentiation of two regimes: the weak and the strong confinement regime.^{72,73}

The weak confinement regime classifies NCs with large enough dimensions such that the electron-hole relative motion is “undisturbed” in a sense that it is not subject to size quantization.^{72,73} That is the case when L exceeds a_X , where a_X is roughly the size of the exciton (see the definition in Equation 2.5). The electron-hole relative motion can therefore be described in terms of the hydrogen atom. Hence, their Coulomb interaction manifests itself in the exciton binding energy, B_X , and likewise the exciton Rydberg, Ry_X ,

$$B_X = \frac{Ry_X}{n^2}, \quad \text{with } Ry_X = \frac{\mu}{m_0 \epsilon_{r,\text{eff}}^2} Ry_H = \frac{\hbar^2}{2\mu a_X^2}, \quad (2.4)$$

where n is the exciton principle quantum number, Ry_H the Hydrogen Rydberg, $\frac{1}{\mu} = \frac{1}{m_e^*} + \frac{1}{m_h^*}$ the reduced effective mass of the electron-hole system, m_0 the free electron mass and a_X the exciton Bohr radius⁷⁴

$$a_X = \frac{m_0 \varepsilon_{r,\text{eff}}}{\mu} a_H = \frac{4\pi\varepsilon_0 \varepsilon_{r,\text{eff}} \hbar^2}{\mu e^2}. \quad (2.5)$$

a_H stands for hydrogenic Bohr radius and e for elementary charge. Synonymous with Ry_H , Ry_X is the ground state and ionization energy of the exciton. A general pattern among LHPs can be noticed, namely that Ry_X tends to increase with the inverse of the atomic mass of the halide anion, i.e. Ry_X tends to increase as the band gap increases.^{20,75} Incidentally, the same trend is present in direct gap III–V and II–VI semiconductors.⁷⁴

Unlike the electron-hole relative motion, the exciton center-of-mass motion is subject to quantum confinement in the weak confinement regime. The exciton as a whole, with its mass $M_X = m_e^* + m_h^*$ is thus the particle inside the above considered potential well. Analogous to the above calculation, the exciton gains additional kinetic energy due to quantum confinement. The total exciton energy relative to the band gap in the weak confinement regime, is therefore^{72,73}

$$E_X^{\text{weak}} = E_g + \frac{3\pi^2 \hbar^2}{2M_X L^2} - B_X. \quad (2.6)$$

On the contrary, the strong confinement regime classifies NCs with edge lengths L undercutting a_X . In this regime, single carrier confinement effects are significant and the relative motion of an electron-hole pair is not correlated any more.⁷³ Therefore, these excitons cannot be described in terms of the hydrogen atom. Spatial confinement forces electron and hole within the NC dimensions and thus dictates their interspace. Consequently the attractive Coulomb interaction between them is increased.⁷⁶ The total exciton energy relative to the band gap in the strong confinement regime can be calculated to be^{72,73}

$$E_X^{\text{strong}} = E_g + \frac{3\pi^2 \hbar^2}{2\mu L^2} - 3.05 \frac{e^2}{\varepsilon_{r,\text{eff}} L}. \quad (2.7)$$

The NCs used in the scope of this thesis do not fall under the strong confinement regime, which is why I leave out details about the derivation for this expression.

Quantum confinement is significant, if the additional kinetic energy due to quantum confinement (second term in Equation 2.6 and Equation 2.7), is comparable or larger than the thermally induced kinetic energy, $E_{th} = \frac{3}{2} k_B T$, where k_B is the Boltzmann constant and T the temperature.⁷¹ Consequently, small temperature and/or small NC size promote quantum confinement effects to become significant. Similarly, if the exciton binding energy or the

attractive Coulomb interaction (third term in Equation 2.6 and Equation 2.7, respectively) exceeds E_{th} , thermal dissociation of the electron-hole pair is suppressed and stable excitons form.⁷⁴ Otherwise, a bound state between electron and hole is energetically not favoured and they remain as free charge carriers in the semiconducting LHP NC. Accordingly, small temperature and/or small NC size additionally promote the existence of stable excitons.⁷⁷

Having covered the effects of NC size and temperature on the charge carriers, let us now consider the effects of temperature on the LHP band structure. With decreasing temperature the majority of LHPs exhibit a red-shift in the band gap, i.e. a decrease in band gap energy,^{78–83} rather than a widening of the band gap as typical for most conventional semiconductors, such as Si or GaAs.⁸⁴ These opposites are proposed to have their origin in the inverted band structure of LHPs compared to that of conventional semiconductors (see Figure 2.3 and description in Subsection 2.1.3).⁷⁹ Hybrid organic-inorganic LHPs additionally undergo structural phase transitions to lower symmetry crystal structures as the temperature decreases.^{85–87} These phase transitions occur at characteristic temperatures (e.g. with decreasing temperature MAPbI₃ transitions from cubic →tetragonal →orthorhombic at ~330 K and ~160 K, respectively)⁸⁷ and appear as discontinuities in the thermal evolution of their band structure, band gap energy, dielectric permittivity and exciton binding energy. The tetragonal→orthorhombic transition is most profound, as it is accompanied with a sharp decrease/increase in dielectric screening⁸⁸/exciton binding energy, respectively,⁸⁹ alongside with a cessation of the rapidly re-orientating motion of the organic cations.^{86,87} Inorganic LHPs do not undergo phase transitions up to room temperature and thus merely show the above described typical continuous band gap shift with temperature.^{75,78} Their exciton binding energy and dielectric permittivity are meanwhile largely temperature independent. Therefore, when the rotational motion of the organic cations is frozen in the low-temperature orthorhombic phase of hybrid LHPs, the dielectric screening mechanism is suggested to be essentially the same as for hybrid and inorganic LHPs, i.e. governed by the (PbX₆)⁴⁻ octahedra.^{90,91} Indeed, calculations reveal comparable relative permittivities in the low temperature orthorhombic phase as long as the hybrid and inorganic LHPs are composed of identical halide atoms.⁷⁵ LHPs with light/heavy halide cations exhibit a low/high relative permittivity, which manifests the recognized large/small exciton binding energy, respectively.^{75,88,90}

As established above, various kinds of LHPs exist. The rich assortment of composition, morphology and size brings about individual properties, which opens the distinguished possibility to design a suitable system for the intended study. For fundamental research on

spin polarization dynamics, the topic of this thesis, the inorganic LHP NC CsPbI₃ is a model platform for the following reasons:

- Unlike hybrid LHPs, inorganic LHPs do not undergo phase transitions with temperature. This is crucial, as temperature dependent spin dynamics are extractable more unambiguously from monotonically behaved background phenomena.^{86,87} Furthermore, the inherent molecular dipole and asymmetric shape of organic cations⁹⁰ (as opposed to the spherically symmetric Cs atom) imposes a strong polarization and inversion asymmetry on the crystal lattice.⁸¹ This affects the spin dynamics of photoinduced charge carriers and thus adds a further, unwanted level of complexity.
- Among Cs-based LHPs, CsPbI₃ exhibits the smallest band gap and exciton binding energy.^{20,75} A small enough exciton binding energy, which falls below the thermal energy, allows the study of free charge carriers, which is preferred with respect to excitons for two reasons: First, this work aims to generate a profound depiction of spin phenomena, which is most fundamental for free electrons and holes compared with the more complex excitons, being a coalition of both. Second, free charge carriers are highly relevant for optoelectronic applications, such as for example energy harvesting, because only dissociated electrons and holes form harvestable current.⁸⁹ Therefore, despite almost always neglected, knowledge about the spin dynamics of photoexcited free charge carriers is crucial for a more profound comprehension of the intrinsic electronic processes and might inspire improved or even novel optoelectronic applications.
- For the same reasons, the NCs used in the scope of this thesis are prepared with a size large enough to avoid considerable size quantization and thus without enhancement of the exciton energy. Hence, nanocubes with relatively long edge lengths are chosen. These can be described within the weak confinement regime and exhibit just about bulk-like optical properties. As a side note, although bulk-like characteristics are required, NCs were chosen over bulk or film CsPbI₃, because the latter adopt the photoinactive yellow non-perovskite crystal phase at ambient and low temperatures.^{92,93} Through post-synthetic heat treatment the desired photoactive black perovskite phase can be achieved, however, it is rather unstable and reverts to the yellow phase within $\sim 1 - 48h$.^{92,94} CsPbI₃ NCs on the other hand exhibit superior thermal and chemical stability, even under humid conditions,⁹⁵ and remain photoactive for roughly two months, when stored in ambient conditions.²⁵ A long intactness is beneficial for experimental measurements and crucial for commercial applications.

On the basis of these considerations, colloidal CsPbI₃ NCs emerge as a model platform to gain fundamental knowledge about spin polarization dynamics of photoinduced charge carriers. Hereinafter, the covered content will therefore refer to colloidal CsPbI₃ NCs, unless specified otherwise.

2.1.2 CsPbI₃ Crystal Structure and Symmetry

Nanocrystals are crystalline nanoparticles, i.e. their atoms are arranged in a near-perfect periodic manner.^{25,96} Consequently, a specific set of symmetry operations, like rotation, inversion, reflection, translation, and combinations of these exist, which map the crystal pattern onto itself and leave it invariant.^{97,98} This specific set is dictated by the crystal pattern and forms a symmetry group, which is called space group in the three-dimensional case. Hence, a crystal can be classified into one of 230 crystallographic space-group types with a unique combination of symbol¹ and number, as given in brackets below. All space groups are again coarsely classified into seven crystal systems, whereof the cubic, tetragonal and orthorhombic crystal systems will be encountered in this work. Depending on temperature and composition, perovskites can embody those three crystal systems, which are designated as α -, β -, and γ -/ δ - phases, respectively.⁷² Although both, γ - (Pbnm, No. 62) and δ - (Pnma, No. 62) phases, are orthorhombic, the latter is a yellow non-perovskite phase, which is photoinactive and thus unwanted for my purposes or any optoelectronic applications. α -, β -, and γ - phases on the other hand are the desired black photoactive perovskite phases. The crystal structure of cubic α -CsPbI₃ (Pm $\bar{3}$ m, No. 221) has already been shown in Figure 2.1 a. Its analogue with slightly rotated (PbX₆)⁴⁻ octahedra represents a distortion of the cubic phase and is described by the lower symmetry tetragonal β -phase (P4/mbm, No. 127). An additional tilt perpendicular to the rotation axis of the (PbX₆)⁴⁻ octahedra, further breaks the symmetry and results in the orthorhombic γ - perovskite phase (Pbnm, No. 62). All of the mentioned space groups have an inversion center as one of their symmetry points and are thus typified as centrosymmetric.^{97,98} To illustrate, a crystal possesses an inversion center at position (0,0,0), if any crystal constituent at position (x,y,z) is equivalently present at position (-x,-y,-z). Centrosymmetry excludes the crystal from exhibiting enantiomorphism (chirality), as well as pyro- and piezoelectricity. These effects involve serious impacts on the intrinsic charge carriers' spin polarization.

Figure 4.1 in Chapter 4 shows an HAADF-STEM (high-angle annular dark-field scanning transmission electron microscopy) image of the CsPbI₃ NCs produced and investigated in the

¹The space group symbol is composed of a capital letter representing the underlying lattice type (P=Primitive), followed by a set of characters indicating the space group's symmetry elements.⁹⁸

scope of this thesis. Precise analysis of HAADF-STEM images, alongside with patterns from X-ray crystallography reveal that CsPbI₃ NCs adopt orthorhombic crystal structure, i.e. the photoactive black perovskite γ -phase (Pbnm).^{72,95,99} It is retained from cryogenic temperatures up to ≈ 473 K, where the crystal phase transitions to the δ -phase (Pnma).⁹⁵ Once in the δ -phase, this phase is irreversibly retained, even upon cooling back to room temperature. Remarkably, this thermal behaviour is in stark contrast to that of bulk CsPbI₃. The latter adopts the orthorhombic δ -phase (Pnma) as its equilibrium phase at ambient and low temperatures. It, however, undergoes a phase transition to the cubic α -phase above ≈ 587 K and successively transitions to the tetragonal β -phase at ≈ 554 K and to the orthorhombic γ -perovskite phase (Pbnm) at ≈ 457 K upon cooling.¹⁰⁰ Subsequently, it is subject to rapid reversion to the equilibrium yellow non-perovskite δ -phase, which is further reinforced through the exposure to moisture.^{92–94} The exceptional stability of the black perovskite γ -phase in NCs, in contrast to bulk, is believed to result from their high surface-to-volume ratio, which causes enough tensile surface strain to stabilize the crystal structure.^{72,101} Furthermore, their hydrophobic capping ligands, stemming from the synthesis of these colloidal NCs, act as a protective layer against humidity, preventing the NCs from fast degradation to the δ -phase.⁹⁵

2.1.3 Electronic Band Structure

In a solid, atoms are closely packed together with interatomic distances so small that their outer orbitals overlap.¹⁰² As an example, the ionic radius of free Pb²⁺ is 119 pm, and that of free I[−] is 220 pm.¹⁰³ Both radii combined is their hypothetical interatomic distance in vacuum, i.e. 119 pm + 220 pm = 339 pm. Comparing this value to the experimentally obtained Pb-I distance in cubic CsPbI₃, 311 pm at 300 K,⁷² affirms the conjecture that Pb and I orbitals overlap and hybridize in the perovskite framework. This suggests the use of the tight-binding model to explain the broadening of discrete atomic energy levels, as present in free atoms, into energy bands as exhibited by solids. Consequently, the wavevector \vec{k} takes on continuous values in solids, rather than discrete values in free atoms. Simultaneously, the electron wave functions become delocalized over the separation of neighbouring atoms involved in the hybridization.^{102,104} The dispersion of the electronic energy states can be calculated across high symmetry points of the crystal, resulting in the so called band structure of the crystal. CsPbI₃ in its cubic representation exhibits a direct band gap located at the R point of the first Brillouin zone, i.e. at the corner of the cube in reciprocal space (c.f. Figure 2.1 b,c).^{20,34} At this point the gap between highest VB and lowest CB defines the band gap.¹⁰² The band gap energy, as well as the properties of the band gap confining bands are highly relevant, as they

determine the optical characteristics of a crystal, since optical transitions occur primarily at the band gap.

As opposed to the outer atomic orbitals, the inner atomic orbitals remain discrete, as they do not overlap with orbitals of neighbouring atoms.¹⁰⁴ Consequently, the energy bands are characterized by the outer atomic orbitals. In case of CsPbI₃ the outer orbitals of ⁸²Pb (electronic configuration [Xe]4f¹⁴5d¹⁰6s²6p²) and ⁵³I ([Kr]4d¹⁰5s²5p⁵) are the main actors regarding its electronic band structure,^{20,34,60} as already introduced in Subsection 2.1.1. Considering only the nearest neighbours, five overlap matrix elements (disregarding SOC for now) describe how the individual outer atomic orbitals of Pb and I overlap.⁵⁹

$$\begin{aligned}
V_{ss} &= \langle S_0 | \hat{H}_{int} | S_1 \rangle = \langle S_0 | \hat{H}_{int} | S_2 \rangle = \langle S_0 | \hat{H}_{int} | S_3 \rangle \\
V_{s_0 p_{1,2,3}} &= \langle S_0 | \hat{H}_{int} | X_1 \rangle = \langle S_0 | \hat{H}_{int} | Y_2 \rangle = \langle S_0 | \hat{H}_{int} | Z_3 \rangle \\
V_{p_0 s_{1,2,3}} &= \langle X_0 | \hat{H}_{int} | S_1 \rangle = \langle Y_0 | \hat{H}_{int} | S_2 \rangle = \langle Z_0 | \hat{H}_{int} | S_3 \rangle \\
V_{pp\sigma} &= \langle X_0 | \hat{H}_{int} | X_1 \rangle = \langle Y_0 | \hat{H}_{int} | Y_2 \rangle = \langle Z_0 | \hat{H}_{int} | Z_3 \rangle \\
V_{pp\pi} &= \langle X_0 | \hat{H}_{int} | X_2 \rangle = \langle X_0 | \hat{H}_{int} | X_3 \rangle = \langle Y_0 | \hat{H}_{int} | Y_1 \rangle = \langle Y_0 | \hat{H}_{int} | Y_3 \rangle = \langle Z_0 | \hat{H}_{int} | Z_1 \rangle = \langle Z_0 | \hat{H}_{int} | Z_2 \rangle.
\end{aligned}$$

\hat{H}_{int} is an interaction Hamiltonian accounting for the interaction of overlapping orbitals. The orbitals of nearest neighbour atoms involved in hybridization are visualized in Figure 2.2. $|S_i\rangle$, $|X_i\rangle$, $|Y_i\rangle$, and $|Z_i\rangle$ denote the individual atomic s- and p- states, respectively, referring to individual atomic orbitals. The subscripts, i, denote the positions, 1,2,3, of the three nearest neighbour I atoms with respect to the Pb atom at position (0,0,0).

As already outlined above, it can be derived that the VB is predominantly composed of the anti-bonding Pb 6s-orbitals stemming from the hybridizations of Pb 6s and I 5p atomic orbitals, which correspond to the overlap matrix elements $V_{s_0 p_{1,2,3}}$.^{20,34,59,60} The main contribution to the CB is found to originate from anti-bonding Pb 6p orbitals with only minor admixture from I 5s orbitals, which correspond to the overlap matrix elements $V_{p_0 s_{1,2,3}}$.

Immediately at the band gap, i.e. at $\vec{k} = 0$, energy bands of crystals are quite similar to discrete energy states of single atoms. Based on this similarity, the electronic wave functions can be classified analogously.¹⁰⁴ To be precise, the electronic wave functions of single atoms are classified as s, p, d, etc., corresponding to the orbital angular momenta $l = 0, 1, 2$, etc., respectively. Accordingly, as established above, the VB wave function of CsPbI₃ exhibits overall s-character ($l = 0$), represented by the orbital wave function $|S\rangle$.^{73,104} The CB wave function, on the other hand, exhibits overall p-character ($l = 1$) in CsPbI₃. The projection of the orbital angular momentum operator \hat{L} along a given direction, commonly z, hence \hat{L}_z ,

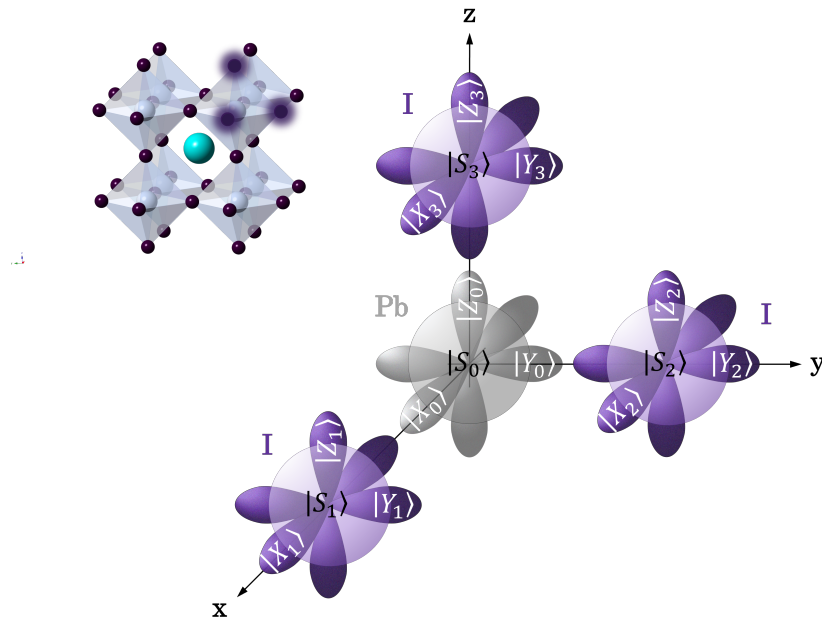


Figure 2.2: Visualization of the outermost s- and p-orbitals of neighbouring Pb and I atoms in CsPbI₃. The spherical s-orbital and the dumbbell-like p-orbitals along the x-, y- and z-axis are shown in gray for Pb and in purple for I atoms. Three exemplary atoms are accentuated in the illustrated perovskite crystal structure for geometrical guidance. The figure is reproduced and adapted from⁵⁹.

has eigenvalues $\hbar m_l$ (referred to as magnetic quantum numbers), i.e. $\hat{L}_z |l, m_l\rangle = \hbar m_l |l, m_l\rangle$.¹⁰⁵ With regard to the VB ($l = 0$) and the CB wave function ($l = 1$), the respective eigenvalues are $m_l = 0$ and $m_l = -1, 0, +1$.¹⁰⁴ It is customary to express the CB wave functions as $|X\rangle$, $|Y\rangle$, and $|Z\rangle$, all real. This practice originates from the analogy to atomic physics, where the angular function $Y_l^{m_l}(\theta, \varphi)$, known as spherical harmonics, relates the states $|l, m_l\rangle$ to their spatial orientations, x , y and z . Accordingly,

$$|l, m_l\rangle = \begin{cases} |1, +1\rangle & = -\frac{1}{\sqrt{2}} (|X\rangle + i|Y\rangle) \\ |1, 0\rangle & = |Z\rangle \\ |1, -1\rangle & = \frac{1}{\sqrt{2}} (|X\rangle - i|Y\rangle) \end{cases} \quad (2.8)$$

Hence, the energy bands are characterized by their orbital angular momentum (as long as the spin angular momentum is disregarded).

However, for a more accurate description of the energy bands SOC, a relativistic effect, must be taken into account.^{59,81} Referring again to atomic physics as a guideline, generally a carrier's spin angular momentum, S , and its orbital angular momentum, L , interact. This is because the magnetic field arising from the orbital motion of the charge carrier interacts with its intrinsic magnetic moment originating from its spin.^{104,105} The spin-orbit interaction

Hamiltonian $\hat{H}_{SO} = \frac{2}{3\hbar^2}\Delta_{SO}\hat{L}\hat{S}$ accounts for this.^{73,104,105} The inherent spin-orbit splitting Δ_{SO} in an atom approximately scales with $\propto Z^2$, where Z is the atomic number.^{38,104} In CsPbI₃ both, lead and iodine are heavy atoms, as can be seen from their large atomic numbers, $Z=82$ and $Z=53$, respectively. Therefore, these atoms have a large inherent spin-orbit splitting. Typically, the spin-orbit splitting of a semiconductor is comparable to that of its constituent atoms.¹⁰⁴ Consequently, Δ_{SO} is expected to be large in CsPbI₃. In fact, it is known to be substantial in LHPs in general and particularly strong in lead-iodine perovskites.¹⁰⁶ It amounts to $\Delta_{SO} \approx 1.3 \text{ eV}$ in CsPbI₃.^{34,59} As a comparison, SOC is considerably smaller in GaAs, $\Delta_{SO}^{GaAs} = 0.34 \text{ eV}$, and Si, $\Delta_{SO}^{Si} = 0.044 \text{ eV}$.¹⁰⁵

In order to include SOC in the expression of VB and CB states, the eigenstates of \hat{H}_{SO} , and therefore of $\hat{L}\hat{S}$, have to be found.¹⁰⁷ The eigenstates of the squared total angular momentum operator, $(\hat{J})^2 = (\hat{L} + \hat{S})^2 \Rightarrow \hat{J}^2 = \hat{L}^2 + \hat{S}^2 + 2\hat{L}\hat{S}$ includes the required term $\hat{L}\hat{S}$, and can be expressed as $\hat{L}\hat{S} = (\hat{J}^2 - \hat{L}^2 - \hat{S}^2)/2$. This means that the eigenstates of $\hat{L}\hat{S}$ are also eigenstates of $\hat{J}^2 - \hat{L}^2 - \hat{S}^2$. In fact, it can be shown that they are also eigenstates of \hat{J}^2 , \hat{L}^2 , and \hat{S}^2 , as all of these latter three operators commute. As \hat{J}^2 also commutes with \hat{J}_z , this qualifies to use the eigenstates of both, \hat{J}^2 and \hat{J}_z , to express the eigenstates of \hat{H}_{SO} and thus the VB and CB states. As a remark, this is only justified in semiconductors where SOC is significant (typically in small or moderate band gap semiconductors).³⁸ Otherwise, crystal-field interactions, i.e. electric fields from adjacent atoms/ ions, have to be considered in addition to SOC.

Analogous to above, the respective eigenvalues of \hat{S}_z , \hat{L}_z , \hat{J}_z are the magnetic quantum numbers $m_\alpha = -\alpha, -\alpha + 1, \dots, \alpha - 1, \alpha$, where $\alpha = s, l, j$, respectively. Because VB holes and CB electrons are fermions, $s = \frac{1}{2}$ and $m_s = -\frac{1}{2}, +\frac{1}{2}$. The VB and CB band gap states can now be expressed as

$$l_{VB} = 0, s = \frac{1}{2} \longrightarrow |j, m_j\rangle_{VB} = \left| \frac{1}{2}, -\frac{1}{2} \right\rangle, \left| \frac{1}{2}, +\frac{1}{2} \right\rangle \quad (2.9)$$

$$l_{CB} = 1, s = \frac{1}{2} \longrightarrow \begin{aligned} |j, m_j\rangle_{CB} &= \left| \frac{1}{2}, -\frac{1}{2} \right\rangle, \left| \frac{1}{2}, +\frac{1}{2} \right\rangle \\ |j, m_j\rangle_{CB'} &= \left| \frac{3}{2}, -\frac{3}{2} \right\rangle, \left| \frac{3}{2}, -\frac{1}{2} \right\rangle, \left| \frac{3}{2}, +\frac{1}{2} \right\rangle, \left| \frac{3}{2}, +\frac{3}{2} \right\rangle. \end{aligned} \quad (2.10)$$

From this it becomes clear that the three-fold degenerate CB (exclusively considering its orbital angular momentum, c.f. Equation 2.8) splits into a double degenerate ($j_{CB} = \frac{1}{2}$) and a quadruple degenerate ($j_{CB'} = \frac{3}{2}$) CB when SOC is taken into account.⁵⁹ $j_{CB'} = \frac{3}{2}$ lies energetically above $j_{CB} = \frac{1}{2}$, distanced by Δ_{SO} , as shown in Figure 2.3.^{34,59} The lower CB, $j_{CB} = \frac{1}{2}$, is commonly referred to as split-off band. Its minimum defines the upper limit of the band gap. Therefore, from here on, the focus will be put on CB, rather than CB', as CB is primarily relevant for the description of optical band gap transitions.

The VB and CB eigenstates in Equation 2.9 and Equation 2.10 can be expressed as linear combinations of the eigenstates of orbital ($|l, m_l\rangle$) and spin ($|s, m_s\rangle$) angular momenta.^{104,105} All factors can be calculated or found as Clebsch-Gordan coefficients in tables for angular momentum addition.^{108,109}

$$|j, m_j\rangle = \underbrace{\sum_{m_l} \sum_{m_s} \langle l, m_l, s, m_s | j, m_j \rangle}_{\text{Clebsch-Gordan coefficients}} |l, m_l, s, m_s\rangle$$

$$|j, m_j\rangle_{VB} = \begin{cases} \left| \frac{1}{2}, +\frac{1}{2} \right\rangle = \left| 0, 0, \frac{1}{2}, +\frac{1}{2} \right\rangle \\ \left| \frac{1}{2}, -\frac{1}{2} \right\rangle = \left| 0, 0, \frac{1}{2}, -\frac{1}{2} \right\rangle \end{cases}$$

$$|j, m_j\rangle_{CB} = \begin{cases} \left| \frac{1}{2}, +\frac{1}{2} \right\rangle = -\frac{1}{\sqrt{3}} \left| 1, 0, \frac{1}{2}, +\frac{1}{2} \right\rangle + \sqrt{\frac{2}{3}} \left| 1, +1, \frac{1}{2}, -\frac{1}{2} \right\rangle \\ \left| \frac{1}{2}, -\frac{1}{2} \right\rangle = \frac{1}{\sqrt{3}} \left| 1, 0, \frac{1}{2}, -\frac{1}{2} \right\rangle - \sqrt{\frac{2}{3}} \left| 1, -1, \frac{1}{2}, +\frac{1}{2} \right\rangle \end{cases} \quad (2.11)$$

To be precise, $|l, m_l, s, m_s\rangle$ signifies $|l, m_l\rangle \otimes |s, m_s\rangle$, because spin and orbital angular momentum states live in different Hilbert spaces. Inserting Equation 2.8 into Equation 2.11 and defining $|s, m_s\rangle = \left| \frac{1}{2}, +\frac{1}{2} \right\rangle := |\uparrow\rangle$ and $|s, m_s\rangle = \left| \frac{1}{2}, -\frac{1}{2} \right\rangle := |\downarrow\rangle$, the total angular momentum states corresponding to the VB and the split-off CB are^{73,104,105}

$$|j, m_j\rangle_{VB} = \begin{cases} \left| \frac{1}{2}, +\frac{1}{2} \right\rangle_{VB} = |S, \uparrow\rangle \\ \left| \frac{1}{2}, -\frac{1}{2} \right\rangle_{VB} = |S, \downarrow\rangle \end{cases} \quad (2.12)$$

$$|j, m_j\rangle_{CB} = \begin{cases} \left| \frac{1}{2}, +\frac{1}{2} \right\rangle_{CB} = -\frac{1}{\sqrt{3}} (|X + iY, \downarrow\rangle + |Z, \uparrow\rangle) \\ \left| \frac{1}{2}, -\frac{1}{2} \right\rangle_{CB} = -\frac{1}{\sqrt{3}} (|X - iY, \uparrow\rangle - |Z, \downarrow\rangle). \end{cases} \quad (2.13)$$

Note, that SOC is ineffective on S states, as the orbital angular momentum is zero ($l = 0$) and therefore no magnetic field is present which could couple to the spin.^{59,105} Hence, in the VB $j = s$, i.e. the spin polarization in $\left| \frac{1}{2}, +\frac{1}{2} \right\rangle_{VB} = |S, \uparrow\rangle$ is 100% up, while in $\left| \frac{1}{2}, -\frac{1}{2} \right\rangle_{VB} = |S, \downarrow\rangle$ it is 100% down. This is in stark contrast to the CB states, where SOC mixes the spin, i.e. $\frac{1}{3}$ up and $\frac{2}{3}$ down in $\left| \frac{1}{2}, +\frac{1}{2} \right\rangle_{CB}$ and $\frac{1}{3}$ down and $\frac{2}{3}$ up in $\left| \frac{1}{2}, -\frac{1}{2} \right\rangle_{CB}$, as given by the Clebsch-Gordan coefficients (c.f. factors in Equation 2.11 and Equation 2.13).

It is worth stressing that in LHPs both, the VB and the CB are two-fold degenerate, whereas in conventional II-VI and III-V compound semiconductors, the VB is four- and the CB two-fold degenerate.¹⁰⁵ In both materials, this is a consequence of SOC, which splits the two- and four-fold degenerate bands such that the former lies energetically below the latter. Hence,

because SOC influences the VB in II-VI and III-V compounds, the four-fold degenerate band is energetically located at the band gap. Analogously, because SOC influences the CB in LHPs, the two-fold degenerate band lies energetically at the band gap. The bands of both, conventional and perovskite semiconductors, are sketched in Figure 2.3a, allowing for a direct comparison between them.

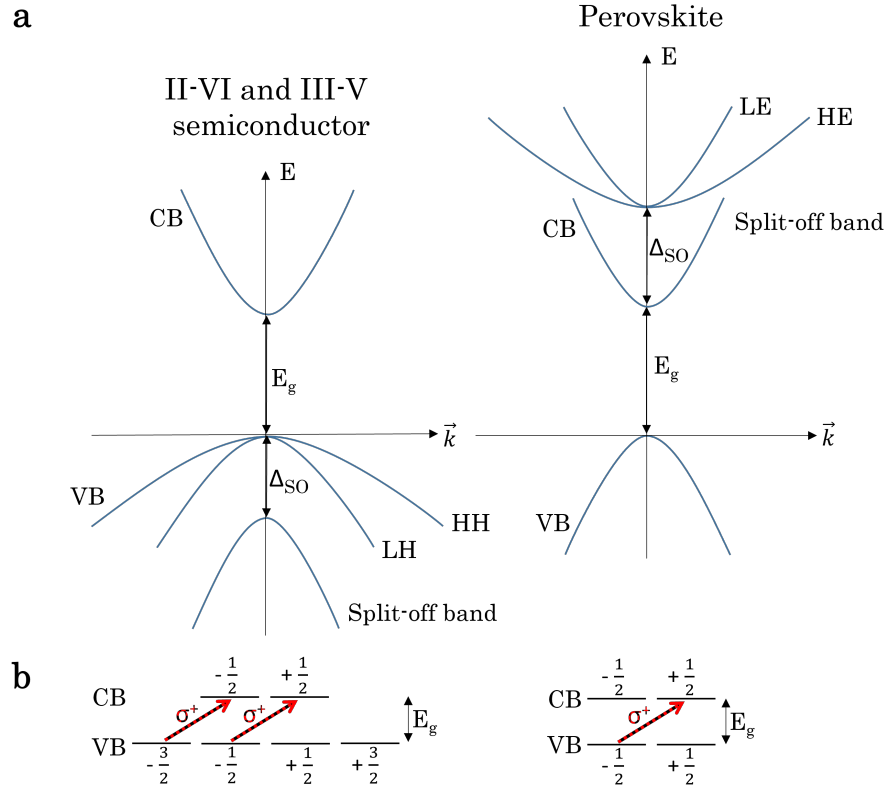


Figure 2.3: Comparison of the band structures and optical transitions in II-VI or III-V semiconductors and LHPs. (a) Band structures in the vicinity of the band gap of II-VI or III-V semiconductors (left) with the band gap at the Γ point¹⁰⁴ and LHPs (right) with the band gap at the R point in the 1st BZ. HH = heavy hole band, LH = light hole band, HE = heavy electron band, LE = light electron band. (b) Allowed optical transitions at the respective band gap induced by σ^+ polarized radiation with suitable wavelength. The fractions represent the magnetic quantum numbers (m_j). In II-VI and III-V compounds (left) two transitions are induced, which involve two VB and two CB states. On the contrary, in LHPs (right) solely one optical transition is induced, which involves only one VB and one CB state.

The four-fold degenerate VB in II-VI and III-V semiconductors, consisting of a so called light (LH) and heavy hole (HH) band, directly impact the optically allowed transitions. During absorption of circularly polarized photons two, rather than individual VB and CB states are addressed. This is sketched in Figure 2.3b. In LHPs on the other hand it is possible to address individual band gap states through circularly polarized photons. This manifests the tremendous advantage of executing spin studies in LHPs compared to in II-VI and III-V compound semiconductors. The reason for the different situations at the band gap lies in

the “inverted” band structure, i.e. a p-like VB and s-like CB in II-VI and III-V compound semiconductors, which is opposite to that in LHPs. Under consideration of SOC the VB is split into a quadruple and a double degenerate band, analogous to the CB in LHPs, as worked out above. However, $j_{VB}^{II-VI,III-V} = \frac{3}{2}$ lies energetically above $j_{VB}^{II-VI,III-V} = \frac{1}{2}$ and thus defines the lower limit of the band gap. Therefore, in II-VI and III-V compounds, four, rather than two degenerate VB states define the lower limit of the band gap.

2.2 Light-Matter Interaction

2.2.1 Optical Absorption

When light hits a semiconducting material, such as LHPs, it is subject to several optical effects.^{38,104} Figure 2.4 sketches this scenario, showing a collection of linear optical processes.

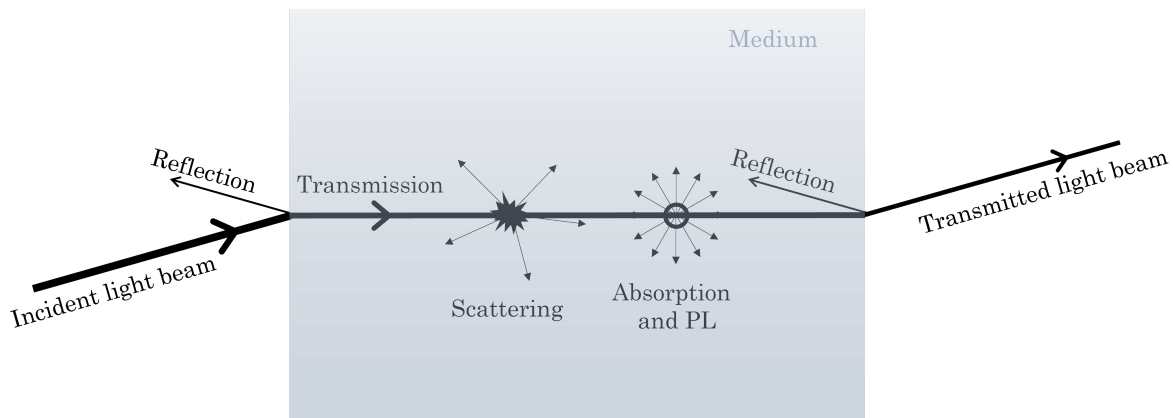


Figure 2.4: Surface and interior optical effects occurring upon light-matter interaction. Here, linear optical processes are considered exclusively.

Briefly mentioning those processes one by one, light-matter interaction begins at the surface of the material, where a fraction of the incident light is reflected. The rest is transmitted into the material, where it may be scattered, absorbed, or simply propagates to the back surface of the material, where it is again reflected or transmitted.^{38,104} Reflection, scattering and absorption are all processes which attenuate the light ray during propagation. Scattering may occur on static, as well as on dynamic inhomogeneities and causes photons to be re-directed in diffuse directions. Dynamic inhomogeneities may be for example density fluctuations associated with acoustic waves (Brillouin scattering) or optical phonons (Raman scattering). Photons with sufficient energy to overcome the band gap of a semiconducting material may be absorbed.

Subsequently, the excitation energy is dissipated as heat before possibly re-emitting non-directional radiation in form of spontaneous photoluminescence (PL). In general, reflection and absorption processes are strongest, as they involve the lowest order of light-matter interactions. For the sake of completeness, besides the mentioned processes, the electromagnetic (EM) wave is furthermore subject to refraction. Refraction becomes apparent as bending of the light ray at material interfaces. This is a consequence of the reduced travelling velocity of an EM wave inside a medium compared to its velocity in vacuum, c .

If the intensity of the light beam is high, several additional phenomena must be taken into account. Examples are sum and difference harmonics generation. Such non-linear optical processes involve higher-order optical interactions and are suppressed for low laser intensities and non-coherent light sources.

Based on the variety of introduced processes, optical spectroscopy represents a rich source of information on intrinsic semiconductor properties. From here on, the focus will be put on absorption spectroscopy, as this technique is well suited for detecting spin related phenomena in LHPs and was therefore used intensively in the scope of this thesis. Below, the basic principles of absorption spectroscopy, in particular those fundamental to calculations performed in this work, are established.

A plane EM wave propagating in z -direction, with wave vector k and angular frequency ω , can be described by its spatial and time dependent electric field

$$\tilde{\mathcal{E}}(z, t) = \mathcal{E}_0 e^{i(kz - \omega t)}. \quad (2.14)$$

Although this equation is complex, which is often more practical during calculation, it is important to remember to take the real part in the end, because a physical EM wave is real. In a medium, the dispersion relation of light is $\omega = \frac{c}{\tilde{n}(\omega)}k$, with the complex refractive index $\tilde{n}(\omega) = n_r(\omega) + i n_i(\omega)$, composed of real, $n_r(\omega)$, and imaginary, $n_i(\omega)$, refractive indices.³⁸ Using this to express k in Equation 2.14 gives

$$\begin{aligned} \tilde{\mathcal{E}}(z, t) &= \mathcal{E}_0 e^{i\left(\frac{\tilde{n}(\omega)}{c}\omega z - \omega t\right)} = \underbrace{\mathcal{E}_0 e^{-\frac{n_i(\omega)}{c}\omega z}}_{\equiv \mathcal{E}_{amp}(\omega)} e^{i\left(\frac{n_r(\omega)}{c}\omega z - \omega t\right)}. \end{aligned} \quad (2.15)$$

The rightmost exponential function reveals that the wave's phase inside the material is determined by $n_r(\omega)$. Consequently, its travelling velocity within the material is

$$v(\omega) = \frac{c}{n_r(\omega)}. \quad (2.16)$$

The exponential function second to last in Equation 2.15 has a real exponent and acts directly on the amplitude \mathcal{E}_0 . This causes the EM wave to decay exponentially with depth z inside a medium, if $n_i(\omega)$, also referred to as extinction coefficient, is non-zero. From this, the intensity of a light beam¹¹⁰

$$I(z) = \frac{cn_r\epsilon_0}{2} \mathcal{E}_{amp}^2(\omega) \quad (2.17)$$

can be deduced, which is experimentally easier accessible compared to its electric field.

Beer's law, given in Equation 2.18, relates the decay of light intensity to its entering depth z into a medium by assuming absorption to be the exclusive optical process responsible for the intensity decay.^{38,104} Therefore, an absorption coefficient, $\alpha(\omega)$, is introduced, which is a strong function of ω and a material specific coefficient.

$$I(z) = I_0 e^{-\alpha(\omega)z}, \quad (2.18)$$

with the incident light intensity at the material interface $I_0 = I(z = 0)$. In absorption spectroscopy, a material's transmission spectrum is recorded through a wavelength scan within the spectral area of interest. Assuming absorption to be responsible for the wavelength specific decrease in transmitted light intensity, Beer's law can be applied. Thus, $\alpha(\omega)$ is an experimentally accessible parameter through absorption spectroscopy.

The absorption process and hence $\alpha(\omega)$ is also accessible through theoretical derivations. Theoretical considerations of absorption are based on the underlying fundamental processes and are thus essential to profoundly understand an experimentally recorded absorption spectrum. To be precise, it is the imaginary part of the relative dielectric function, $\epsilon_i(\omega)$, which will be derived below, as its expression, once known, permits to fully calculate $\alpha(\omega)$. This becomes evident from the expression of $\alpha(\omega)$ in Equation 2.19, which is found as follows. On comparison of Equation 2.17 and Equation 2.18, and by using that the complex relative dielectric function, $\tilde{\epsilon}_{rel}(\omega) = \epsilon_r(\omega) + i\epsilon_i(\omega)$, is related to the complex refractive index via $\tilde{n}(\omega) = \sqrt{\tilde{\epsilon}_{rel}(\omega)}$,¹¹⁰ the absorption coefficient can be expressed in terms of the imaginary part of the relative dielectric function, $\epsilon_i(\omega) = 2n_r(\omega)n_i(\omega)$,^{38,104}

$$\alpha(\omega) = 2 \frac{n_i(\omega)}{c} \omega = \frac{\epsilon_i(\omega)}{n_r(\omega)c} \omega. \quad (2.19)$$

From this equation the absorption coefficient will be fully calculable, because $\varepsilon_i(\omega)$ will be derived from theoretical prospects below and

$$n_r(\omega) = \frac{1}{\sqrt{2}} \sqrt{\varepsilon_r(\omega) + \sqrt{\varepsilon_r(\omega)^2 + \varepsilon_i(\omega)^2}}. \quad (2.20)$$

Meanwhile, $\varepsilon_r(\omega)$ is accessible through the respective Kramers–Kronig relation

$$\varepsilon_r(\omega) - 1 = \frac{2}{\pi} \mathcal{P} \int_0^\infty \frac{\omega' \varepsilon_i(\omega')}{\omega'^2 - \omega^2} d\omega', \quad (2.21)$$

where \mathcal{P} stands for “principal part of the integral”, i.e. it insures that a singularity in the denominator ($\omega'^2 = \omega^2$) is avoided.

Thus, in order to calculate $\alpha(\omega)$, $\varepsilon_i(\omega)$ must be derived, which will be pursued from here on. A photon with sufficient energy to overcome the band gap of a semiconducting material may be absorbed by exciting an electron from an initial state i in the VB, to a final state f in the CB.³⁸ Since for a given photon energy, transitions between many CB states are possible, the rate for the absorption of one photon involves a summation over initial and final electron states. The rate of absorption per unit volume of a cell of the material will therefore be denoted as R . Absorption, thus, causes the EM field to lose energy (per unit volume of the incident beam) of the amount

$$-\frac{dE}{dt dV} = R \hbar \omega. \quad (2.22)$$

The above expression can be related to the intensity of the light beam, by multiplying the energy density with the travel velocity of the photons in the medium, i. e. $\frac{c}{n_r}$. This leads to

$$-\frac{dI}{dt} = \frac{c}{n_r(\omega)} R \hbar \omega. \quad (2.23)$$

With the aim to find a relationship between R , which can be calculated using Fermi’s Golden Rule, and $\varepsilon_i(\omega)$, the power loss rate $\frac{dI}{dt}$ is transformed as¹⁰⁴

$$\begin{aligned} -\frac{dI}{dt} &= -\frac{dI}{dz} \frac{dz}{dt} = -\frac{d}{dz} (I_0 e^{-\alpha(\omega)z}) \frac{c}{n_r(\omega)} = \alpha(\omega) I(z) \frac{c}{n_r(\omega)} = I(z) \frac{\omega \varepsilon_i(\omega)}{n_r(\omega)^2} \\ &= \frac{\varepsilon_0 \varepsilon_i(\omega) c \omega}{2 n_r(\omega)} \mathcal{E}_{amp}^2(\omega), \end{aligned} \quad (2.24)$$

where Equation 2.16 – Equation 2.19 were used. Finally, setting Equation 2.23 and Equation 2.24 equal gives

$$\varepsilon_i(\omega) = \frac{2\hbar}{\varepsilon_0 \mathcal{E}_{amp}^2(\omega)} R. \quad (2.25)$$

According to Fermi's Golden Rule¹⁰⁴

$$R = \frac{2\pi}{\hbar} \sum_{\vec{k}_c, \vec{k}_v} |\langle c | \hat{H}_{e^-, \text{Radiation}} | v \rangle|^2 \delta(E_c(\vec{k}_c) - E_v(\vec{k}_v) - \hbar\omega), \quad (2.26)$$

where the summation is to be understood per unit volume of the crystal. It is instructive to consider the individual components of this equation in more detail, which is done now.

As an electron moves inside a crystal, it moves in a periodic potential originating from the lattice constituents. Its wave functions are therefore expressed in form of Bloch functions, which include the lattice periodicity in the periodic functions $u_{c/v}(\vec{r})$.¹⁰⁴

$$\begin{aligned} |c\rangle &= u_{c, \vec{k}_c}(\vec{r}) e^{i\vec{k}_c \vec{r}} \quad \text{for an electron in the CB,} \\ |v\rangle &= u_{v, \vec{k}_v}(\vec{r}) e^{i\vec{k}_v \vec{r}} \quad \text{for an electron in the VB.} \end{aligned} \quad (2.27)$$

Those multiplied by $e^{-i\omega_c/vt}$ are plane waves with an amplitude modulated by $u_{c/v}(\vec{r})$, respectively. $\hat{H}_{e^-, \text{Radiation}}$ in Equation 2.26 represents the electron, radiation interaction Hamiltonian, which introduces a weak perturbation to the otherwise unperturbed electrons inside the crystal.

$$\hat{H}_{e^-, \text{Radiation}} = \frac{e}{m} \vec{A} \hat{p}, \quad (2.28)$$

where \hat{p} is the electron momentum operator and $\vec{A} = \frac{1}{2} |\vec{A}_0| \left(e^{i(\vec{k}\vec{r} - \omega t)} + e^{-i(\vec{k}\vec{r} - \omega t)} \right) \hat{e}$ is the vector potential of the EM field, with \hat{e} a unit vector parallel to \vec{A} .¹⁰⁴ Accordingly, the transition matrix element in Equation 2.26 can be calculated as

$$\begin{aligned} |\langle c | \hat{H}_{e^-, \text{Radiation}} | v \rangle|^2 &= \left(\frac{e}{m} \right)^2 \frac{|\vec{A}_0|^2}{4} \left| \langle c | e^{i\vec{k}\vec{r}} \hat{e} \hat{p} | v \rangle \right|^2 \\ &= \left(\frac{e}{m} \right)^2 \frac{\mathcal{E}_{amp}^2(\omega)}{4\omega^2} |P|^2, \end{aligned} \quad (2.29)$$

where the electric dipole approximation, i.e. $\mathcal{E}_{amp}(\omega) = |\vec{A}_0| \omega$, was used to obtain the second row of Equation 2.29. The momentum matrix element $\left| \langle c | e^{i\vec{k}\vec{r}} \hat{e} \hat{p} | v \rangle \right|^2$ is only weakly dependent on \vec{k} and can therefore be treated as a constant $|P|^2$. To be precise, this is true within *electric dipole approximation*:¹⁰⁴ *Wavevector conservation dictates that $\vec{k}_c - \vec{k}_v = \vec{k}$. However, for visible*

and IR light, the radiation wavevector \vec{k} is small in comparison to typical Brillouin zone sizes and \vec{k}_c/ν .^{105,111} Therefore, \vec{A} can be expanded in a Taylor series $\vec{A} \propto e^{i\vec{k}\vec{r}} = \sum_{n=0}^{\infty} \frac{(i\vec{k}\vec{r})^n}{n!} = 1 + i\vec{k}\vec{r} + \mathcal{O}(\vec{k}^2)$. Within electric dipole approximation, all \vec{k} -dependent terms are neglected. In other words $\vec{k} = 0$ and $\vec{k}_c = \vec{k}_v$.

The delta function in Equation 2.26 ensures that the energy is conserved in the absorption process. Summing over \vec{k}_c and \vec{k}_v , and assuming parabolic bands, i.e. $\hbar\omega = E_g + \frac{\hbar^2 k^2}{2} \left(\frac{1}{m_e^*} + \frac{1}{m_h^*} \right)$, the delta function can be converted into a joint density of doubly spin degenerate VB and CB states (JDOS).^{38,104,105}

$$\text{JDOS} = \begin{cases} \frac{\sqrt{2\mu^3}}{\pi^2 \hbar^3} \sqrt{\hbar\omega - E_g} & \text{for } \hbar\omega > E_g \\ 0 & \text{for } \hbar\omega < E_g \end{cases} \quad (2.30)$$

Inserting both, the equation found for JDOS (Equation 2.30) and for $|\langle c | H_{e^- \text{-Radiation}} | v \rangle|^2$ (Equation 2.29) into Equation 2.26 and subsequently into Equation 2.25, the expression for the imaginary part of the dielectric function is obtained and reads

$$\varepsilon_i(\omega) = \frac{1}{8\pi\epsilon_0} \frac{e^2 (2\mu)^{\frac{3}{2}}}{m^2 \hbar^3 \omega^2} |P|^2 \sqrt{\hbar\omega - E_g}. \quad (2.31)$$

This equation describes direct interband transitions of free charge carriers near E_g within electric dipole approximation.

In a similar way, the conversion of a photon into an exciton can be derived. In this case, $|0\rangle$ describes the initial ground state without an exciton and $|f\rangle$ the final state, where an exciton with energy $E_f \equiv E_n = E_g - \frac{R_{yx}}{n^2}$ and wavevector $\vec{K} = \vec{k}_e + \vec{k}_h = \vec{k}_e - \vec{k}_v$ has been created.¹⁰⁴ These wave functions only couple to each other, i.e. photon absorption only becomes possible, if the matrix element $|\langle f | \hat{H}_{X, \text{Radiation}} | 0 \rangle|^2$ is non-zero. Again, Fermi's Golden Rule can be formulated as

$$R_{0 \rightarrow f} = \frac{2\pi}{\hbar} \sum_f |\langle f | \hat{H}_{X, \text{Radiation}} | 0 \rangle|^2 \delta(E_f(\vec{K}) - \hbar\omega). \quad (2.32)$$

The exciton envelope wave function is $\Phi_{nlm_l}(\vec{R}, \vec{r}) = \Psi_{\vec{K}} \phi_{nlm_l}(\vec{r}) \propto e^{i\vec{K}\vec{R}} \phi_{nlm_l}(\vec{r})$, with the center-of-mass coordinate $\vec{R} = \frac{m_e^* \vec{r}_e + m_h^* \vec{r}_h}{m_e^* + m_h^*}$, the relative coordinate $\vec{r} = \vec{r}_e - \vec{r}_h$ and the Hydrogen wave functions $\phi_{nlm_l}(\vec{r}) = Y_{lm}(\theta, \varphi) R_{nl}(r)$.¹⁰⁴ Due to wavevector conservation, the photon wavevector equals the exciton wavevector, i.e. absorption occurs at the point, where photon and exciton dispersion curves intersect. As the photon dispersion curve is very steep, \vec{K} is

small and can be approximated to be zero. Consequently, $0 \approx \vec{K} = \vec{k}_e - \vec{k}_v \Rightarrow \vec{k}_e \approx \vec{k}_v$. Thus, from now on, \vec{k}_e and \vec{k}_v will be collectively denoted as \vec{k}_e . With this, the matrix element can be rewritten as¹⁰⁴

$$\left| \langle f | \hat{H}_{X, \text{Radiation}} | 0 \rangle \right|^2 \propto \left| \phi_{nlm_l}(0) \right|^2 \left| \langle \Psi_{\vec{k}_e}^c | \hat{H}_{e^-}, \text{Radiation} | \Psi_{\vec{k}_e}^v \rangle \right|^2. \quad (2.33)$$

$\left| \phi_{nlm_l}(0) \right|^2$ gives the probability for electron and hole to be located within the same primitive cell, because $\vec{r} = 0$ is equivalent to $\vec{r}_e = \vec{r}_h$. Thus, the probability of optically creating an exciton, given by the matrix element in Equation 2.33, is proportional to the wave function overlap of electron and hole. As a side note, $\left| \phi_{nlm_l}(0) \right|^2$ is non-zero only if the orbital angular momentum is zero, i.e. $l = 0$ and consequently $m_l = 0$, which reveals that optically excited excitons only exist with s symmetry. Solving the Hydrogen wave functions¹⁰⁷ for $\vec{r} = 0, l = 0, m_l = 0$, while referring to electron and hole of an exciton (a_X) instead of electron and proton in a Hydrogen atom (a_0), gives

$$\left| \phi_{n00}(0) \right|^2 = \left| Y_{00}(\theta, \varphi) R_{n0}(0) \right|^2 = \left| \frac{1}{2\sqrt{\pi}} \frac{2}{a_X^2 n^2} \right|^2 = \frac{1}{\left| \sqrt{\pi} a_X^2 n^2 \right|^2} = \frac{1}{\pi a_X^3 n^3}. \quad (2.34)$$

$\left| \langle \Psi_{\vec{k}_e}^c | \hat{H}_{e^-}, \text{Radiation} | \Psi_{\vec{k}_e}^v \rangle \right|^2$, rightmost term in Equation 2.33, is treated analogously to Equation 2.29 above.¹⁰⁴

Finally, the imaginary part of the dielectric function for the exciton bound states results in¹⁰⁴

$$\varepsilon_i(\omega) = \frac{1}{2} \frac{e^2}{\varepsilon_0 \omega^2 m^2 a_X^3} |P|^2 \sum_{n=1}^{\infty} \frac{1}{n^3} \delta\left(\hbar\omega - \left(E_g - \frac{Ry_X}{n^2}\right)\right) \quad \text{for } \hbar\omega < E_g, \quad (2.35)$$

where a factor of 1/2 was included, which takes care of the spin degeneracy. It is intriguing that the oscillator strength of bound exciton states decreases with n^3 , while their binding energy decreases with n^2 . As $n \rightarrow \infty$, the discrete exciton bound states merge into a quasi continuum, while the corresponding exciton energies approach the band gap energy, i.e. $E_n = E_g - \frac{Ry_X}{n^2} \rightarrow E_g$.

Absorption of photons with energies $\hbar\omega > E_g$ is expressed analogously to the above derived continuum absorption for free carriers (Equation 2.31), multiplied by a term referred to as Coulomb enhancement factor (CEF), which accounts for the exciton effect that enhances

photon absorption in the continuum. Correspondingly,

$$\varepsilon_i(\omega) = \frac{1}{8\pi\varepsilon_0} \underbrace{\frac{\xi}{1-e^{-\xi}}}_{\text{CEF}} \underbrace{\frac{e^2(2\mu)^{\frac{3}{2}}}{m^2\hbar^3\omega^2}|P|^2 \sqrt{\hbar\omega - E_g}}_{\text{free carrier transition}} \quad \text{for } \hbar\omega > E_g, \quad (2.36)$$

where $\xi = 2\pi \sqrt{\frac{Ry_X}{\hbar\omega - E_g}}$.^{104,112} Both, Equation 2.35 and Equation 2.36 approach the same finite, non-zero value as $\hbar\omega \rightarrow E_g$, i.e.

$$\lim_{\hbar\omega \rightarrow E_g} \varepsilon_i(\hbar\omega) = \frac{e^2\mu}{2\varepsilon_0 m^2 E_g^2 a_X} |P|^2. \quad (2.37)$$

This demonstrates a smooth transition of discrete exciton bound state absorption (Equation 2.35) into continuum absorption (Equation 2.36). Experimentally obtained absorption spectra of perovskites, as well as conventional semiconductors confirm this theoretically derived prediction.^{80,113–115}

2.2.2 Polarization of EM Waves and Photons

Classically, a light wave propagating in z-direction is characterized by its spatial- and time-dependent electric field vector, $\vec{\mathcal{E}}(z, t)$ (Equation 2.14), which points perpendicular to the direction of propagation. Although it is real, it is often more practical to use a complex notation, remembering to take the real part in the end. Expressed in cartesian coordinates it is^{38,107}

$$\vec{\mathcal{E}}(z, t) = \begin{pmatrix} \mathcal{E}_0^x e^{i(kz-\omega t)} \\ \mathcal{E}_0^y e^{i(kz-\omega t+\phi)} \\ 0 \end{pmatrix} = \begin{pmatrix} \mathcal{E}_0^x \\ \mathcal{E}_0^y e^{i\phi} \\ 0 \end{pmatrix} e^{i(kz-\omega t)} = \vec{\mathcal{E}}_0 e^{i(kz-\omega t)}. \quad (2.38)$$

The polarization of the EM wave manifests itself in the direction of motion of $\vec{\mathcal{E}}_0$ in an x-y-plane at a fixed, arbitrary z-coordinate. In the commonly used “detector view convention” $\vec{\mathcal{E}}_0$ is viewed from the point of the detector towards the light source. In case of circular polarization, counter-clockwise rotation of $\vec{\mathcal{E}}_0$ is thus left-handed and clockwise rotation right-handed. (This definition is opposite to the “source view convention”.)

Figure 3.2 b and c in Subsection 3.2.2 illustrate the temporal evolution of $\vec{\mathcal{E}}_0$ for linearly and circularly polarized light, respectively.

Table 2.1 summarizes different types of polarization including the corresponding relative amplitudes, \mathcal{E}_0^x and \mathcal{E}_0^y , as well as the relative phase, ϕ .³⁸

Table 2.1: Various types of polarization and corresponding relative amplitudes and phases.

Polarization	Relative Amplitudes	Relative Phase ϕ
Linear, π	$\mathcal{E}_0^x, \mathcal{E}_0^y$ arbitrary	$0, \pi$
Left-handed circular, σ^+	$\mathcal{E}_0^x = \mathcal{E}_0^y$	$+\frac{\pi}{2}$
Right-handed circular, σ^-	$\mathcal{E}_0^x = \mathcal{E}_0^y$	$-\frac{\pi}{2}$
Elliptical	$\mathcal{E}_0^x \neq \mathcal{E}_0^y$ $\mathcal{E}_0^x = \mathcal{E}_0^y$	$\pm\frac{\pi}{2}$ $\neq 0, \neq \pm\frac{\pi}{2}, \neq \pi$
Unpolarized	$\mathcal{E}_0^x, \mathcal{E}_0^y$ random	random

It becomes clear from Figure 3.2 b and Table 2.1 that the x- and y-components of a linearly polarized electric field vector oscillate in phase with respect to one another. In contrast, the oscillations of x- and y-components of circularly polarized light are not in phase: the x-component (y-component) lags behind the y-component (x-component) by $\phi = 90^\circ$, or, equivalently a quarter wavelength, for right- (left-) handed circularly polarized light.

Bridging the gap between the classical and quantum mechanical description of light, any beam of light can be considered as a superposition of many beams consisting of a single photon each.¹⁰⁷ This leads to interesting consequences. For example, if a certain fraction of energy of a classical light beam is transmitted through a polarization selective prism, quantum mechanically, that fraction is interpreted as the probability that one photon passes the prism. In order to acquire a deeper understanding of photon polarization, from here on, it is specified via its quantum mechanical description. To begin with, a single photons' "state vector of polarization" is defined as¹⁰⁷

$$|\Psi\rangle = \begin{pmatrix} \psi_x \\ \psi_y \end{pmatrix}. \quad (2.39)$$

In contrast to the classical electric field, which is three dimensional and real, the photon polarization state is a vector in complex, two-dimensional space.¹⁰⁷

Pairs of photon polarization states can be found, which form a complete orthonormal basis. Those are for example $|x\rangle$ and $|y\rangle$, as well as $|\sigma^+\rangle$ and $|\sigma^-\rangle$.

$$|x\rangle = \begin{pmatrix} 1 \\ 0 \end{pmatrix}, \quad |y\rangle = \begin{pmatrix} 0 \\ 1 \end{pmatrix}, \quad \text{and} \quad |\sigma^+\rangle = \frac{1}{\sqrt{2}} \begin{pmatrix} 1 \\ i \end{pmatrix}, \quad |\sigma^-\rangle = \frac{1}{\sqrt{2}} \begin{pmatrix} 1 \\ -i \end{pmatrix} \quad (2.40)$$

Note, that their components are equivalent to the classical x- and y- components of $\vec{\mathcal{E}}_0$ (c.f. Equation 2.38 and Table 2.1). An arbitrary photon polarization state $|\Psi\rangle$ can be written as a coherent superposition of the chosen basis, e.g.

$$|\Psi\rangle = |x\rangle\langle x|\Psi\rangle + |y\rangle\langle y|\Psi\rangle = |\sigma^+\rangle\langle\sigma^+|\Psi\rangle + |\sigma^-\rangle\langle\sigma^-|\Psi\rangle. \quad (2.41)$$

Generalizing the above, $|\Psi\rangle$ can be expressed in any basis, $|a\rangle, |b\rangle$.¹⁰⁷ To do so, all vector components expressed in the old basis (e.g. $|x\rangle, |y\rangle$) must be transformed to the new basis.

$$\begin{aligned} \langle a|\Psi\rangle &= \langle a|x\rangle\langle x|\Psi\rangle + \langle a|y\rangle\langle y|\Psi\rangle \\ \langle b|\Psi\rangle &= \langle b|x\rangle\langle x|\Psi\rangle + \langle b|y\rangle\langle y|\Psi\rangle \\ \Rightarrow |\Psi\rangle &= \begin{pmatrix} \langle a|\Psi\rangle \\ \langle b|\Psi\rangle \end{pmatrix} = \underbrace{\begin{bmatrix} \langle a|x\rangle & \langle a|y\rangle \\ \langle b|x\rangle & \langle b|y\rangle \end{bmatrix}}_{\text{transformation matrix } \mathcal{R}} \begin{pmatrix} \langle x|\Psi\rangle \\ \langle y|\Psi\rangle \end{pmatrix}. \end{aligned} \quad (2.42)$$

The derivation of the transformation matrix is most illustrative by regarding $|a\rangle$ and $|b\rangle$ as basis vectors, which are rotated by an angle θ with respect to the original $|x\rangle$ and $|y\rangle$ basis vectors. An equivalent interpretation is that $|\Psi\rangle$ is rotated in the opposite direction, i.e. by $-\theta$.¹⁰⁷ In any case, the transformation matrix describing the rotation is easily derived and reads

$$\mathcal{R}(\theta) = \begin{bmatrix} \cos\theta & \sin\theta \\ -\sin\theta & \cos\theta \end{bmatrix} = \underbrace{\cos\theta \begin{bmatrix} 1 & 0 \\ 0 & 1 \end{bmatrix}}_{\mathbb{1}} + i \sin\theta \underbrace{\begin{bmatrix} 0 & -i \\ i & 0 \end{bmatrix}}_{\hat{S}} \quad (2.43)$$

The knowledge of the eigenvalues and eigenstates of $\mathcal{R}(\theta)$ contains important information about intrinsic quantum mechanical properties of photon polarization. They are found by solving the Schrödinger equation $\mathcal{R}(\theta)|\Psi\rangle = r|\Psi\rangle$. As an intermediate step, $\hat{S}|\Psi\rangle = \lambda|\Psi\rangle$ has to be solved first. It is straight forward to find

$$\hat{S}|\sigma^+\rangle = +1|\sigma^+\rangle \quad \text{and} \quad \hat{S}|\sigma^-\rangle = -1|\sigma^-\rangle. \quad (2.44)$$

In fact, \hat{S} is the spin operator of the photon!¹⁰⁷ A photon in its spin eigenstate $|\sigma^+\rangle$ ($|\sigma^-\rangle$) has spin +1 (−1). Any other arbitrary polarization state of the photon is a superposition of a spin +1 and a spin −1 photon.

This is now written out for a general case and an explicit example of linear polarization in x-direction.

$$\begin{aligned}
 \text{Arbitrary polarization: } |\Psi\rangle &= \frac{1}{\sqrt{2}}(\psi_x - i\psi_y)|\sigma^+\rangle + \frac{1}{\sqrt{2}}(\psi_x + i\psi_y)|\sigma^-\rangle \\
 \text{x-polarization: } |x\rangle &= \begin{pmatrix} 1 \\ 0 \end{pmatrix} = \frac{1}{\sqrt{2}}\frac{1}{\sqrt{2}}\begin{pmatrix} 1 \\ i \end{pmatrix} + \frac{1}{\sqrt{2}}\frac{1}{\sqrt{2}}\begin{pmatrix} 1 \\ -i \end{pmatrix} = \frac{1}{\sqrt{2}}|\sigma^+\rangle + \frac{1}{\sqrt{2}}|\sigma^-\rangle.
 \end{aligned} \tag{2.45}$$

Notice, that linear polarization is a superposition of equal amounts of +1 and -1 photon spin.¹⁰⁷

\hat{S}_z is the projection of the photon spin operator \hat{S} onto the z-axis. Its eigenvalues $m_s = \pm\hbar$ have a direct physical meaning, namely the spin angular momentum in z-direction.¹⁰⁷

$$\hat{S}_z|\sigma^+\rangle = +\hbar|\sigma^+\rangle \text{ and } \hat{S}_z|\sigma^-\rangle = -\hbar|\sigma^-\rangle \tag{2.46}$$

Quantum mechanically, a particle's helicity describes the projection of its spin onto its momentum. Thus, if a photon is moving in z-direction and it is in a state $|\sigma^+\rangle$ ($|\sigma^-\rangle$), then its spin and momentum are parallel (anti-parallel) and its helicity is $+\hbar$ ($-\hbar$).

I will complete this subsection about photon polarization by returning once more to $\mathcal{R}(\theta)$. From Equation 2.43, Equation 2.44 and Equation 2.46 it is clear, that $|\sigma^+\rangle$ and $|\sigma^-\rangle$ are not only eigenstates of \hat{S} and \hat{S}_z , but also of $\mathcal{R}(\theta)$. In fact, $|\sigma^+\rangle$ and $|\sigma^-\rangle$ are the only eigenstates of $\mathcal{R}(\theta)$. They are found by solving the respective Schrödinger equation

$$\mathcal{R}(\theta)|\Psi\rangle = (\cos\theta\mathbb{1} + i\sin\theta\hat{S})|\Psi\rangle = r|\Psi\rangle \Rightarrow \begin{cases} \mathcal{R}(\theta)|\sigma^+\rangle = (\cos\theta + 1 \cdot i\sin\theta)|\sigma^+\rangle = e^{+i\theta}|\sigma^+\rangle \\ \mathcal{R}(\theta)|\sigma^-\rangle = (\cos\theta - 1 \cdot i\sin\theta)|\sigma^-\rangle = e^{-i\theta}|\sigma^-\rangle \end{cases}$$

The eigenvalues $e^{+i\theta}$ and $e^{-i\theta}$ of $\mathcal{R}(\theta)$ corresponding to its eigenvectors $|\sigma^+\rangle$ and $|\sigma^-\rangle$, respectively, indicate that the components of the eigenvectors merely change by a complex phase under rotation of the basis.

2.2.3 Selection Rules and Optical Orientation

In electric dipole approximation, optical transitions within atoms obey selection rules, which result from restrictions imposed on the matrix element by symmetry considerations.¹⁰⁴ Explicitly, a transition is dipole allowed if $\Delta l = \pm 1$.¹⁰⁵ Taking SOC into account and differentiating between linearly and circularly polarized irradiation, transitions obey $\Delta m_J = 0$ and $\Delta m_J = \pm 1$, respectively. Indeed, this can be also applied to optical transitions in crystals, which are governed by synonymous selection rules. Figure 2.5 shows the involved energetic levels at the CsPbI₃ band gap (at $\vec{k} = 0$), it is essentially a close up view of Figure 2.3 right. It visualizes the discussed optical transitions induced by absorption of linearly (π , purple) or circularly (σ^+ , red and σ^- , blue) polarized light. Each arrow implicates the creation of one VB hole at the foot, and one CB electron at the head of the respective arrow.

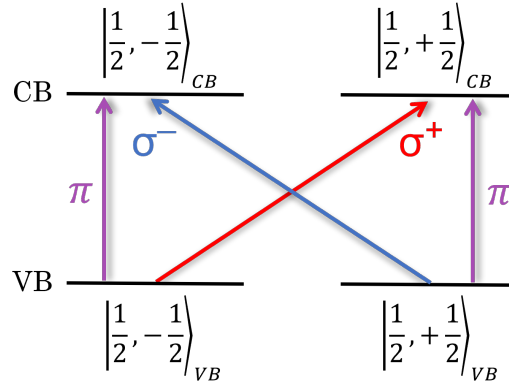


Figure 2.5: Optical transitions at the CsPbI₃ band gap. The arrows indicate interband transitions induced by linearly (π), as well as circularly polarized irradiation (σ^+ , σ^-).

In the following, the matrix elements for interband transitions in CsPbI₃ from $|\frac{1}{2}, \pm\frac{1}{2}\rangle_{VB}$ (c.f. Equation 2.12) to $|\frac{1}{2}, \pm\frac{1}{2}\rangle_{CB}$ (c.f. Equation 2.13) are calculated. Hereby, the interconnection between selection rules and light polarization is nicely perceivable.

The transition probability for an interband transition from initial state $|v\rangle$ to $|c\rangle$ is proportional to the transition matrix element $\langle c | \hat{H}_{e^-, \text{Radiation}} | v \rangle$ (Equation 2.26). According to Equation 2.29 $\langle c | \hat{H}_{e^-, \text{Radiation}} | v \rangle \propto \langle c | \vec{A} \hat{p} | v \rangle$, where \vec{A} describes the incoming EM field and \hat{p} is the momentum operator of an electron inside a crystal. With $\vec{A} \propto \vec{\mathcal{E}}_0$, the transition matrix element for an optical transition from $|\frac{1}{2}, -\frac{1}{2}\rangle_{VB}$ to $|\frac{1}{2}, +\frac{1}{2}\rangle_{CB}$ (red arrow labeled σ^+ in Figure 2.5) is proportional to

$$\begin{aligned}
{}_{CB}\langle \frac{1}{2}, +\frac{1}{2} | \vec{\mathcal{E}}_0 \hat{p} | \frac{1}{2}, -\frac{1}{2} \rangle_{VB} &= \vec{\mathcal{E}}_0 {}_{CB}\langle \frac{1}{2}, +\frac{1}{2} | \begin{pmatrix} \hat{p}_x \\ \hat{p}_y \\ \hat{p}_z \end{pmatrix} | \frac{1}{2}, -\frac{1}{2} \rangle_{VB} \\
&\propto \vec{\mathcal{E}}_0 [\langle X - iY, \downarrow | + \langle Z, \uparrow |] \begin{pmatrix} \hat{p}_x \\ \hat{p}_y \\ \hat{p}_z \end{pmatrix} |S, \downarrow \rangle = \vec{\mathcal{E}}_0 [\langle X - iY | \begin{pmatrix} \hat{p}_x \\ \hat{p}_y \end{pmatrix} |S \rangle \langle \downarrow | \downarrow \rangle + \langle Z | \begin{pmatrix} \hat{p}_x \\ \hat{p}_y \end{pmatrix} |S \rangle \langle \uparrow | \downarrow \rangle] .
\end{aligned} \tag{2.47}$$

By using the matrix-element theorem and that $\langle \downarrow | \downarrow \rangle = 1$ and $\langle \uparrow | \downarrow \rangle = 0$, the last term can be recognized to be zero. The matrix-element theorem is based on group theoretical considerations and assigns irreducible representations to the energy bands of a semiconductor crystal.¹⁰⁴ It excludes for example transitions between bands of the same symmetry, i.e. both exhibit s symmetry, or both containing p symmetry, because of parity violation. (Bands of the same symmetry have the same parity, while \hat{p} has odd parity, thus reverting the parity of one band when building a direct product with it). The matrix-element theorem, hence, enables one to find the non-zero matrix elements responsible for interband transitions.^{104,105} Those are comparable for LHPs⁵⁹ and III-V compounds,^{104,105,116} because VB and CB are merely reversely ordered.

$$\langle c | \hat{p} | v \rangle = \langle X | \hat{p}_x | S \rangle = \langle Y | \hat{p}_y | S \rangle = \langle Z | \hat{p}_z | S \rangle = iP, \tag{2.48}$$

where P is a real constant, which has already been introduced in Subsection 2.2.1. Thus, Equation 2.47 reduces to

$${}_{CB}\langle \frac{1}{2}, +\frac{1}{2} | \vec{\mathcal{E}}_0 \hat{p} | \frac{1}{2}, -\frac{1}{2} \rangle_{VB} \propto \vec{\mathcal{E}}_0 \begin{pmatrix} \langle X | \hat{p}_x | S \rangle \\ -i \langle Y | \hat{p}_y | S \rangle \\ 0 \end{pmatrix} = \vec{\mathcal{E}}_0 P \begin{pmatrix} i \\ 1 \\ 0 \end{pmatrix} \tag{2.49}$$

At this point it is enlightening to ask which light polarization causes this matrix element and therefore the transition probability to maximize or to vanish. For this purpose, $\vec{\mathcal{E}}_0$, having arbitrary polarization for now, is expressed in components of left- and right-handed circular polarization according to Equation 2.45 top

$$\vec{\mathcal{E}}_0 \propto \alpha \vec{\mathcal{E}}_{\sigma^+} + \beta \vec{\mathcal{E}}_{\sigma^-} \propto \alpha \begin{pmatrix} 1 \\ i \\ 0 \end{pmatrix} + \beta \begin{pmatrix} 1 \\ -i \\ 0 \end{pmatrix}. \quad (2.50)$$

Inserting this into Equation 2.49 gives

$${}_{CB} \langle \frac{1}{2}, +\frac{1}{2} | \vec{\mathcal{E}}_0 \hat{p} | \frac{1}{2}, -\frac{1}{2} \rangle_{VB} \propto P[\alpha \underbrace{(i+i)}_{2i} + \beta \underbrace{(i-i)}_0] \propto \alpha. \quad (2.51)$$

Equation 2.51 demonstrates that exclusively the left-handed (σ^+) circular polarization components in the EM radiation induce the considered transition from $|\frac{1}{2}, -\frac{1}{2}\rangle_{VB}$ to $|\frac{1}{2}, +\frac{1}{2}\rangle_{CB}$ (red arrow labeled σ^+ in Figure 2.5).

Analogously it can be shown that an optical transition from $|\frac{1}{2}, +\frac{1}{2}\rangle_{VB}$ to $|\frac{1}{2}, -\frac{1}{2}\rangle_{CB}$ is exclusively induced by components corresponding to right-handed circular polarization in the EM radiation (blue arrow labeled σ^- in Figure 2.5). Meanwhile, transitions from $|\frac{1}{2}, +\frac{1}{2}\rangle_{VB}$ to $|\frac{1}{2}, +\frac{1}{2}\rangle_{CB}$ and $|\frac{1}{2}, -\frac{1}{2}\rangle_{VB}$ to $|\frac{1}{2}, -\frac{1}{2}\rangle_{CB}$ (purple arrows labeled π in Figure 2.5) are induced by linearly polarized EM radiation, i.e. equivalent amounts of left- and right-circular polarization ($\alpha = \beta$) as derived above for linearly x-polarized photons (Equation 2.45 bottom).

The described phenomenon, that individual states are addressable with circular polarization, is utilized as an experimental technique called optical orientation. Optical orientation, or optical spin injection describes the creation of a net spin polarization in a semiconductor via absorption of circularly polarized light.³⁸ In other words, a temporary non-equilibrium population of spin polarized charge carriers is induced, which subsequently decays via spin depolarizing processes, such as one or a combination of the EY, DP and BAP spin relaxation mechanisms, which will be covered below, in Section 2.4. For now, let us consider the effect of optical orientation at the instant in time of its occurrence. As established in Subsection 2.1.3, in LHPs, both, the VB and CB are two-fold spin degenerate. Optical orientation through resonant absorption of σ^+ (σ^-) polarized radiation generates electron-hole pairs with spin orientations $+\frac{1}{2}h, +\frac{1}{2}e$ ($-\frac{1}{2}h, -\frac{1}{2}e$), where the m_j spin orientation is expressed in hole (h) and electron (e) representation.³⁸ Note, that the unoccupied VB state has the opposite sign as the hole spin polarization, i.e. it is $|m_j = -\frac{1}{2}\rangle_{VB}$ ($|m_j = +\frac{1}{2}\rangle_{VB}$).

Because of this two-fold spin degeneracy of both, VB and CB, in LHPs, the theoretically maximal achievable electron and hole spin polarization, Π_e and Π_h is 100%. This is a consequence of SOC, which introduces the splitting of the two-fold ($j = \frac{1}{2}$) and four-fold ($j = \frac{3}{2}$) spin

degenerate CBs, shifting the latter away from the band gap (c.f. Subsection 2.1.3). Hence, strong SOC creates perfect conditions for optimal optical orientation,¹¹⁷ which is a property particularly valuable for quantum information science and spintronics.

In contrast, $\Pi_e = \Pi_h = 50\%$ in conventional II-VI and III-V semiconductors.^{37,38} The reason for the spin polarization being halved compared to that in LHPs lies in the four-fold spin degenerate VB in II-VI and III-V compounds, as shown in Figure 2.3 left. In order to explicitly calculate Π_e , to see that it amounts to 50%, the electron spin polarization is defined^{37,38}

$$\Pi_e = \frac{n_\uparrow - n_\downarrow}{n_\uparrow + n_\downarrow}. \quad (2.52)$$

n is the relative number of spin up (\uparrow) and spin down (\downarrow) electrons, induced by circularly polarized irradiation of desired handedness. The heavy-hole transitions are three times more likely than those from light-hole states.^{37,38} This results from the evaluation of the respective matrix elements, as qualitatively shown above for transitions in LHPs. Thus, for e.g. left-handed circularly polarized irradiation

$$\Pi_e^{\sigma^+} = \frac{3 - 1}{3 + 1} = 50\%. \quad (2.53)$$

The calculation of Π_h is analogous and results in 50% as well. The same is of course true for right-handed circularly polarized irradiation.

The fact that the LHP band structure offers perfect conditions for optimal optical orientation reaching up to a theoretical spin polarization of 100% makes LHPs appealing model systems for semiconductor spintronics³⁶ and fundamental spin studies.^{39,40}

2.3 Carrier-Phonon Coupling

The mechanical softness and ionicity of the LHP crystal lattice substantially impacts key electronic properties such as the exciton binding energy, charge carrier mobility and recombination, as well as charge carrier spin dynamics.^{89,106,113,117} To be precise, one, the charge carriers are embedded and influenced by the lattice-induced dielectric environment and two, they interact with the lattice in a direct way through carrier - phonon coupling.⁸⁹ Both will be discussed in this section. I will start with elaborating the origin of a material's dielectric permittivity.

The dynamical response of a material to an electric field with frequency ν is assessed by its relative permittivity (real part), $\epsilon_r(\nu)$, also referred to as dielectric permittivity. Importantly, it is a function of frequency, which is particularly pronounced in perovskites.⁸⁹ Sketching its shape from high to low frequency, the dielectric function $\epsilon_r(\nu)$ increases with every intrinsic resonance, because processes with high resonance frequencies can dynamically follow lower frequencies and thus contribute to $\epsilon_r(\nu)$, but not vice versa. At the high-frequency end, the dielectric function of perovskites is dictated by electronic interband transitions, $\nu \sim 10^{14} \text{Hz}$, and amplified by the contribution of polar lattice vibrations (LO phonons), $\nu \sim 10^{12} \text{Hz}$, predominantly originating from Pb–X stretching and Pb–X–Pb rocking modes within the $(\text{PbX}_6)^{4-}$ octahedra.^{89,118} Collective re-orientations of organic A cations commence at $\nu \sim 10^{11} \text{Hz}$, but are absent for inorganic LHPs, which have an atom (Cs) at the A site.⁸⁹ The final increment in $\epsilon_r(\nu)$ is associated with slow ion migration through the lattice, $\nu \lesssim 10^2 \text{Hz}$, in particular of I^- ions. In the low-frequency vicinity of every resonance, $\epsilon_r(\nu)$ transitions into a plateau, i.e. a quasi-static dielectric permittivity, $\epsilon_{r,static}(\nu)$, turning the dielectric function ($\epsilon_r(\nu)$ plotted against ν) roughly into a step-like function.

In semiconductors, $\epsilon_r(\nu)$ is especially relevant at the frequency corresponding to the electron-hole motion in excitons, denoted by $\epsilon_{r,eff}$, as it determines the strength of screening of the Coulomb interaction between electron and hole. This is manifested in the exciton binding energy according to Equation 2.4, i.e. $B_X \propto \frac{1}{\epsilon_{r,eff}^2}$. Polarization responses of processes with resonance energies of the order of B_X and above contribute to dielectric screening, whereas those significantly below B_X do not contribute, because they are too inert to follow the electron-hole motion effectively. Thus, in LHPs, the leading contribution to exciton screening stems from processes at the above sketched high-frequency end of the dielectric function: explicitly, these processes are electronic interband transitions and LO phonons.^{89,118} On this basis, the mean value of several theoretical and experimental examinations converges to $\epsilon_{r,eff} \approx 8$ for orthorhombic CsPbI_3 .^{75,78,89,91} The high and low frequency plateaus surrounding $\epsilon_{r,eff}$ are dictated by the resonances of electronic interband transitions, $\epsilon_{r,static,optical} = 5.4$, and LO phonons, $\epsilon_{r,static,LOphonons} = 30.4$, respectively.⁸⁹ It is noteworthy, that the latter two values were determined for MAPbI_3 . However, it is justified to adopt them for CsPbI_3 , as the resonance frequency of the organic MA molecule is one order of magnitude smaller than that of LO lattice vibrations and thus only commences to contribute to dielectric screening for frequencies significantly below $\epsilon_{r,static,LOphonons}$.^{75,89}

Let us now draw the attention to direct carrier-lattice interaction, i.e. scattering. Generally, scattering in a crystal only occurs due to a deficiency of real space periodicity.¹¹¹ The reason

behind this is that the wave function of a charge carrier in a perfectly periodic crystal, i.e. without any perturbations, persists forever. Distortions of the lattice periodicity may be caused by crystal boundaries, impurities, defects, other carriers, phonons, etc. and this way limit the lifetime of the carrier's wave function. In other words, scattering occurs as a consequence of crystal lattice imperfections.

Particularly relevant to LHPs is carrier-phonon scattering. Hence, it is instructive to firstly specify what a phonon is. Lattice vibrations, i.e. collective atomic modes, are customarily quantised in form of massless, bosonic quasiparticles called phonons, which, depending on their type, couple to charge carriers through different mechanisms.¹¹¹ Symmetry analysis reveals that in LHPs, carriers predominantly couple to polar LO phonons through Fröhlich interaction and to non-polar acoustic phonons through deformation potential scattering (ADP).¹¹⁹ In LHPs, and ionic crystals in general, LO phonons are accompanied by a macroscopic electric field, which arises from the relative displacements of metal cations (Pb^{2+}) against halide anions (X^-).⁸⁹ Through Coulomb interaction, charge carriers interact strongly with this field, making Fröhlich interaction the dominant carrier-phonon scattering mechanism, while causing contributions from other mechanisms to be practically irrelevant at room temperature as expected for ionic materials.^{104,119,120} Charge carrier - acoustic phonon coupling through deformation potential scattering, on the other hand, has a different underlying mechanism: acoustic phonon modes involve temporary lattice perturbations, that cause modulations of the band structure, i.e. of the “landscape” of charge carriers, and this way interact with them.⁸⁹ Acoustic phonon scattering only becomes important at cryogenic temperatures, where optical phonons become scarce, because generally, when both, acoustic and optical phonons modes are thermally excited, the optical phonon scattering rate is considerably higher than that of acoustic phonons.^{82,112,120} Quantitatively, in CsPbI_3 NCs, the phonon energies were experimentally determined to be $E_{LO} \approx 26.3 \pm 7.0 \text{ meV}$ and $E_{ADP} \approx 7.2 \text{ meV}$.⁸²

Carrier-phonon interactions mediate the exchange of energy and momentum between charge carriers and the lattice.¹¹² It has therefore major impact on the cooling behaviour of photoexcited charge carriers. In the so called phonon-cascade model, hot² charge carriers cool down towards the band edge via a cascade of emission of LO phonons until their energy falls below the threshold energy for LO phonon emission ($E < E_{\text{phonon}}$). Cooling via the phonon-cascade model is the dominant way hot charge carriers cool down in LHPs and conventional semi-

²Within the first ps after photoexcitation, the non-thermal carrier distribution thermalizes via carrier-carrier scattering to a Maxwell-Boltzmann distribution.^{33,112} The latter allows for the assignment of a carrier temperature T_C . Charge carriers, which are photoexcited into the VB/CB with excess energy have a carrier temperature, which is larger than the lattice temperature T_L . This justifies to refer to them as “hot” carriers. During the cooling process, T_C converges towards T_L .

conductors, as long as the density of photoexcited carriers is small,^{33,112} which is the case for all experiments conducted in the scope of this thesis. Otherwise, reabsorption of emitted LO phonons by carriers, as well as carrier-carrier interactions like Auger recombination are present, which perturb the cascade process.

Momentum and energy conservation impose limitations on the wavevectors of LO phonons, which are absorbable and emittable by charge carriers. That is, $\vec{k}' = \vec{k} \pm \vec{q}$ and $E' = E \pm E_{phonon}$, respectively.¹⁰⁵ The LO phonon wavevector, denoted by \vec{q} , has an interjacent angle θ with the initial wavevector of the carrier, \vec{k} . After the carrier-LO phonon scattering event, the final carrier wavevector \vec{k}' encloses an angle θ_k with \vec{k} . Table 2.2 summarizes the restrictions momentum and energy conservation impose on the magnitude of the carrier's wavevector and energy in a carrier - LO phonon scattering event.

Table 2.2: Momentum and energy conservation in a carrier - LO phonon scattering event.¹⁰⁵

	Phonon Absorption	Phonon Emission
Momentum Conserv.	$k'^2 = k^2 + q^2 + 2kq \cos\theta$	$k'^2 = k^2 + q^2 - 2kq \cos\theta$
Energy Conserv.	$\frac{\hbar^2 k'^2}{2m^*} = \frac{\hbar^2 k^2}{2m^*} + \hbar\omega_{LO}$	$\frac{\hbar^2 k'^2}{2m^*} = \frac{\hbar^2 k^2}{2m^*} - \hbar\omega_{LO}$
Mom. & E. Conserv.	$\cos\theta = \frac{m^*\omega_{LO}}{\hbar k q} - \frac{q}{2k} \equiv f(q)$	$\cos\theta = \frac{m^*\omega_{LO}}{\hbar k q} + \frac{q}{2k} \equiv f(q)$
$q_{min} =$	$k \left(\sqrt{1 + \frac{\hbar\omega_{LO}}{E}} - 1 \right), \theta_k = \theta = 0$	$k \left(1 - \sqrt{1 - \frac{\hbar\omega_{LO}}{E}} \right), \theta_k = \theta = 0$
$q_{max} =$	$k \left(\sqrt{1 + \frac{\hbar\omega_{LO}}{E}} + 1 \right), \theta_k = \theta = \pi$	$k \left(1 + \sqrt{1 - \frac{\hbar\omega_{LO}}{E}} \right), \theta_k = \pi, \theta = 0$

Inserting the respective expression of k' (1st row in Table 2.2) into the equation resulting from energy conservation (2nd row in Table 2.2) leads to a function $f(q)$ (3rd row in Table 2.2). As the cosine is defined between -1 and 1 , the equivalent must be true for $f(q)$, i.e. $-1 \leq f(q) \leq 1$. Solving this equation for q gives all absorbable or emittable phonon wavevectors q , where $q_{min} \leq q \leq q_{max}$ (4th row in Table 2.2). As an example, the process of phonon emission within a parabolic CB is illustrated in Figure 2.6.

The theoretical description of carrier-LO phonon scattering via Fröhlich interaction ($\hat{H}_{Fröhlich}$) can give further insight into this process. The corresponding matrix element is^{105,121,122}

$$M_{\vec{k} \rightarrow \vec{k} \pm \vec{q}} = \frac{|\langle \vec{k} \pm \vec{q} | \hat{H}_{Fröhlich} | \vec{k} \rangle|^2}{(n_{LO} + 1/2 \mp 1/2)} = \frac{e\hbar^2 \mathcal{E}_{LO}}{2Vq^2 m_e^*} \delta_{\vec{k}, \vec{k} \pm \vec{q}} = \frac{e^2 \hbar \omega_{LO}}{2Vq^2} \left(\frac{1}{\epsilon_\infty} - \frac{1}{\epsilon_0} \right) \delta_{\vec{k}, \vec{k} \pm \vec{q}}, \quad (2.54)$$

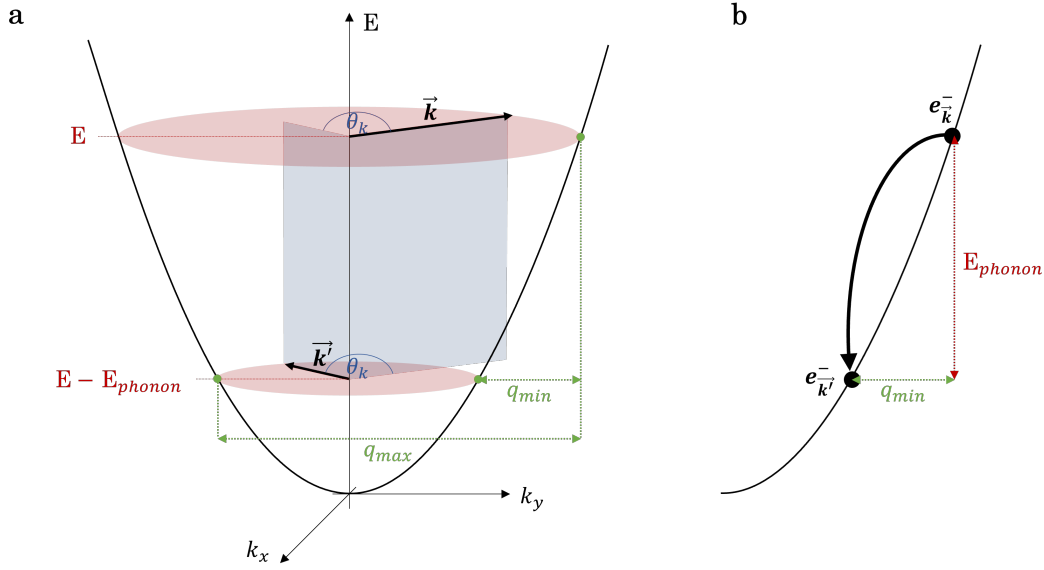


Figure 2.6: The process of carrier cooling according to the phonon-cascade model represented by one phonon emission event in a parabolic CB.^{105,112} (a) Shown are energies (red), maximum and minimum wave vectors (green) and the angle θ_k (blue) enclosed by initial (\vec{k}) and final (\vec{k}') wave vectors (black). The effective phonon-cascade process is governed by the emission of LO phonons with the smaller wavevector, q_{min} , justifying to sketch the phonon cascade process as shown in (b). The CB electron emitting an LO phonon yields $\vec{k} \parallel \vec{k}'$, i.e. $\theta_k = 0$.

where V is the crystal volume. The longitudinal electric field associated with the LO phonon is given by $\mathcal{E}_{LO} = \frac{m_e^* e \omega_{LO}}{\hbar} \left(\frac{1}{\epsilon_\infty} - \frac{1}{\epsilon_0} \right)$, with ϵ_∞ and ϵ_0 the high- and low-frequency dielectric permittivities of the material. In lead-iodide perovskites, the latter two variables can be assigned to $\epsilon_{r,static,optical}$ and $\epsilon_{r,static,LOphonons}$, respectively, as resonance corresponding to the electron-hole motion of an exciton lies in between these plateau values, as established above.⁸⁹ $M_{\vec{k} \rightarrow \vec{k} \pm \vec{q}} \propto \frac{1}{q^2}$ expresses the probability for the carrier-LO phonon scattering process, which maximizes for $q = q_{min}$. Therefore, in the cascade process preferentially phonons with the wavevector q_{min} are produced, resulting in a phonon distribution, which is strongly peaked near q_{min} .^{104,105,112} This justifies to sketch carrier cooling via the cascade process as shown in Figure 2.6 b.

The characteristic rate for carrier-LO phonon scattering via Fröhlich interaction is derived by using Fermi's golden rule and integrating over all final carrier states S_f , i.e. those with \vec{k}' .¹⁰⁵

$$\begin{aligned}
 W(\vec{k}) &= \frac{2\pi}{\hbar} \int |\langle f | \hat{H}_{Fröhlich} | i \rangle|^2 \delta(E_f - E_i) dS_f \\
 W(\vec{k}) &= \frac{2\pi}{\hbar} \int \frac{V}{(2\pi)^3} \left[M_{\vec{k} \rightarrow \vec{k} + \vec{q}} n_{LO} \delta(E_{\vec{k}} - E_{\vec{k} + \vec{q}} + \hbar\omega_{LO}) \right. \\
 &\quad \left. + \Theta(E - \hbar\omega_{LO}) M_{\vec{k} \rightarrow \vec{k} - \vec{q}} (n_{LO} + 1) \delta(E_{\vec{k}} - E_{\vec{k} - \vec{q}} - \hbar\omega_{LO}) \right] d\vec{k}' \quad (2.55)
 \end{aligned}$$

The LO phonon occupation number, n_{LO} , gives the number of thermally excited LO phonon modes with angular frequency ω_{LO} at temperature T .³⁸ This function is highly temperature dependent and dictated by Bose-Einstein statistics, as given by Equation 2.56 and plotted in Figure 2.7.

$$n_{LO} \propto \frac{1}{\exp\left(\frac{\hbar\omega_{LO}}{k_B T}\right) - 1} \quad (2.56)$$

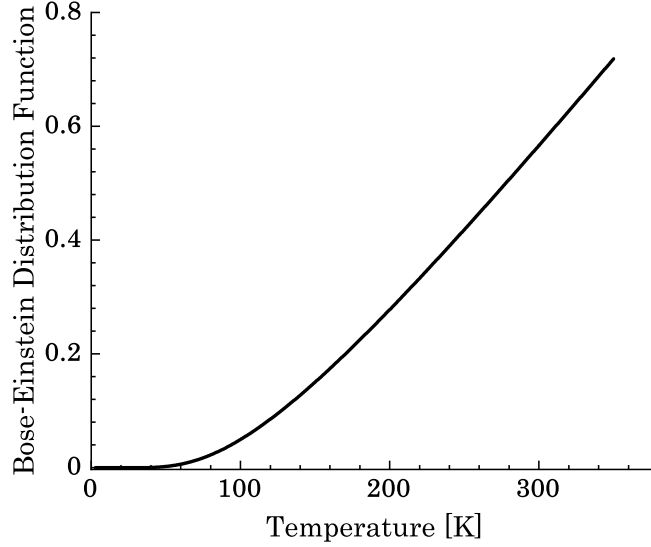


Figure 2.7: Bose-Einstein distribution function plotted against temperature. The plot was generated using the LO phonon energy of CsPbI₃, $\hbar\omega_{LO} = 26.3 \text{ meV}$ ⁸².

The absorption of an LO phonon by a charge carrier is only possible if LO phonon modes are thermally excited and becomes likelier the more modes are excited.^{38,112} Effectively, the LO phonon absorption rate is proportional to n_{LO} . LO phonon emission on the other hand can occur in two ways: spontaneously or stimulated. The former is independent of n_{LO} and is essentially possible at all temperatures as long as the carrier has sufficient energy to emit an LO phonon, i.e. $E \geq \hbar\omega_{LO}$. The latter, on the other hand, is again reliant on the presence of excited LO phonon modes and thus also proportional to n_{LO} .

The contributions of LO phonon absorption and emission to the Fröhlich scattering rate can be identified as the first and second term, respectively, in Equation 2.55, as well as in Equation 2.58:¹⁰⁵ $\vec{k} \rightarrow \vec{k} + \vec{q}$ in the first term indicates the transition of a carrier from state \vec{k} to $\vec{k} + \vec{q}$ and respective energy $E_{\vec{k}}$ to $E_{\vec{k}+\vec{q}}$ through LO phonon absorption. This term is proportional to n_{LO} . LO phonon emission ($\vec{k} \rightarrow \vec{k} - \vec{q}$, $E_{\vec{k}} \rightarrow E_{\vec{k}-\vec{q}}$) is expressed in the second term, where $n_{LO} + 1$ accounts for stimulated and spontaneous emission, respectively. Importantly, the emission term has to be omitted for carrier energies below the threshold for

LO phonon emission ($E < \hbar\omega_{LO}$), because in this case, stimulated, as well as spontaneous LO phonon emission are prohibited by energy conservation. This is accounted for by the step function $\Theta(E - \hbar\omega_{LO})$. It is zero if $E < \hbar\omega_{LO}$ and one otherwise. Consequently, for carrier energies smaller than LO phonon energies,

$$W_{E < \hbar\omega_{LO}} \propto n_{LO}, \quad (2.57)$$

which states that the Fröhlich scattering rate is linearly dependent on the LO phonon occupation number and therefore has a temperature dependence as dictated by the Bose-Einstein distribution function (c.f. Equation 2.56 and Figure 2.7).

The solution to Equation 2.55 can be found by inserting the matrix element (Equation 2.54), substituting $d\vec{q}$ for $d\vec{k}$ and solving the integral over \vec{q} . Omitting screening effects, the final equation of the carrier-LO phonon scattering rate is¹⁰⁵

$$\begin{aligned} W(E(\vec{k})) &= \\ &= \frac{e^2 \omega_{LO}}{2\pi\hbar} \sqrt{\frac{m^*}{2E}} \left(\frac{1}{\varepsilon_\infty} - \frac{1}{\varepsilon_0} \right) \left[n_{LO} \sinh^{-1} \left(\frac{E}{\hbar\omega_{LO}} \right)^{\frac{1}{2}} + \Theta(E - \hbar\omega_{LO}) (n_{LO} + 1) \sinh^{-1} \left(\frac{E}{\hbar\omega_{LO}} - 1 \right)^{\frac{1}{2}} \right] \\ &= W_0 \sqrt{\frac{\hbar\omega_{LO}}{E}} \left[\underbrace{n_{LO} \sinh^{-1} \left(\frac{E}{\hbar\omega_{LO}} \right)^{\frac{1}{2}}}_{\text{absorption}} + \underbrace{\Theta(E - \hbar\omega_{LO}) (n_{LO} + 1) \sinh^{-1} \left(\frac{E}{\hbar\omega_{LO}} - 1 \right)^{\frac{1}{2}}}_{\text{emission}} \right] \end{aligned} \quad (2.58)$$

In the last row of Equation 2.58 energy independent parameters are collected in W_0 , which is defined as

$$W_0 = \frac{e^2 \sqrt{2m^* \hbar\omega_{LO}}}{4\pi\hbar^2} \left(\frac{1}{\varepsilon_\infty} - \frac{1}{\varepsilon_0} \right). \quad (2.59)$$

Considering how the carrier-LO phonon scattering rate via Fröhlich interaction (Equation 2.58) depends on the energy of the charge carrier, Figure 2.8 shows $\frac{W}{W_0}$ versus $\frac{E}{\hbar\omega_{LO}}$ (dark green line denoted by “Total”) and the individual contributions from the LO phonon absorption, spontaneous and stimulated emission terms (remaining green lines). Figure 2.8 demonstrates nicely, that for carrier energies below the threshold for LO phonon emission, i.e. $\frac{E}{\hbar\omega_{LO}} < 1$, the total scattering rate (dark green curve) follows the course of the LO phonon absorption curve. The adjacent steep increase in the scattering rate begins at $\frac{E}{\hbar\omega_{LO}} = 1$, when both, spontaneous and stimulated LO phonon emission commence.

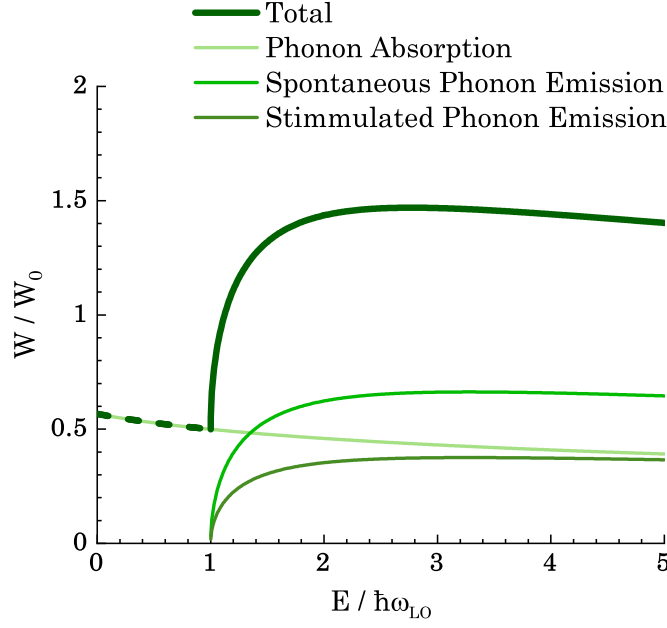


Figure 2.8: LO phonon scattering rate versus carrier energy. Rate for carrier-LO phonon scattering in CsPbI₃ at 300K. Equation 2.58 is plotted for an LO phonon energy of CsPbI₃, $\hbar\omega_{LO} = 26.3 \text{ meV}$ ⁸² and $T = 300 \text{ K}$. Displayed are the total scattering rate (darkest green, thick) along with all individual contributions stemming from the absorption (bright green), spontaneous (intermediate green) and stimulated emission (dark green) terms.

Returning to Equation 2.59, it is informative to note, that a slight transformation of the equation has a physical interpretation. Namely, $\alpha = \frac{W_0}{2\omega_{LO}}$ is the Fröhlich coupling strength, also referred to as polaron coefficient.^{105,112} Evaluating it for an electron (hole) in CsPbI₃, using the effective electron (hole) mass $m_e^* = 0.22 m_0$ ^{123,124} ($m_h^* = 0.14 m_0$ ^{123,124}) and the LO phonon energy $\hbar\omega_{LO} = 26.3 \text{ meV}$ ⁸², yields $\alpha_{CsPbI_3}^{e^-} = 1.62$ ($\alpha_{CsPbI_3}^h = 1.30$). These values are comparable to that computed for MAPbI₃, $\alpha_{MAPbI_3} = 2.34$ ⁸⁹, but significantly larger than of GaAs, $\alpha_{GaAs} = 0.088$ ¹¹². This discrepancy is expected, because LHPs are ionic semiconductors, whereas III-V compounds, such as GaAs, are an intermediate type between covalent and ionic semiconductors and thus weakly polar.^{105,112} Furthermore, the carrier mobility, which is antiproportional to α , is much higher in GaAs ($\sim 10000 \text{ cm}^2 \text{ V}^{-1} \text{ s}^{-1}$ ¹¹²), compared to lead-iodide perovskites ($\sim 100 \text{ cm}^2 \text{ V}^{-1} \text{ s}^{-1}$ in MAPbI₃⁸⁹). The significantly larger Fröhlich coupling strength in LHPs compared to that of GaAs, once again confirms that charge carrier-phonon coupling via Fröhlich interaction is substantial in ionic semiconductors, such as LHPs.^{82,89}

Coming back to Equation 2.55, it not only allows for the derivation of the LO phonon scattering rate (Equation 2.58), but also for that of the momentum relaxation rate. The latter is of particular importance in the context of this work, as the EY spin relaxation mechanism is based upon it. However, its derivation is somewhat more complicated, because the amount of

momentum transfer between phonon and charge carrier in the process of scattering depends on their relative travelling directions. Hence, a fractional increase/ decrease of momentum of $\pm \frac{q}{k} \cos \theta$ is transferred from phonon (\vec{q}) to electron (\vec{k}), in the electron's direction of motion upon absorption (+)/ emission (-) of a phonon, where θ is the angle enclosed by \vec{k} and \vec{q} . The term $\cos \theta$ results from momentum and energy conservation and is given in Table 2.2. With this, the momentum relaxation rate can be derived and results in¹⁰⁵

$$\frac{1}{\tau_m} = W_0 \sqrt{\frac{\hbar \omega_{LO}}{4E}} \left[\underbrace{n_{LO} \left(\left(1 + \frac{\hbar \omega_{LO}}{E} \right)^{\frac{1}{2}} - \frac{\hbar \omega_{LO}}{E} \sinh^{-1} \left(\frac{E}{\hbar \omega_{LO}} \right)^{\frac{1}{2}} \right)}_{\text{absorption}} + \underbrace{\Theta(E - \hbar \omega_{LO}) (n_{LO} + 1) \left(\left(1 - \frac{\hbar \omega_{LO}}{E} \right)^{\frac{1}{2}} + \frac{\hbar \omega_{LO}}{E} \sinh^{-1} \left(\frac{E}{\hbar \omega_{LO}} - 1 \right)^{\frac{1}{2}} \right)}_{\text{emission}} \right] \quad (2.60)$$

How this momentum relaxation rate is commonly used to express the Elliot-Yafet spin relaxation rate, will be elaborated in Section 2.5.

2.4 Carrier Spin Relaxation in Semiconductors

Phonon mediated charge carrier dynamics, as discussed above, have been so far considered independently from the charge carrier spin. However, investigation of charge carrier spin dynamics provide important complementary information about internal processes of photoexcited semiconductor systems.¹¹² A profound understanding of spin phenomena in semiconductors is essential for their application in the promising field of spintronics, as introduced in Chapter 1.

The successful execution of the technique “optical orientation” in semiconductors in 1968 paved the way for exploring carrier spin dynamics with a time resolution of up to picoseconds, which was inaccessible to the traditional electron spin resonance (ESR) technique at the time.¹²⁵ This stimulated a number of studies on spin relaxation processes in III-V semiconductors, which brought forth theoretical spin relaxation models explaining the new experimental data. A collection of the most important of these is shown here.

- In the **Elliott-Yafet (EY) mechanism** (Elliott, 1954¹²⁶ and Yafet, 1963¹²⁷), spin relaxation of free charge carriers occurs during momentum scattering as a result of lattice-induced SOC.^{38,125} As SOC mixes spin up and spin down wave functions, disorientation of the carrier spin becomes possible in the process of momentum scattering, even if the involved scattering potential does not act directly on the carrier spin. The EY theory takes account of scattering by acoustic and optical phonons, as well as by impurities.
- The **D'yakonov-Perel' (DP) mechanism** (D'yakonov and Perel', 1971^{128,129}) occurs in crystals without inversion center.^{125,130} In such crystals, a spin splitting of the energy band for all $\vec{k} \neq 0$ is present, implying that opposite spin states exhibit different energies at the same wave vector \vec{k} . This is equivalent to an effective crystal-internal magnetic field with magnitude and orientation dependent on \vec{k} . As a result, the spin axis of a free charge carrier precesses around the effective magnetic field. Meanwhile, its optically induced ensemble spin polarization diminishes. The DP mechanism is therefore also referred to as precession spin relaxation mechanism of free charge carriers.
- The **Bir-Aronov-Pikus (BAP) mechanism** (Bir, Aronov and Pikus, 1975^{131,132}) accounts for spin flip transitions due to Coulomb mediated exchange interaction between electrons and holes.¹²⁵ The exchange interaction is the binding force between an electron and hole in an exciton. It is furthermore particularly strong in heavily p-doped semiconductors, exhibiting a high number of free holes. Spin relaxation in these examples is therefore primarily driven by the BAP mechanism.
- **Hyperfine interaction** is a purely magnetic phenomenon and describes the mutual interaction between electron and nuclei magnetic momentum.¹⁰⁵ It can be the main cause of spin relaxation for electrons localized in quantum wells and quantum dots, or for those bound to donors.^{125,133} However, free electrons in metals or bulk semiconductors are hardly affected by this interaction, as it is short ranged and thus too weak to cause effective spin relaxation.

Those long-standing models successfully describe the underlying processes of spin-related optoelectronic characteristics of conventional III-V semiconductors. Naturally, the overarching question arises, whether those models are also applicable to LHPs. Intense research on LHPs in recent years brought forth that their optoelectronic properties in many aspects compare to those of III-V compounds.²⁷ Therefore, LHPs may be regarded as close cousins to conventional III-V semiconductors, thus allowing for a tentative and conscious application of those models to LHPs.²⁷

Today, the study of spin-related phenomena in LHPs is at the forefront of current research. In the following paragraph, a collection of these studies is given, summarizing major results and open questions on spin dynamics in LHPs.

By now, a broad consensus about spin relaxation times, τ_s , in LHPs appears to have been approached. They are manifold reported to be of the order of a few picoseconds for thin-films and NCs, all measured through circularly polarized DTS at room temperature.^{134–137} Nevertheless, τ_s is influenced by LHP composition. Comparing ABX₃ thin films incorporating A = MA, Cs, B=Pb and X = Br, I, spin relaxation times increase from 1.3 ps to 4.3 ps in the order $\tau_s^{\text{CsPbI}_3} < \tau_s^{\text{MAPbI}_3} < \tau_s^{\text{CsPbBr}_3} < \tau_s^{\text{MAPbBr}_3}$.¹³⁵ Exchanging the heavy metal lead (Pb) by the lighter tin (Sn), both elements belonging to the same periodic group (IV), increases the spin relaxation time significantly.¹³⁷ CsSnBr₃ NCs for example yield $\tau_s^{\text{CsSnBr}_3} = 18 \pm 2 \text{ ps}$. According to these studies, the strongest effect on the spin relaxation time is ascribed to the choice of metal cation, followed by the choice of halide anion. A-site cations influence spin relaxation time only weakly. This indicates that spin relaxation dynamics are predominantly impacted by the LHP band structure, which is determined by the (BX₆)⁴⁻ octahedra. Furthermore, the strong dependence of τ_s on the molar mass of B- and X-site constituents evidences the dominant role SOC plays in spin relaxation in LHPs. This is because a semiconductor's intrinsic spin-orbit splitting correlates with its constituent's mass, as established in Subsection 2.1.3. To give an example, the spin-orbit splitting of CsSnBr₃ ($\Delta_{SO}^{\text{CsSnBr}_3} \approx 0.43 \text{ eV}$ ¹³⁷) is roughly 3.7-fold smaller compared to that of CsPbBr₃ ($\Delta_{SO}^{\text{CsPbBr}_3} \approx 1.61 \text{ eV}$ ³⁴).¹³⁸ Spin relaxation processes, which rely on SOC, can thus be influenced by the choice of crystal constituents, i.e. lighter elements induce smaller spin-orbit splitting in LHPs, leading to a prolongation of spin relaxation time.

Regarding crystal dimension, it has been found that strong quantum confinement accelerates spin relaxation.^{136,139} Spin relaxation times were systematically studied for CsPbBr₃ and CsPbI₃ QDs of various sizes. It was found that a reduction in edge length from $\approx 8 \text{ nm}$ to $\approx 4 \text{ nm}$ reduces the spin relaxation time from $\tau_s \approx 1.9 \text{ ps}$ to $\approx 1.2 \text{ ps}$ in CsPbBr₃ QDs, and from $\tau_s \approx 3.2 \text{ ps}$ to $\approx 1.9 \text{ ps}$ in CsPbI₃ QDs.¹³⁶ The same trend is found in the single crystalline Ruddlesden–Popper perovskite PEA₂PbI₄(MAPbI₃)_{n-1} as the number of layers, n, is reduced.¹³⁹ While $\tau_s \approx 7 \text{ ps}$ for $n \approx 4$, spin relaxation becomes faster and yields $\tau_s \approx 0.3 \text{ ps}$ for $n \approx 1$. The latter spin relaxation time is consistent with a study on 2D layered (C₆H₅C₂H₄NH₃)₂PbI₄ thin films, where $\tau_s = 0.24 \pm 0.01 \text{ ps}$ has been deduced.¹⁴⁰ These studies consistently show that spin relaxation times reduce upon size reduction of small NCs/ QDs. In summary, enhancement of quantum confinement accelerates spin relaxation in LHPs. The authors of these studies name the following possible reasons to explain the described phenomenon: scattering with QD

surfaces,^{136,139} spin-spin interactions with surface dangling bonds, and Coulomb exchange interaction (BAP mechanism).^{139,140} The latter becomes evident when considering that the exciton energy increases upon size reduction of the respective particle (c.f. Equation 2.7). Indeed, in the mentioned 2D layered $(C_6H_5C_2H_4NH_3)_2PbI_4$ thin films, the exciton binding energy reaches values as large as 180 meV.¹⁴⁰ As a reference, this enormous exciton binding energy exceeds that in bulk $CsPbI_3$ ten-fold. Hence, strong quantization and entailed large exciton energies might be a key parameter in determining the dominating spin relaxation mechanism in a material.

The described effect of strong quantization on spin relaxation must not be confused with that of small to moderate quantization: For spin relaxation being predominantly phonon assisted, moderate quantum confinement is generally an effective way to prolong spin relaxation. This is because moderate confinement initiates discrete (versus continuous), atom-like energy levels.¹⁴¹ As a result carrier-phonon scattering is suppressed, because it becomes less likely that phonon energies match intralevel transition energies – a phenomenon called “phonon bottleneck” and well known from III-V semiconductors. This way the EY mechanism can be suppressed. Indeed, $CsPbI_3$ NCs show a prolonged spin relax time compared with their bulk counterpart, speaking for EY to be the dominant spin relax mechanism in this material under moderate or absent quantization.¹³⁶ In contrast, spin relaxation times in $CsPbBr_3$ are shorter in NCs compared to in bulk, indicating spin relaxation due to phonon scattering in form of the EY mechanism to be rather negligible. Further evidence for lead-iodide and lead-bromide LHPs ($APbI_3$ and $APbBr_3$, $A = MA, Cs$) being dominated by different spin relaxation mechanisms is that the former show prolonged spin relaxation as the phonon occupation is reduced by lowering the temperature, while spin relaxation times in the latter are not affected by temperature.¹³⁵ This again supports the evidence that the EY mechanism is dominant and negligible in $APbI_3$ and $APbBr_3$, respectively.

It has been shown that spin relaxation times in LHPs stay constant for small photoexcitation fluences,¹³⁷ but shorten as the fluence increases to high levels.¹³⁴ This indicates that at high laser intensities carrier-carrier scattering additionally contributes to carrier spin relaxation, while being negligible at small laser intensities.

In the helicity dependent pump-probe experiments of the above discussed studies no external magnetic fields were incorporated. If, however, the sample under investigation is wished for being subjected to a homogeneous magnetic field, two options arise: The magnetic field is applied along (Faraday geometry), or perpendicular (Voigt geometry) to the observation direction. If the pump-probe experiment is in Faraday geometry, the photoexcited ensemble

of charge carriers comprises of a highly non-equilibrium spin distribution, whose relaxation involves energy transfer to the lattice via phonon scattering.¹⁴² The associated time constant T_1 is referred to as longitudinal, or spin-lattice relaxation time. For a pump-probe experiment in Voigt geometry, the pump-induced charge carrier spins are in a superposition of spin up and spin down state.¹⁴² Initially, these states precess in phase about the field vector of the externally applied magnetic field in a plane normal to it. All these spins add constructively, which yields an optically induced net magnetization, that temporally evolves at Larmor frequency. The decay of the net magnetization reflects the spin decoherence of individual charge carriers and the associated lifetime T_2 is referred to as transverse spin relaxation time, or phase relaxation time. It is caused mostly by spin-spin interactions and is thus a much faster process compared to phonon induced longitudinal spin relaxation, i.e. $T_1 \gg T_2$.

In polarization dependent pump-probe experiments without any external magnetic field, the spin ensemble does not Larmor precess as described above. Measuring spin relaxation due to dephasing, T_2 , is thus not available. Rather, spin relaxation times deduced from such experiments corresponds to T_1 .¹³⁴ Therefore, in the following studies, which incorporate a magnetic field in their pump-probe experiments, the focus is put on the results of T_1 , rather than T_2 .

Spin relaxation in CsPbBr₃ single crystals was measured through polarization sensitive pump-probe spectroscopy, while exposing the sample to magnetic fields of up to $4T$.³⁶ The measured long-lasting spin relaxation time lies in the range of 32 to 53 ns at cryogenic temperature, i.e. $T \leq 5K$. The group attributes it to hyperfine interaction between localized charge carriers and nuclei spins. For localized electrons in bulk GaAs, InP and CdTe, it has been shown that an external magnetic field may suppress spin relaxation via hyperfine interaction.¹⁴³ Spin relaxation in the latter studies lasts even longer and reaches values of the order of milliseconds. It is clear, that spin relaxation governed by hyperfine interaction is prolonged by an external magnetic field, as it interferes with the purely magnetic hyperfine interaction between electron and nuclei magnetic momentum. Hyperfine interaction is a strong, but short ranged interaction and thus the main cause of spin relaxation for localized electrons, while being negligible for free electrons.^{125,133}

Notably, spin relaxation times can significantly exceed the lifetime of the photoinduced electron-hole pairs.³⁶ This is a further evidence, that the detected long-lasting spin relaxation times do not arise directly from optical orientation. Instead, the spin polarization of photoinduced carriers measured in these experiments is transferred to localized carriers, which far outlive the incident photoexcited electron-hole pairs. Therefore, spin polarization can remain in the system even after carrier recombination, explaining the long-lasting spin relaxation

times reported in these studies. To date, the initial spin relaxation processes, which arise directly from photocreated electron-hole pairs require further research, as they have not been fully understood yet, nor have they been unambiguously assigned a dominating spin relaxation mechanism.

From the given collection of exemplary studies it can be deduced that efforts have been made to unravel the laws of spin relaxation in LHPs, but at the time it remains only partially understood. Summarizing and converging the results of the above studies leads to what is commonly accepted as of today: One, the choice of metal cation and halide anion determine the intrinsic spin-orbit splitting and strongly affect spin relaxation dynamics. Two, spin relaxation is influenced by quantum confinement in two ways: strong quantum confinement drastically enlarges the exciton energy in LHPs and accelerates spin relaxation, while small to moderate quantum confinement suppresses and thus prolongs phonon assisted spin relaxation. Three, it is understood that large carrier densities contribute to spin relaxation via carrier-carrier scattering.

The governing spin relaxation mechanism, thus, predominantly depends on LHP constituents, crystal size, temperature, and photoexcitation intensity. A fundamental and quantitative understanding of how these conditions impact spin relaxation and the unambiguous assignment to the dominating spin relaxation mechanism is, however, still missing. Therefore, from here on, the target is to investigate and contribute exactly that in CsPbI₃ NCs.

Out of the above listed spin-relaxation mechanisms only the EY and DP mechanism are concerned with free charge carriers¹²⁵ and thus applicable to describe spin dynamics in un- and slightly confined CsPbI₃ NCs (low cryogenic temperatures excepted). However, in principle, the DY theory can be excluded, as it acts in crystals exhibiting inversion symmetry breaking, which is not the case for the centrosymmetric CsPbI₃ NCs (c.f. Subsection 2.1.2). It is nevertheless instructive to elucidate the key differences between those two spin relaxation mechanisms, as it is still under debate, if Rashba-type effects are present in LHPs, which would involve inversion symmetry breaking.¹⁴⁴ Thus, an immediate comparison of EY and DP theory helps to assign the suitable one to my experimental data. In Chapter 5 this then allows for the exclusion of the DY mechanism not only through theoretical arguments, but also through experimental evidence.

Comparing the mathematical expressions describing EY and DP spin relaxation reveals their principally opposite dependency on momentum scattering.¹²⁵ While the EY spin relaxation rate increases with a higher carrier scattering rate, $\frac{1}{\tau_{EY}} \propto \frac{1}{\tau_m}$, it decreases in the DP model,

$\frac{1}{\tau_{DP}} \propto \tau_m$. The microscopic origin for this is that DP spin relaxation takes place between, rather than during scattering events. Consequently, with an increasing momentum scattering rate, e.g. as a result of a high phonon concentration, the efficiency of the EY mechanism increases and that of the DP mechanism decreases. On rising temperature, both mechanisms predict a rapid increase in spin relaxation, however, with different dependencies, i.e. $\frac{1}{\tau_{EY}} \propto \frac{1}{\tau_m} T^2$ and $\frac{1}{\tau_{DP}} \propto \tau_m T^3$.

For the sake of completeness, I want to briefly address under which conditions the BAP mechanism and/ or hyperfine interaction may control spin relaxation even in CsPbI₃. These conditions may be significant quantum confinement, or low cryogenic temperatures, as in both cases charge carriers tend to increasingly coalesce and form excitons. It is for example known that at cryogenic temperatures, in III-V compounds the BAP mechanism gains importance even in bulk structures.¹²⁵ This means that in increasingly cold ambience spin relaxation due to exchange interaction between electron and hole commences to compete with phonon-assisted spin relaxation. Additionally, it has been reported, that at $T < 30 - 40$ K, the detected increasing spin relaxation rate is a consequence of electron localization at low temperatures.¹²⁵ This way, spin relaxation may be governed by hyperfine interaction between the localized electron spin with magnetic momenta of lattice nuclei.

From here on, the focus will be returned to the investigation of free charge carrier spin relaxation, as justified above and motivated in Subsection 2.1.1.

2.5 Elliott-Yafet Spin Relaxation Theory

In order to predict the rate of charge carrier spin relaxation in a certain material, it is essential to firstly identify the dominating mechanism behind it by comparing experimental data to spin relaxation theory. In my first-author publication on “spin polarization dynamics of free charge carriers in CsPbI₃ NCs”¹¹³ we present that the EY mechanism dominates spin relaxation. Therefore this theory is elucidated in detail in this section.

The EY theory was derived to describe spin relaxation in III-V semiconductors.^{105,122,125} The VB in this group of materials has p-symmetry and is thus influenced significantly by SOC, splitting it into heavy hole, light hole and split-off band (c.f. Figure 2.3). In the latter two, spin up and spin down states are mixed, even at $\vec{k} = 0$.¹⁰⁵ As a result, holes are subject to ultra fast spin randomization.^{38,145} By contrast, there is no mixing of CB spin states at $\vec{k} = 0$, i.e. $j = s$, because the CB has s-symmetry. Deviating from the zone center, i.e. at $\vec{k} \neq 0$, spin up

and spin down states mix as a consequence of SOC.¹⁰⁵ Spin relaxation in the CB, thus, occurs on a significantly slower time scale and is described by mechanisms, such as those listed in Section 2.4.^{38,145}

Due to the similarity of the band structures of III-V semiconductors and perovskites, which is merely reversed (c.f. Figure 2.3), the above argumentation can be adopted for CB electrons and VB holes in LHPs. In LHPs, it is the CB, which exhibits p-symmetry. The lowest CB is the split-off band, distanced from the light and heavy electron bands by Δ_{SO} . Within the lowest CB, spins are mixed, even at $\vec{k} = 0$ (c.f. Equation 2.13), analogous to the split-off VB in III-V compounds. Accordingly, CB electrons in LHPs are subject to ultra fast spin randomization. By contrast, there is no mixing of VB spin states in LHPs at $\vec{k} = 0$, i.e. $j = s$ (c.f. Equation 2.12), analogous to the CB in III-V compounds. Again, spin up and spin down states are mixed only for $\vec{k} \neq 0$. Consequently, hole spin relaxation is expected to occur on a significantly slower time scale than electron spin relaxation. Tentatively, spin relaxation in the LHP VB can therefore also be described by the spin relaxation mechanisms derived for CB electrons in III-V semiconductors.

The EY mechanism predicts that carrier - phonon scattering impacts charge carrier spin. Consequently, the Ansatz for the EY spin scattering rate is equivalent to that of carrier - phonon scattering in Equation 2.55.^{105,122}

$$W_{EY}(\vec{k}) = \frac{2\pi}{\hbar} \int |\langle f | \hat{H}_{Fröhlich} | i \rangle|^2 \delta(E_f - E_i) dN_f \quad (2.61)$$

N_f denotes the number of final electron (hole) states in the CB (VB) in III-V compounds (LHPs). As opposed to carrier-phonon scattering, spin scattering requires initial (i) and final (f) states to be considered spin sensitive. As the Fröhlich scattering potential is assumed to not directly act on the spin state, the matrix element in Equation 2.61 can be divided into a spin insensitive and a spin sensitive component^{105,122}

$$\langle f | \hat{H}_{Fröhlich} | i \rangle = \langle F_{\vec{k}'} | \hat{H}_{Fröhlich} | F_{\vec{k}} \rangle \left({}_{CB} \langle u_{\vec{k}'}(\uparrow) | u_{\vec{k}}(\uparrow) \rangle_{CB} + {}_{CB} \langle u_{\vec{k}'}(\downarrow) | u_{\vec{k}}(\uparrow) \rangle_{CB} \right). \quad (2.62)$$

$F_{\vec{k}}$ are spin insensitive envelope functions multiplying the respective spin sensitive eigenfunctions $u_{\vec{k}}$. The CB (VB in LHPs) eigenfunctions $u_{\vec{k}}$ are mixed in spin only if $\vec{k} \neq 0$. (At the zone center they are pure in spin as given by Equation 2.12.) $u_{\vec{k}}$ are eigenfunctions of the

Hamiltonian \hat{H}^{total} and satisfy the Schrödinger equation^{105,146}

$$\hat{H}^{\text{total}} = \underbrace{\frac{p^2}{2m_0} + V(\vec{r})}_{\hat{H}_0} + \underbrace{\frac{\hbar}{m_0} \vec{k} \vec{p} + \frac{\hbar^2 k^2}{2m_0}}_{\hat{H}_k} + \underbrace{\frac{\hbar}{4m_0^2 c^2} \nabla V(\vec{r}) \times \vec{p} \vec{\sigma}}_{\hat{H}_{SO}}.$$

$$\hat{H}^{\text{total}} |\vec{u}_{\vec{k}}\rangle = E_{\vec{k}} |\vec{u}_{\vec{k}}\rangle \quad (2.63)$$

m_0 is the free electron (hole) mass, $V(\vec{r})$ a periodical crystal potential, and $\vec{\sigma}$ are the Pauli matrices. The total Hamiltonian is comprised of three constituents: the unperturbed Hamiltonian (\hat{H}_0), a perturbation Hamiltonian (\hat{H}_k) including one term of linear and one of quadratic dependence on \vec{k} following Kane's $\vec{k} \cdot \vec{p}$ theory, and finally a perturbation Hamiltonian taking into account spin-orbit coupling effects (\hat{H}_{SO}).^{146,147} The solution of the Schrödinger equation

$$\hat{H}_0 |\vec{u}_n\rangle = E_n |\vec{u}_n\rangle \quad (2.64)$$

is assumed to be known, enabling one to use the complete set of $|\vec{u}_n\rangle$ as a basis. The eight basis vectors are

$$\begin{aligned} |u_{c1}\rangle &= i|S, \uparrow\rangle, |u_{v1}\rangle = -\frac{1}{\sqrt{2}}|X + iY, \uparrow\rangle, |u_{v2}\rangle = \frac{1}{\sqrt{2}}|X - iY, \uparrow\rangle, |u_{v3}\rangle = |Z, \uparrow\rangle, \\ |u_{c2}\rangle &= i|S, \downarrow\rangle, |u_{v4}\rangle = \frac{1}{\sqrt{2}}|X - iY, \downarrow\rangle, |u_{v5}\rangle = -\frac{1}{\sqrt{2}}|X + iY, \downarrow\rangle, |u_{v6}\rangle = |Z, \downarrow\rangle. \end{aligned} \quad (2.65)$$

The eigenvalues of the first four basis states are respectively degenerate with the last four basis states. With this basis the total Hamiltonian for cubic crystals reads¹⁰⁵

$$\hat{H}_{8 \times 8}^{\text{total}} = \begin{bmatrix} E_c & -\frac{k_+ P}{\sqrt{2}} & \frac{k_- P}{\sqrt{2}} & k_z P & 0 & 0 & 0 & 0 \\ -\frac{k_- P}{\sqrt{2}} & E_v + \frac{\Delta_{SO}}{3} & 0 & 0 & 0 & 0 & 0 & 0 \\ \frac{k_+ P}{\sqrt{2}} & 0 & E_v - \frac{\Delta_{SO}}{3} & 0 & 0 & 0 & 0 & \sqrt{2} \frac{\Delta_{SO}}{3} \\ k_z P & 0 & 0 & E_v & 0 & 0 & \sqrt{2} \frac{\Delta_{SO}}{3} & 0 \\ 0 & 0 & 0 & 0 & E_c & \frac{k_- P}{\sqrt{2}} & -\frac{k_+ P}{\sqrt{2}} & k_z P \\ 0 & 0 & 0 & 0 & \frac{k_+ P}{\sqrt{2}} & E_v + \frac{\Delta_{SO}}{3} & 0 & 0 \\ 0 & 0 & 0 & \sqrt{2} \frac{\Delta_{SO}}{3} & -\frac{k_- P}{\sqrt{2}} & 0 & E_v - \frac{\Delta_{SO}}{3} & 0 \\ 0 & 0 & \sqrt{2} \frac{\Delta_{SO}}{3} & 0 & k_z P & 0 & 0 & E_v \end{bmatrix}$$

Its eigenvalues $E_{\vec{k}}$ are deduced by solving $\det(\hat{H}_{8 \times 8}^{\text{total}} - E_{\vec{k}} \mathbb{1}_{8 \times 8}) = 0$. As the goal is to describe how CB electrons (VB holes in LHPs) are affected by the EY mechanism (Equation 2.61), the eigenvalues and eigenvectors of $\hat{H}_{8 \times 8}^{\text{total}}$ will be explicitly formulated. The former is calculated to be¹⁰⁵

$$E_{\vec{k},CB} = E_c + \frac{\hbar^2 k^2}{2m_0} + \frac{P^2 \left(E_g + 2\frac{\Delta_{SO}}{3}\right) k^2}{\left(E_g + 2\frac{\Delta_{SO}}{3}\right) \left(E_g + \frac{\Delta_{SO}}{3}\right) - 2\left(\frac{\Delta_{SO}}{3}\right)^2}. \quad (2.66)$$

When factoring out k^2 , Equation 2.66 takes on a more compressed form

$$E_{\vec{k},CB} = E_c + \frac{\hbar^2 k^2}{2m^*}, \quad (2.67)$$

with

$$\frac{1}{m^*} = \frac{1}{m_0} + \frac{\left(E_g + 2\frac{\Delta_{SO}}{3}\right) 2P^2}{\left[\left(E_g + 2\frac{\Delta_{SO}}{3}\right) \left(E_g + \frac{\Delta_{SO}}{3}\right) - 2\left(\frac{\Delta_{SO}}{3}\right)^2\right] \hbar^2}. \quad (2.68)$$

This allows to find an expression for P^2 , namely

$$P^2 = \left(\frac{1}{m^*} - \frac{1}{m_0}\right) \frac{\left[\left(E_g + 2\frac{\Delta_{SO}}{3}\right) \left(E_g + \frac{\Delta_{SO}}{3}\right) - 2\left(\frac{\Delta_{SO}}{3}\right)^2\right] \hbar^2}{2\left(E_g + 2\frac{\Delta_{SO}}{3}\right)}. \quad (2.69)$$

This expression will be needed in the proceeding calculation.

Subsequently, the corresponding eigenstates $|\vec{u}_{\vec{k}}\rangle$ ¹⁰⁵ can be deduced by inserting the found eigenvalue (Equation 2.66) into the equation $\left(\hat{H}_{8 \times 8}^{\text{total}} - E_{\vec{k},CB} \mathbb{1}_{8 \times 8}\right) |\vec{u}_{\vec{k}}\rangle_{CB} = 0$. It is noteworthy, that the following eigenstates are both energy eigenstates of the same energy eigenvalue found in Equation 2.66. This contains an important message, namely that although differing in spin, the energy of both eigenstates is the same, i.e. degenerate.

$$\begin{aligned} |u_{\vec{k}}(\uparrow)\rangle_{CB} &= a|u_{c1}\rangle + b|u_{v1}\rangle + c|u_{v2}\rangle + d|u_{v3}\rangle + e|u_{v5}\rangle + f|u_{v6}\rangle \\ |u_{\vec{k}}(\downarrow)\rangle_{CB} &= a|u_{c2}\rangle - b^*|u_{v4}\rangle - c^*|u_{v5}\rangle + d|u_{v6}\rangle + e|u_{v2}\rangle - f^*|u_{v3}\rangle, \end{aligned} \quad (2.70)$$

with

$$\begin{aligned} a &= \frac{\left(E_g + \frac{\Delta_{SO}}{3}\right) \left(E_g + 2\frac{\Delta_{SO}}{3}\right) - 2\left(\frac{\Delta_{SO}}{3}\right)^2}{D}, \quad b = -\frac{k_- P}{\sqrt{2}E_g} a, \quad c = \frac{k_+ P}{\sqrt{2}D} \left(E_g + \frac{\Delta_{SO}}{3}\right), \\ d &= \frac{k_z P}{D} \left(E_g + 2\frac{\Delta_{SO}}{3}\right), \quad e = \sqrt{2} \frac{k_z P \Delta_{SO}}{D \cdot 3}, \quad f = \frac{k_+ P \Delta_{SO}}{D \cdot 3} \end{aligned} \quad (2.71)$$

and

$$D^2 = \left[\left(E_g + \frac{\Delta_{SO}}{3} \right) \left(E_g + 2 \frac{\Delta_{SO}}{3} \right) - 2 \left(\frac{\Delta_{SO}}{3} \right)^2 \right]^2 \left(1 + \frac{k_{\perp}^2 P^2}{2E_g^2} \right) + \left[\left(E_g + \frac{\Delta_{SO}}{3} \right)^2 + 2 \left(\frac{\Delta_{SO}}{3} \right)^2 \right] \frac{k_{\perp}^2 P^2}{2} + \left[\left(E_g + 2 \frac{\Delta_{SO}}{3} \right)^2 + 2 \left(\frac{\Delta_{SO}}{3} \right)^2 \right] k_z^2 P^2. \quad (2.72)$$

Here, it was used that $k_{\perp}^2 = k_x^2 + k_y^2$. Note, that the denotation of the spin (\uparrow) in $|u_{\vec{k}}(\uparrow)\rangle_{CB}$ (Equation 2.70) may be somewhat misleading. It does not imply that the state is a pure spin up state! Rather, it implies that $|u_{\vec{k}}(\uparrow)\rangle_{CB}$ contains all spin up basis vectors ($|u_{c1}\rangle, |u_{v1}\rangle, |u_{v2}\rangle, |u_{v3}\rangle$) and furthermore two out of four spin down basis vectors ($|u_{v5}\rangle, |u_{v6}\rangle$). Analogously, (\downarrow) in $|u_{\vec{k}}(\downarrow)\rangle_{CB}$ (Equation 2.70) does not refer to a pure spin down state, but to one containing all spin down basis vectors ($|u_{c2}\rangle, |u_{v4}\rangle, |u_{v5}\rangle, |u_{v6}\rangle$) expanded by two spin up basis vectors ($|u_{v2}\rangle, |u_{v3}\rangle$). Importantly, these spin sensitive CB (VB in LHPs) states (Equation 2.70) are \vec{k} -dependent and valid not only at $\vec{k} = 0$, as those in Equation 2.12, but also for finite \vec{k} . At $\vec{k} = 0$, the states reduce to $|u_{\vec{k}=0}(\uparrow)\rangle_{CB} = |u_{c1}\rangle$ and $|u_{\vec{k}=0}(\downarrow)\rangle_{CB} = |u_{c2}\rangle$, consistent with Equation 2.12.

As my goal is to describe how CB electrons (VB holes in LHPs) are affected by the EY mechanism (Equation 2.61), the products of spin-insensitive ${}_{CB}\langle u_{\vec{k}'}(\uparrow) | u_{\vec{k}}(\uparrow) \rangle_{CB}$ and spin-sensitive ${}_{CB}\langle u_{\vec{k}'}(\downarrow) | u_{\vec{k}}(\uparrow) \rangle_{CB}$ parts of the EY matrix element in Equation 2.62 must be built.¹⁰⁵

$${}_{CB}\langle u_{\vec{k}'}(\uparrow) | u_{\vec{k}}(\uparrow) \rangle_{CB} = a'a + b'^*b + c'^*c + d'd + e'e + f'^*f \quad (2.73)$$

$${}_{CB}\langle u_{\vec{k}'}(\downarrow) | u_{\vec{k}}(\uparrow) \rangle_{CB} = -c'e + d'f + e'c - f'd, \quad (2.74)$$

where $\langle u_i | u_j \rangle = \delta_{ij}$ was applied, which holds for all basis vectors (Equation 2.65).

It is legitimate to assume kinetic energies of the CB electron (VB hole in LHPs), that are small compared with the band gap energy. In that case D^2 (Equation 2.72) reduces to

$$D^2 \approx \left[\left(E_g + \frac{\Delta_{SO}}{3} \right) \left(E_g + 2 \frac{\Delta_{SO}}{3} \right) - 2 \left(\frac{\Delta_{SO}}{3} \right)^2 \right]^2. \quad (2.75)$$

With that, the spin conserving matrix element (first term in brackets in Equation 2.73) approaches unity, i.e. ${}_{CB}\langle u_{\vec{k}'}(\uparrow) | u_{\vec{k}}(\uparrow) \rangle_{CB} \approx 1$,¹⁰⁵ and I am left with solving the matrix element describing spin-flip processes, i.e. ${}_{CB}\langle u_{\vec{k}'}(\downarrow) | u_{\vec{k}}(\uparrow) \rangle_{CB}$. Inserting $c^{(\prime)}$, $d^{(\prime)}$, $e^{(\prime)}$, $f^{(\prime)}$ from Equation 2.71 into Equation 2.74 gives

$${}_{CB}\langle u_{\vec{k}'}(\downarrow) | u_{\vec{k}}(\uparrow) \rangle_{CB} = \frac{P^2}{D^2} \frac{\Delta_{SO}}{3} (2E_g + \Delta_{SO})(k'_z k_+ - k'_+ k_z). \quad (2.76)$$

Inserting P^2 and D^2 from Equation 2.69 and Equation 2.75, respectively, leads to

$$\begin{aligned} {}_{CB}\langle u_{\vec{k}'}(\downarrow) | u_{\vec{k}}(\uparrow) \rangle_{CB} &= \left(\frac{1}{m^*} - \frac{1}{m_0} \right) \frac{\hbar^2}{2} \frac{(2E_g + \Delta_{SO}) \frac{\Delta_{SO}}{3}}{E_g \left(E_g + 2\frac{\Delta_{SO}}{3} \right) (E_g + \Delta_{SO})} (k'_z k_+ - k'_+ k_z) \\ &= \left(1 - \frac{m^*}{m_0} \right) \frac{1}{m^*} \frac{\hbar^2}{2} \frac{\eta(2-\eta)}{E_g(3-\eta)} k k' e^{i\phi} \sin\theta. \end{aligned} \quad (2.77)$$

In the second line, η substitutes $\frac{\Delta_{SO}}{E_g + \Delta_{SO}}$ and the k -dependent term has been expressed as an angular relationship of k' with k , where θ is the angle between \vec{k}' and \vec{k} , and ϕ is the angle between \vec{k}_x and \vec{k}_y . Expressing the initial kinetic energy as $E = \frac{\hbar^2 k^2}{2m^*}$, Equation 2.77 transforms to¹⁰⁵

$${}_{CB}\langle u_{\vec{k}'}(\downarrow) | u_{\vec{k}}(\uparrow) \rangle_{CB} = \left(1 - \frac{m^*}{m_0} \right) \frac{E}{E_g} \frac{\eta(2-\eta)}{(3-\eta)} \frac{k'}{k} e^{i\phi} \sin\theta. \quad (2.78)$$

The EY spin relaxation rate $\frac{1}{\tau_{EY}}$ can now be obtained by replacing the spin sensitive term of Equation 2.62 with the just derived matrix element (Equation 2.78) and subsequently inserting Equation 2.62 into the Ansatz (Equation 2.61). As the Ansatz is equivalent to that of carrier-phonon scattering, it is clear that spin relaxation due to carrier-phonon scattering is closely related to carrier-phonon scattering disregarding spin. Indeed, the spin insensitive part of the matrix element (the factor term in Equation 2.62) is equivalent to that of momentum scattering in carrier-phonon interactions (Equation 2.54),^{105,122} i.e.

$$\underbrace{\left| \langle F_{\vec{k}'} | \hat{H}_{\text{Fröhlich}} | F_{\vec{k}} \rangle \right|^2}_{\text{Equation 2.62}} = \underbrace{M_{\vec{k} \rightarrow \vec{k} \pm \vec{q}} (n_{LO} + 1/2 \mp 1/2)}_{\text{Equation 2.54}} = \underbrace{\left| \langle \vec{k} \pm \vec{q} | \hat{H}_{\text{Fröhlich}} | \vec{k} \rangle \right|^2}_{\text{Equation 2.54}}. \quad (2.79)$$

It is thus customary to express spin relaxation in terms of the momentum relaxation rate $\frac{1}{\tau_m}$ (Equation 2.60). With that, the rate of spin relaxation due to carrier-phonon scattering as predicted by the EY mechanism in the approximation of cubic crystals results in

$$\frac{1}{\tau_{EY}} = \gamma \frac{1}{\tau_m} \left(1 - \frac{m^*}{m_0} \right)^2 \left(\frac{E}{E_g} \right)^2 \frac{2\eta^2(2-\eta)^2}{(3-\eta)^2}. \quad (2.80)$$

Here, γ is a dimensionless constant of the order of one, which arises from the integration over θ . It takes different values depending on the kind of momentum scattering (electron scattering

by acoustic or optical phonons, or by impurities). In the case of momentum scattering by polar optical phonons (including LO phonons), $\gamma \approx 2$.¹²⁵

In order to work out the ex- and implicit temperature dependency of the EY spin relaxation rate, the electron kinetic energy $E = k_B T$ is inserted into Equation 2.80.¹²⁵ Keeping only temperature dependent terms, Equation 2.80 reduces to

$$\frac{1}{\tau_{EY}} \propto \frac{1}{\tau_m} T^2. \quad (2.81)$$

It needs to be pointed out, that a simple term for the spin relaxation rate as the one in Equation 2.80 can only be obtained if the involved scattering processes are presumed to be elastic, i.e. $k' = k$.¹⁰⁵ Otherwise, the rate has to be found numerically.^{105,122} Nevertheless, Equation 2.80 has been used extensively in the literature to describe spin relaxation, which is also caused by highly non-elastic processes, such as polar optical phonon scattering.^{10,125,148} As an example, LO phonon scattering is distinctly inelastic because of the considerable magnitude of $E_{LO} = \hbar\omega_{LO}$, which takes on values of typically several tens of millielectronvolts in conventional semiconductor materials,¹⁰⁵ as well as in LHPs (in CsPbI₃, $E_{LO} \approx 26.3 \pm 7.0 \text{ meV}$)⁸². The use of Equation 2.80 to describe spin relaxation, which is predominantly driven by polar phonon scattering may therefore be done only with great caution.

The numeric solution of the EY spin relaxation rate, taking into account inelastic momentum scattering, has been reported in 2004 by A. Dyson and B. K. Ridley – almost three decades after the initial description of the EY mechanism.¹²² The authors begin with the same considerations and Ansatz as presented in this section. The final expression for the EY spin relaxation rate, however, is not expressed in terms of the momentum relaxation rate, $\frac{1}{\tau_m}$, as this would again require to assume elastic scattering. Instead, their final expression strongly reminds of the equation found for the momentum scattering rate (Equation 2.60), including additional parameters stemming from the spin sensitive matrix element.

$$\frac{1}{\tau'_{EY}} = W_0 \frac{\hbar^2 \omega_{LO}^2}{E_g^2 \sqrt{\pi} (k_B T)^{3/2}} \frac{\eta^2 (2 - \eta)^2}{(3 - \eta)^2} \int e^{-\frac{E}{k_B T}} [n_{LO} A(E) + (n_{LO} + 1) B(E)] \sqrt{E} dE. \quad (2.82)$$

W_0 has already been defined during the derivation of the momentum scattering rate (Equation 2.59 in Section 2.3), and

$$\begin{aligned}
A(E) &= \left(\frac{E}{\hbar\omega_{LO}}\right)^{3/2} \left[\left(1 + \frac{\hbar\omega_{LO}}{2E}\right) \left(1 + \frac{\hbar\omega_{LO}}{E}\right)^{1/2} - \frac{1}{2} \left(\frac{\hbar\omega_{LO}}{E}\right)^2 \sinh^{-1} \left(\frac{E}{\hbar\omega_{LO}}\right)^{1/2} \right], \\
B(E) &= \Theta(E - \hbar\omega_{LO}) \left(\frac{E}{\hbar\omega_{LO}}\right)^{3/2} \left[\left(1 - \frac{\hbar\omega_{LO}}{2E}\right) \left(1 - \frac{\hbar\omega_{LO}}{E}\right)^{1/2} - \frac{1}{2} \left(\frac{\hbar\omega_{LO}}{E}\right)^2 \sinh^{-1} \left(\frac{E}{\hbar\omega_{LO}} - 1\right)^{1/2} \right].
\end{aligned}
\tag{2.83}$$

Note, that in Equation 2.82 $n_{LO} A(E)$ is the term referring to phonon absorption, and $(n_{LO} + 1) B(E)$ to stimulated and spontaneous phonon emission, respectively, analogous to Equation 2.58 describing the LO phonon scattering rate.

CHAPTER 3

Materials and Experimental Methods

3.1 Sample Preparation

In the scope of this thesis both, CsPbI₃ NCs and CsPbI₃ NC:PCBM were examined. These were self-made in the in-house chemistry lab. Sample preparation involved the synthesis of CsPbI₃ NCs, followed by admixture of PCBM in case of CsPbI₃ NC:PCBM. In a final step, the obtained solutions were either investigated in solution (in a quartz glass cuvette), or in form of a spin coated film on a sapphire substrate.

3.1.1 Synthesis of CsPbI₃ Nanocubes

Colloidal CsPbI₃ NCs are synthesized from CsPbBr₃ NCs by a post-synthetic anion exchange reaction using PbI₂ as a precursor.^{25,99} First, CsPbBr₃ NCs are synthesized by an ultrasonication approach developed at the chair (Chair for Photonics and Optoelectronics, LMU).²⁵ This method has the great advantage to not require high temperatures, or inert atmospheres as, by contrast, required in the hot-injection approach and other synthesis techniques.^{20,149} During the ultrasonication process direct tip-sonication (SONOPULS HD 3100, BANDELIN, 30W, 10 min) is applied to a mixture of precursor salts (0.1 mmol Cs₂CO₃ and 0.3 mmol PbBr₂) in combination with capping ligands (0.5 ml oleic acid and 0.5 ml oleylamine) in 10 ml of the non-polar solvent octadecene under ambient atmospheric conditions. The transition from an initial colourless solution to a yellow solution during tip-sonication indicates that CsPbBr₃

NCs have formed. The next step is centrifugation (10000 rpm, 10 min) and re-dispersion of the sediment in hexane by mild sonication. Subsequently, this step is repeated in order to finally attain homogeneously sized, well-dispersed CsPbBr₃ nanocubes.

The as prepared CsPbBr₃ NC colloidal solution is now treated post-synthetically to convert to CsPbI₃ NCs. First, a PbI₂-ligand solution is prepared by dissolving 0.2 mmol PbI₂ precursor in a mixture of 50 ml toluene, 2 ml oleylamine, and 2 ml oleic acid at 100 °C under continuous stirring. To initiate the halide exchange reaction, 10 ml of the precursor solution is added to 1 ml of the CsPbBr₃ NC solution and set aside for two hours under continuous stirring at ambient conditions. The halide exchange reaction is completed if the colour has shifted from yellow (CsPbBr₃ NC) to red (CsPbI₃ NC). This can be checked by eye to get a first impression, and by analysing the PL spectrum of this solution. In the next step, the obtained dispersion of colloidal CsPbI₃ NC are purified. For this, the sediment resulting from centrifugation (14500 rpm, 30 min) is re-dispersed in 2 ml hexane. Thus, a concentrated dispersion of homogeneously sized CsPbI₃ NC is obtained, ready to be diluted to a desired concentration and/or spin coated onto glass substrates for optical measurements.

High-angle annular dark-field scanning transmission electron microscopy (HAADF-STEM) allows for precise imaging and structural characterization of nanoparticles. The HAADF-STEM image in Figure 4.1 in Chapter 4 is recorded by an FEI Titan microscope operating at 300 kV and shows the self-made colloidal CsPbI₃ NC resulting from the procedure described above.

3.1.2 Mixing of CsPbI₃ Nanocubes with PCBM

[6,6]-Phenyl C₆₁ butyric acid methyl ester with the formula C₇₂H₁₄O₂ is commonly referred to as PCBM.¹⁵⁰ It is a suitable acceptor material for CB electrons of CsPbI₃, as these two materials form a type II heterojunction.¹⁵¹ To be precise, the lowest unoccupied molecular orbital (LUMO) of PCBM (-4.3 eV^{152}) lies energetically about 750 meV below the CsPbI₃ CB minimum (-3.55 eV^{151}). Meanwhile, VB holes remain in CsPbI₃, because its VB maximum (-5.25 eV^{151}) lies about 750 meV above the highest occupied molecular orbital (HOMO) of PCBM (-6.0 eV^{152}). This is visualized in the energy level diagram in Figure 3.1 a. The energy level diagram suggests that bringing together PCBM and the CsPbI₃ NCs should strongly affect photoexcited CB electrons in CsPbI₃. Namely, they may quickly be scavenged by PCBM and leave the CsPbI₃ NCs. Meanwhile, photoexcited VB holes are expected to remain in CsPbI₃. A blend system of this form, i.e. CsPbBr₃ NC:PCBM, has previously shown efficient electron

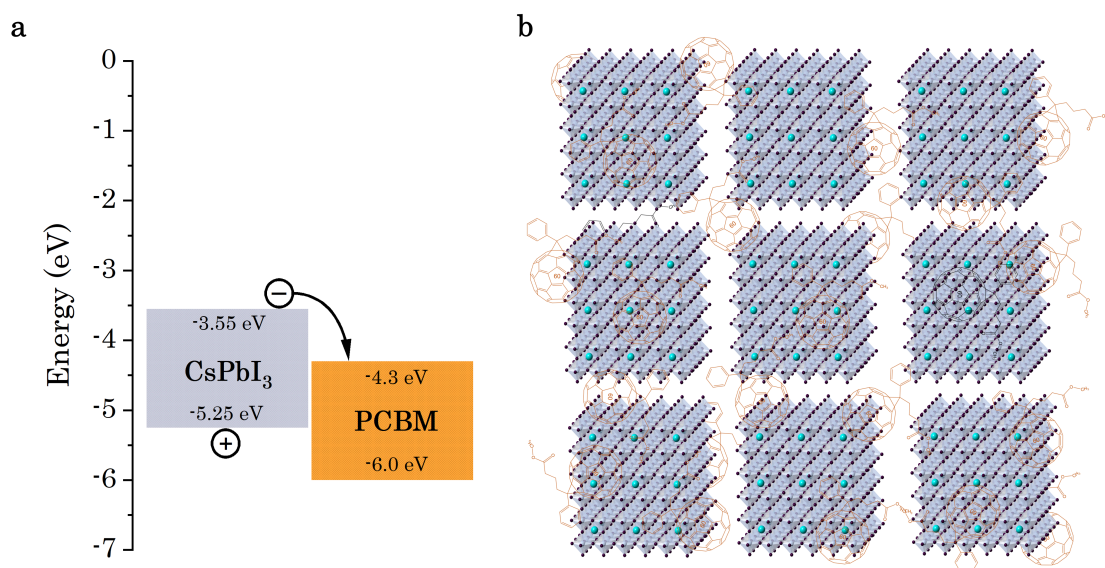


Figure 3.1: Combination of CsPbI₃ and PCBM. (a) Energy level diagram and visualization of the energetically favourable process of a CsPbI₃ CB electron (⊖) transferring onto PCBM. Meanwhile, VB holes (⊕) remain in CsPbI₃ due to the insuperable energetic barrier towards PCBM. (b) Sketch of the CsPbI₃ NC:PCBM blend showing PCBM molecules (orange) lying on top of the NC surfaces. The scaling of NCs and molecules does not reflect their real sizes.

transfer.¹⁵³ Furthermore, it is reported that the electron transfer properties are superior in case of the blend compared a CsPbBr₃ NC:PCBM layer-by-layer structure. It is thus favourable to also use a blend, rather than a layer-by-layer system in the investigation of CsPbI₃ NC:PCBM as was done in the scope of this thesis. Efficient electron transfer from CsPbI₃ to PCBM enables one to not only locally, but also optically separate electrons from holes, because CB electrons, which are located on PCBM are invisible in the CsPbI₃ spectrum. This way, spin relaxation rates of electrons and holes can be analysed individually by fitting the data with respective rate equations (Section 6.2).

For this reason, a blend solution of the colloidal CsPbI₃ NCs and PCBM has been prepared as follows. First, PCBM is dissolved in chlorobenzene with a concentration of 15 mg/ml and stirred at 70 °C for 3-4 hours in order for PCBM to dissolve completely. The obtained PCBM solution is subsequently mixed with the purified colloidal CsPbI₃ NC dispersion (Subsection 3.1.1) in a 1 : 1 volumetric ratio resulting in the desired blend solution. Just like in the case of the pure CsPbI₃ NCs solution, the blend solution may be diluted to a desired concentration and/or spin coated onto glass substrates for optical measurements.

SEM and TEM images of pure and blend solution reveal that their morphologies are much the same. This is a strong indication that PCBM molecules settle on the surface of CsPbI₃ NCs without altering the NC morphology.¹⁵⁴ This is sketched in Figure 3.1 b.

3.2 Linear Optical Spectroscopy

3.2.1 Absorption and Photoluminescence Spectroscopy

In order to record linear absorption and PL spectra of a prepared sample solution, the latter is drop-deposited onto a sapphire substrate and spread into a thin layer through spin coating. The coated substrates, once dry, are measured in a Cary 5000 UV-Vis-NIR spectrophotometer and a Varian Cary Eclipse fluorescence spectrophotometer (Agilent Technologies), respectively, at ambient conditions.

The PL spectra provide information about whether the halide exchange reaction during the above described synthesis of CsPbI₃ NCs is completed. It is the case, if the PL emission has shifted from ≈ 2.39 eV green (CsPbBr₃ NCs) to ≈ 1.85 eV red (CsPbI₃ NCs). Furthermore, the magnitude of PL emission is an indicator of sample degradation, as the photoactive colloidal NCs become photoinactive (no emission) over time (months), which is a consequence of phase transition to the yellow non-perovskite δ -phase.

Regarding absorption spectroscopy, it is important to bear in mind that experimentally, absorption cannot be measured directly, as it is superimposed by other optical processes. Those are outlined in the beginning of Subsection 2.2.1. Instead, absorbance, the total attenuation of transmitted radiant power (\propto intensity I) across the entire material thickness, l , is measured and quantified in terms of optical density (OD) or transmittance (T).

$$\frac{I(z=l)}{I_0} = T = 10^{-OD} = e^{-\alpha l} \quad (3.1)$$

By neglecting any attenuating optical processes other than absorption, Beer's law, given in Equation 2.18, relates α to OD and T . It has been used for the last term in Equation 3.1. Note, that T , OD , α , and $I(z)$ are all material-specific parameters and therefore dependent on radiation frequency (ω).

Measurement data is only of use, if it can be interpreted through theoretical considerations. Therefore, the measured OD data must be related to the imaginary part of the dielectric function, ϵ_i , which was derived to describe absorption from theoretical considerations (c.f. Subsection 2.2.1). Equation 2.19 relates α to ϵ_i . Comparing OD - and α -term in Equation 3.1 reveals that they merely differ by their bases, i.e. base 10 and base e , respectively. OD and α

are therefore proportional.

$$OD = -\log_{10}(e^{-\alpha l}) = \frac{1}{\ln(10)}\alpha l \approx 0.434 \alpha l$$

$$\Rightarrow OD \propto \alpha \quad (3.2)$$

Equation 3.2 is true, as long as any attenuating optical processes other than absorption are neglected. However, acknowledging that all attenuating optical processes contribute to the signal recorded through absorption spectroscopy (“absorbance spectroscopy” would be the more accurate term), the resulting OD data nevertheless allows for an estimation of α . Namely, by approximating all attenuating optical processes other than absorption to be independent of ω . Those are then collectively accounted for by a global offset (OD_{offset}).

$$OD(\omega) + OD_{\text{offset}} = \frac{1}{\ln(10)} \alpha(\omega) l \quad (3.3)$$

Equation 3.2 and Equation 3.3 establish the relation between the measured $OD(\omega) + OD_{\text{offset}}$ data and $\alpha(\omega)$. Combined with Equation 2.19, which relates $\alpha(\omega)$ to $\varepsilon_i(\omega)$, a direct comparison between measurement and theory can be drawn. The respective function for data-fitting is derived in Subsection 2.2.1 and Section A.2, and the result is given by Equation A.10.

3.2.2 Polarization Dependent Spectroscopy

The expression “dichroism” has its origin in the Greek language and means “two-coloured”. It describes polarization dependent absorption, which is a material characteristic exhibited by chiral substances and some crystals.³⁸ To understand this phenomenon, one has to refer to Equation 2.15 and Equation 2.19 in Subsection 2.2.1. These nicely show that the absorption coefficient, $\alpha(\omega)$, directly depends on the imaginary relative refractive index, $n_i(\omega)$. A material exhibits linear dichroism, if its imaginary refractive indices for ordinary and extraordinary crystal axes are dissimilar. Hence, after transmission, white light shows unequal spectra, i.e. appears in different colours, when linearly polarized parallel to the ordinary, or extraordinary crystal axis. “Two-coloredness” is thus an appropriate depiction. Analogously, a material exhibits circular dichroism (CD) if it possesses different imaginary refractive indices for right and left handed circularly polarized light, which again cause wavelength dependent absorption to different extents and result in non-identical transmission spectra. Hence, after transmission of right, or left handed circularly polarized radiation, these rays appear in different colours.

Working Principle of CD Spectroscopy

CD spectroscopy is a form of absorption spectroscopy, which measures the degree of circular dichroism exhibited by a substance. In the scope of this thesis, CD measurements were conducted at the Chirascan Circular Dichroism Spectrometer (Applied Photophysics) at the Chair of Professor Rädler (LMU). The built in light source (xenon arc lamp) emits unpolarized white light with wavelengths covering the UV-Vis spectrum.¹⁵⁵ Subsequently, it enters a monochromator, which automatically scans a user-defined wavelength range once the measurement is started. Linear polarization of the light beam is ensured by transmission through a linear polarizer, e.g. a Glan-Thompson polarizing prism. The linearly polarized, monochromatic light now enters a photo-elastic modulator (PEM), which essentially acts as a dynamic quarter wave plate and modulates the polarization to be alternately left or right handed circularly polarized at a known frequency. Subsequently, the beam is transmitted through the sample, its signal is amplified by a photomultiplier and finally photodetected through an avalanche photodiode. The photodetection signal is interpreted using a lock-in amplifier, which is synchronized to the PEM frequency. By comparing the absorbance of left-handed circularly polarised light (L-CPL) and right-handed circularly polarised light (R-CPL), i.e. $\Delta A \equiv A_{L-CPL}(\lambda) - A_{R-CPL}(\lambda)$, CD spectroscopy gives information about the sample's wavelength dependent degree of circular dichroism.

Working Principle of a Retarder Wave Plate

Dichroism is related to birefringence, where the real instead of the imaginary part of the refractive indices of a material differ for extraordinary and ordinary crystal axes. The real part of the refractive index, $n_r(\omega)$, determines the phase of the transmitted light wave (rightmost term of Equation 2.15). In contrast, the imaginary refractive index, $n_i(\omega)$ determines the absorption coefficient, $\alpha(\omega)$, and thus attenuation, as elaborated in detail in Subsection 2.2.1. During transmission of e.g. linearly polarized light through a birefringent material, a phase difference between the component polarized along ordinary and extraordinary crystal axis accumulates. This phenomena is known as retardation.³⁸ The magnitude of retardation is determined by the phase difference, i.e. $\Delta\phi = \frac{2\pi|\Delta n(\omega)|d}{\lambda}$, with $\Delta n(\omega) = n_o(\omega) - n_e(\omega)$ (all real) and λ the vacuum wavelength of the incident light. Consequently, linearly polarized radiation can be transformed into elliptical or circular polarization and vice versa upon transmission through a birefringent material. The working principle of a wave plate, also known as a retarder, is based on this effect.¹⁵⁶ If linearly polarized radiation has an angle of 45 degree to

the ordinary crystal axis of the wave plate and the thickness of the wave plate is such that $|\Delta\phi| = \frac{\pi}{2} = \frac{\lambda}{4}$, the radiation polarization is transformed from linear to circular and the wave plate is referred to as a quarter wave plate.³⁸

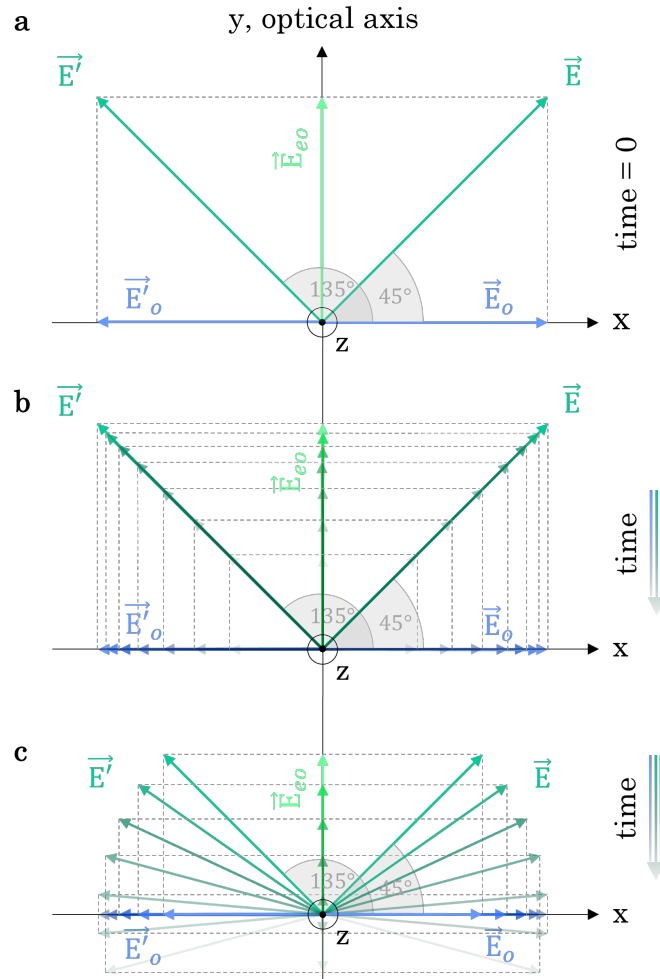


Figure 3.2: Effect of a quarter wave plate on the electric field vector of EM radiation. (a) Two electric field vectors incident on a quarter wave plate, \vec{E} enclosing 45° and \vec{E}' enclosing 135° with the x-axis. As defined by the quarter wave plates used in the experiments presented in this thesis, the y-axis is the optical axis, which is in this case the slow axis, and the x-axis is the fast axis. The propagation direction of the EM wave is along the z-axis, i.e. out of the paper plane, towards the reader. **(b)** The depicted temporal evolution of \vec{E} and \vec{E}' illustrates two individual linearly polarized EM waves. This is the situation before the rays enter the quarter wave plate. **(c)** Temporal evolution of \vec{E} and \vec{E}' after completed transmission through the quarter wave plate. \vec{E} now rotates clockwise, while \vec{E}' rotates counter-clockwise. Hence, the EM radiation polarization is now right-handed circular and left-handed circular, respectively.

For polarization dependent experiments conducted in the scope of this thesis the following quarter wave plates were used: Thorlabs AQWP05M-600 (400 – 800 nm) and Thorlabs SAQWP05M-700 (325 – 1100 nm).¹⁵⁶ Both are composed of crystalline Quartz (at $\hbar\omega = 1.92$ eV: $n_o = 1.542, n_{eo} = 1.551$)^{157,158} and Magnesium Fluoride (at $\hbar\omega = 1.92$ eV: $n_o = 1.377, n_{eo} = 1.389$)^{159,160}. These materials both exhibit $n_o < n_{eo}$ at the given radiation energy. As a conse-

quence, according to Equation 2.16, travel velocities inside the quarter wave plate are $v_o > v_{ao}$. The ordinary axis (here x-axis) is therefore the so called “fast axis” and the extraordinary axis (here y-axis) the “slow axis”. As the frequency of the EM wave, i.e. the oscillation frequency of the electric field vector, is constant for all refractive indices, once fully transmitted through the wave plate, its phases are $\phi_o < \phi_{ao}$, i.e. $|\Delta\phi| = \frac{\lambda}{4}$ in case of a quarter wave plate. Consequently, if the electric field vector was polarized linearly before entering the wave plate, it is circularly polarized after transmission. This is illustrated in Figure 3.2.

Working Principle of a Glan-Thompson Polarizing Prism

A Glan-Thompson polarizing prism is another example of an application making use of birefringence. It consists of two calcite prisms connected at their interfaces through optical cement. The angle θ of the prisms are chosen such that the ordinary components of the unpolarized input light ray experiences total internal reflection at the prism interface, while the extraordinary components pass through both prisms. This creates a linearly polarized output ray of high quality from an unpolarized input ray.

3.3 Differential Transmission Spectroscopy

DTS is a pump-probe technique allowing for time-resolved identification of occupied and unoccupied VB and CB states. It is based on the principle of Pauli exclusion, also referred to as Pauli blocking, which refers to the quantum mechanical principle that two fermions cannot occupy the same state. In other words, linear optical excitation is not possible if the respective VB or CB state is already occupied by an electron or a hole, respectively.

The working principle of DTS becomes clear when taking a detailed look into the measurement sequence. First, a pump pulse with user-defined power and wavelength is targeted onto the sample under investigation. Within the sample material, optical transitions may be induced, causing the filling of the respective phase space. Second, at variable time delay with respect to the pump pulse, a spectrally broad probe pulse arrives at the identical sample area that was previously illuminated by the pump pulse. The probe pulse of the DTS setup used in the scope of this thesis covers the entire visible spectrum and appears as white light (WL). It is therefore also referred to as WL pulse. Depending on the wavelength, i.e. energy, of an exemplary probe pulse photon, two situations exist: If its energy coincides with a transition into a state, which is already occupied through absorption of pump pulse photons, it is transmitted or

even accompanied by a coherent photon of identical energy, which is created in the process of stimulated emission (e). Else, the exemplary photon may be absorbed by the sample. Note, that at high laser powers additional cases must be taken into account as non-linear optical phenomena, such as second- or third order harmonic generation, gain importance.³⁸ The experiments presented in this thesis were conducted at low laser powers. This justifies to interpret phase space filling and stimulated emission to be the dominant phenomena leading to the recorded DTS signals evaluated and discussed in Chapter 5 and Chapter 6.

The fraction of the WL pulse, which is transmitted through the sample is dispersed into its spectral components through a spectrometer. This spectrum is compared to a spectrum recorded in the second part of the DTS measurement sequence: The pump pulse is blocked and is thus inhibited to optically interact with the sample. Therefore, solely the probe pulse arrives at the sample and may induce material specific optical transitions. The complete experimental sequence of DTS can therefore be expressed in the following condensed manner: [Pump, delay t_1 , Probe], denoted as P,WL, followed by [Probe], denoted as WL. Subsequently, this sequence is repeated at changed time delay, i.e. [Pump, delay t_2 , Probe] (P,WL), followed by [Probe] (WL). And so on. This sequence is depicted in Figure 3.3.

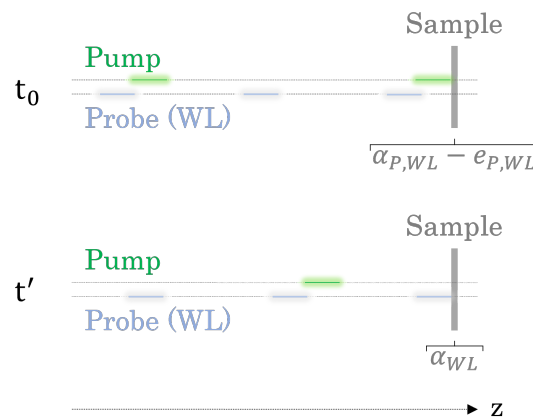


Figure 3.3: Laser pulse sequence in DTS. At time t_0 , a pump and probe pulse reach the sample (at a user defined, variable time delay between them). At time $t' > t_0$, only a probe pulse reaches the sample. Subsequently, the pulse sequence repeats at t_0 and so forth. Note, that pulse length (100 fs) and the intermediate interval between two probe pulses (1 ms) are drawn disproportionate, as they differ by the order of 10^{10} . Also note, that in DTS, pump and probe pulses spatially overlap on the sample. This is omitted here for the purpose of clarity. Therefore, exclusively the z-axis, the propagation direction of the laser pulses, is included.

Hence, in DTS, a sample's change in optical density (OD) is measured, which is induced by the pump pulse. Through the use of Equation 3.1, this change in OD, ΔOD , can be expressed as

$$\begin{aligned}\Delta OD &= OD_{P,WL} - OD_{WL} \\ \Rightarrow \Delta OD &= -\log_{10}\left(\frac{I_{P,WL}}{I_0}\right) + \log_{10}\left(\frac{I_{WL}}{I_0}\right) = -\log_{10}\left(\frac{\frac{I_{P,WL}}{I_0}}{\frac{I_{WL}}{I_0}}\right) = -\log_{10}\left(\frac{I_{P,WL}}{I_{WL}}\right).\end{aligned}\quad (3.4)$$

The proportionality between OD and α (Equation 3.2) also holds for ΔOD and $\Delta\alpha$. Hence,

$$\begin{aligned}\Delta OD &= -\log_{10}\left(\frac{\frac{I_{P,WL}}{I_0}}{\frac{I_{WL}}{I_0}}\right) = -\log_{10}\left(\frac{e^{-(\alpha_{P,WL}-e_{P,WL})l}}{e^{-\alpha_{WL}l}}\right) = -\log_{10}\left(e^{-(\alpha_{P,WL}-e_{P,WL}-\alpha_{WL})l}\right) \\ \Rightarrow \Delta OD &= \frac{1}{\ln(10)} \Delta\alpha l,\end{aligned}\quad (3.5)$$

where it is assumed that exclusively phase space filling and stimulated emission are responsible for the change in absorption coefficient $\Delta\alpha$ (as was pointed out above), i.e.

$$\begin{aligned}\Delta\alpha &= [\alpha_{P,WL} - e_{P,WL}] - \alpha_{WL} \\ \Rightarrow \Delta\alpha &= [(1 - f_e)(1 - f_h) \alpha_{WL} - f_e f_h \alpha_{WL}] - \alpha_{WL} = -(f_e + f_h) \alpha_{WL}.\end{aligned}\quad (3.6)$$

f_e and f_h are the photoexcited electron and hole distribution functions, respectively. Hence, the pump pulse-induced change in the sample's absorption coefficient, $\Delta\alpha$, discloses information about electron and hole occupancies in the CB and VB, respectively, as manifested in Equation 3.6. $\alpha_{P,WL}$ and α_{WL} denote the absorption coefficients resulting from probe pulse arrival at the sample with and without prior pumping, respectively, and are shown in Figure 3.3 (gray description below sample). This sketch, thus, also visualizes the chosen Ansatz in Equation 3.6 top.

It is customary to express experimental pump-probe data in terms of differential transmission, $\frac{\Delta T}{T}$, which is related to the measured laser intensities through

$$\frac{\Delta T}{T} = \frac{\frac{I_{P,WL}-I_{WL}}{I_0}}{\frac{I_{WL}}{I_0}} = \frac{I_{P,WL} - I_{WL}}{I_{WL}} = \frac{I_{P,WL}}{I_{WL}} - 1.\quad (3.7)$$

Here, it was used that $\Delta T = T_{P,WL} - T_{WL} = \frac{I_{P,WL}-I_{WL}}{I_0}$, according to Equation 3.1.

By combining Equation 3.4, Equation 3.5, Equation 3.6 and Equation 3.7, a relation between $\frac{\Delta T}{T}$, ΔOD and $\Delta\alpha$ is obtained.

$$\frac{\Delta T}{T} = 10^{-\Delta OD} - 1 = e^{-\Delta\alpha l} - 1 \stackrel{Taylor}{=} (1 - \Delta\alpha l + \mathcal{O}((\Delta\alpha l)^2)) - 1 \approx (f_e + f_h)\alpha_{WL}l \quad (3.8)$$

This manifests that time-resolved pump-probe spectroscopy is a distinct information source of temporal state occupancies of CB electrons and VB holes.

The DTS Setup

Coherent, monochromatic light is provided to the DTS setup by the Libra-HE+ laser system by Coherent. It is an ultrafast Titanium:Sapphire based amplifier system, which outputs 800 nm laser pulses of 100 fs pulse length at a repetition rate of 1 kHz. The inconceivable short duration of the pulse length can be made somewhat more graspable by comparing the following ratios: $\frac{1s}{100 fs} \approx \frac{300\,000\,years}{1s}$. Femtosecond laser pulses allow for cutting-edge experiments at the forefront of current research, as the pulse length defines the temporal resolution of the experiment.

The output power of the Libra-HE+ laser system is $\approx 5 W$, which, at first glance, appears like a dim light bulb. However, considering that only every one millisecond a pulse emerges, which is as short as 100 fs, the output power of $\approx 5 W$ is quite a lot and amounts to 50 GW during one pulse. A large laser power is important for pump-probe experiments, as the laser beam has to be divided into a pump and probe beam, both requiring sufficient power to provoke second harmonic processes and account for losses at various optical components, such as mirrors, lenses, irises and so forth, on its way to the sample. Moreover, pump and probe beam must emerge from the same laser source, as their pulses need to be temporally correlated. Only then, pump and probe pulses can be simultaneously incident at the sample and the probe pulse precisely delayed with respect to the pump pulse. This time delay is achieved through a delay stage, enlarging the beam path of the probe beam, which correlates to a prolongation in propagation of up to 3 ns. (The incremental step size of the delay stage is 100-fold smaller than the resolution of the experiment, which is determined by the pulse length.)

After passing the delay stage, the 800 nm probe beam is focussed into a CaF₂ crystal, thereby activating internal non-linear optical processes enabling white light generation. Subsequently, this spectrally broad probe beam is focussed through the use of a parabolic mirror onto the sample and its transmission is detected by a spectrometer.

Simultaneously, wavelength, focus and direction of the pump beam is prepared before locally coinciding with the probe beam at the sample position. Thereby, the journey of the pump beam differs quite substantially from that of the probe beam. The 800 nm output from the Libra-HE+ laser system is split by a beam splitter, designating one part of it as the pump beam. It passes an optical parametric amplifier (OPA), which is a complex system comprised from diverse optical components, again involving multiple non-linear optical processes. It offers continuous wavelength tuning from $\approx 300\text{ nm} - 11000\text{ nm}$. This is crucial to experiments, which rely on resonant pumping, i.e. of the same energy as transitions at the optical band gap of the sample material. Most experiments presented in this thesis were conducted at precise resonant pumping energy. Because only every second pump pulse must arrive at the sample in order to produce a differential signal (c.f. Figure 3.3), a chopper, operating at 500 kHz , i.e. half of the 1 kHz laser repetition rate, is located in the pump beam path. Finally, a neutral density (ND) filter wheel allows to attenuate its power as desired by the user. At the position of the sample, the diameter of the pump beam is measured to be $d_{\text{pump}} = 1.05\text{ mm}$. Thus, an area on the sample of $A = (d_{\text{pump}}/2)^2 \pi = 8.66 \cdot 10^{-3}\text{ cm}^2$ is illuminated.

Finally, a MS260i spectrometer by Newport receives the probe pulses after transmission through the sample. The recorded spectra from probe pulses with and without prior pumping allows for the computation of a DT signal, which is visualized by Newport software on a computer. Ultimately, time-resolution of the DT spectra becomes possible through the combined analysis of delay stage position and the respective transmission spectrum.

The described DTS setup only allows for unpolarized measurements. During my time as a PhD student, I modified the setup for the purpose of conducting polarization dependent DTS. This included the selection and order of suiting components and their installation, alignment, testing and use.

Thereby, the pump beam path was equipped with an achromatic quarter wave plate, converting linear into circular polarization for wavelengths within $400 - 800\text{ nm}$ (Thorlabs AQWP05M-600). In the probe beam path, a Glan-Thompson polarizing prism (GT), which ensures broad band linearly polarized radiation, was installed after the CaF_2 WL crystal. The reason for this is, that the initially linearly polarized output from the Libra-HE+ laser system becomes rather unpolarized during the WL generation process. In order to generate circularly polarized radiation through the use of a quarter wave plate, however, the incident radiation must be linearly polarized (c.f. Figure 3.2). After the GT, a superachromatic quarter waveplate (Thorlabs

SAQWP05M-700) was installed to ensure broad band (325-1100 nm) circular polarization of the WL probe pulse.

As described in Subsection 3.2.2, circular polarization is achieved at an angle of 45° between the fast axis of a quarter-wave plate and the linear polarization of the entering beam. Consequently, left-handed circular polarization (σ^+) can be inverted into right-handed circular polarization (σ^-), and vice versa, through a 90° rotation of the quarter wave plate.

The implementation of the described alterations of the DTS setup now allow for polarization sensitive experiments. A sketch, showing the most relevant optical components, is displayed in Figure 3.4. It is this setup, that I used to conduct the majority of measurements presented in this thesis.

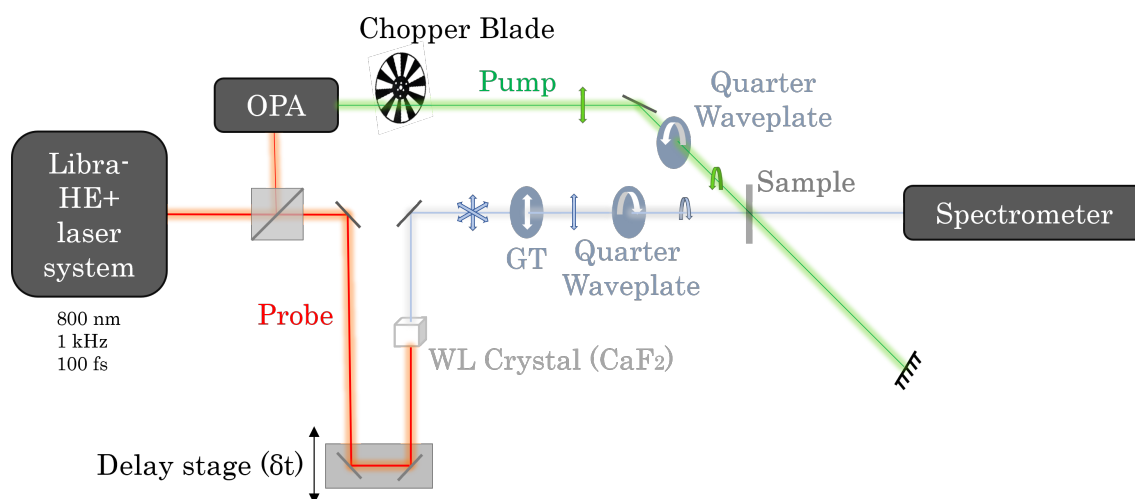


Figure 3.4: DTS setup including alterations allowing for polarization dependent experiments. The shown optical components are described in the text. Green and blue arrows pointing in random (unpolarized), up-down (linear polarization) and circular (circular polarization) direction indicate the polarization of pump and probe pulses, respectively.

CHAPTER 4

Optical Characterization of CsPbI₃ Nanocubes

Before presenting their optical characterization, first I want to show an HAADF-STEM image of the CsPbI₃ nanocubes produced and investigated in the scope of this thesis (Figure 4.1).

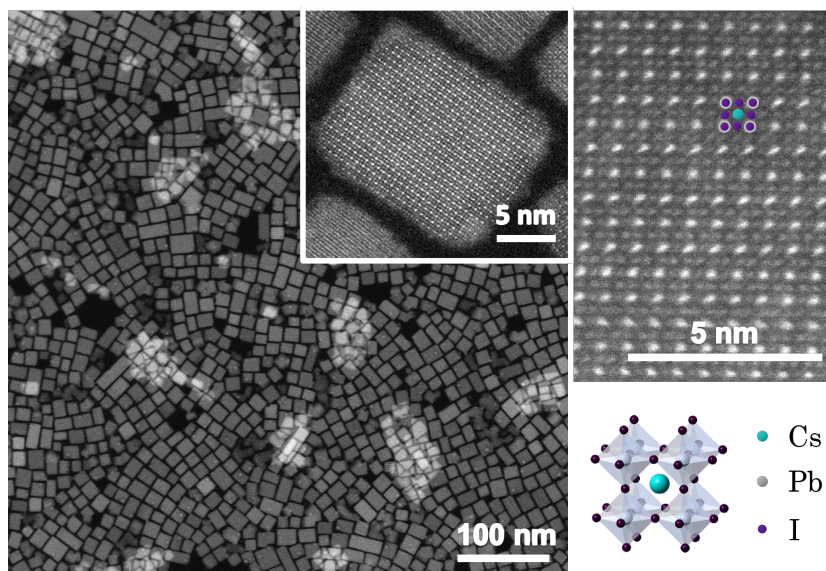


Figure 4.1: HAADF-STEM images of the CsPbI₃ NCs prepared and investigated in the scope of this thesis. Individual atoms are accentuated in the top right image with the colour code matching that of the illustrated crystal structure.

The HAADF-STEM image reveals the NC's cubic morphology and single-crystalline nature. Individual atoms, which build the crystal lattice, are accentuated in the magnified picture

(top right).²⁵ Edge lengths of the nanocubes are evaluated from the image and result on average in $L = 13 \pm 3 \text{ nm}$. This length exceeds the reported exciton Bohr radius in CsPbI₃ NCs of $a_X = 3.3 \text{ nm}$,⁷² classifying these particles to fall under the weak confinement regime (c.f. Subsection 2.1.1). Size quantization is therefore expected to be insignificant in these CsPbI₃ NCs. This is addressed and confirmed via precise spectroscopic analysis presented in the next section.

4.1 Static Absorption and Photoluminescence Spectra

Figure 4.2 shows RT measurements of static absorption and PL spectra of CsPbI₃ NCs deposited on a glass substrate. Under UV illumination, the CsPbI₃ NCs exhibit red PL with a maximum photon energy of 1.85 eV . In the absorption data, a steep continuum absorption onset is present, which is overlaid by its fit function in the inset. The fit function was generated using Equation A.10. One of the fitting parameters is the band gap energy, which results in $E_g = 1.8572 \pm 0.0008 \text{ eV}$ for the shown fit function. The value just about coincides with the PL peak energy, indicating that radiatively recombining charge carriers originate primarily from the band gap. Both, absorption and PL spectra are in accordance with previous reports.^{20,25,72,82}

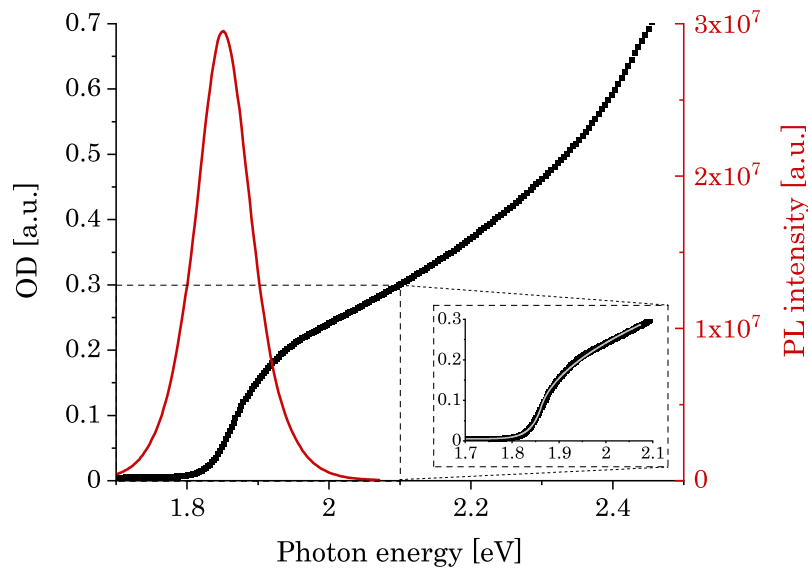


Figure 4.2: Static absorption and PL spectra of CsPbI₃ NCs. Measured data points of OD (black) and PL intensity (red) correspond to left and right y-axis, respectively. The inset shows the OD data for energies around the band gap overlaid by a fitting curve (gray).

Significant excitonic features are absent in the absorption spectrum, indicating that homogeneous broadening due to thermally induced exciton dissociation, i.e. LO phonon scattering, exceeds the exciton binding energy. Explicitly, $R_{YX} = 23.3 \text{ meV} < E_{th} = 37.9 \text{ meV}$. The value for R_{YX} is extracted from my experimental data as described below and is consistent with previous reports on CsPbI₃ NCs (21.2 meV^{72} , 20 meV^{20}). Therefore, it can be inferred that e-h pairs are mostly ionized yielding free charge carriers rather than excitons. Another evidence of this is that the evaluated average NC edge length L (Subsection 3.1.1) exceeds the exciton Bohr radius, $a_X = 3.3 \text{ nm}^{72}$. Thus, the NCs can be classified to lie in the weak confinement regime (c.f. Subsection 2.1.1) and therefore exhibit bulk-like optical properties. This is in line with the shape of the measured continuum absorption onset in Figure 4.2.

Figure 4.3 shows absorption spectra of CsPbI₃ NCs measured from cryogenic temperatures, 4 K, to RT, 293 K. With decreasing temperature, a bulge becomes increasingly identifiable as it grows into an independent peak and shifts away from the continuum towards smaller photon energies. It is interpreted as the 1s resonance of excitonic absorption. Increased excitonic contribution at cryogenic temperatures has been reported for various LHPs.^{80,83,86,114}

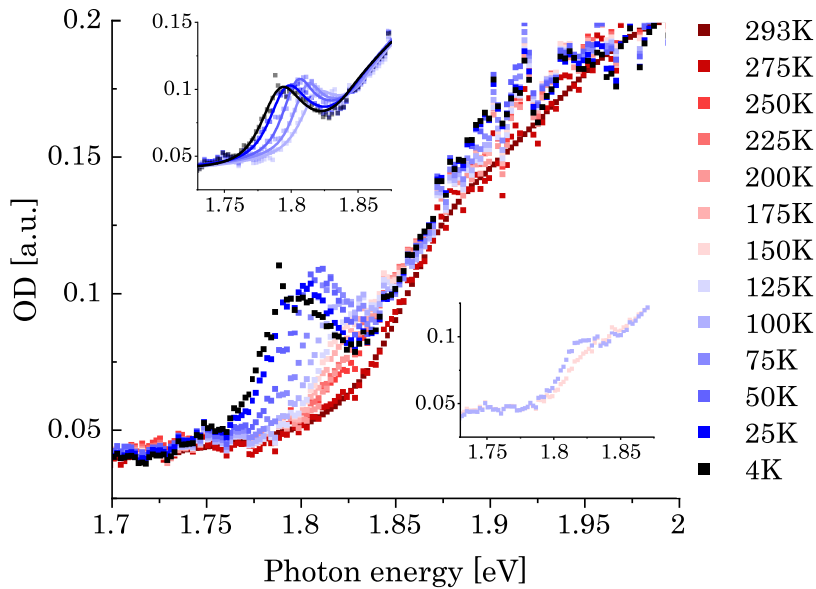


Figure 4.3: Temperature dependent static absorption spectra of CsPbI₃ NCs. OD is recorded for a wide range of temperatures, from 4 K (dark blue), to RT, 293 K (red). In the bottom right inset the 100 K and 150 K spectra are compared to witness the emergence of the 1s excitonic resonance peak. The top left inset shows fitted spectra for the temperature range from 4 K to 100 K using Equation A.10.

In order to extract the exciton Rydberg, spectra from 4 K to 100 K are fitted with Equation A.10. This is shown in the top left inset in Figure 4.3. The best fit to the data is obtained for

$R_{yX} = 23.3 \text{ meV}$. This is a reasonable result as it only slightly exceeds the values given in the literature, which are in the range of $16.3 \text{ meV} - 21.2 \text{ meV}$.^{20,72,75}

The increasing conspicuity of the 1s exciton peak towards lower temperatures clearly supports that bound e-h pairs, i.e. excitons, gain an increasing dominance over free e-h pairs at these temperatures. Explicitly, stable excitons may form at cryogenic temperatures, if $E_{th} < R_{yX}$. Based on the exciton Rydberg extracted from the presented absorption data and the range of literature values, this condition is fulfilled for $T < 180 \text{ K}$ and $T < 126 \text{ K} - 164 \text{ K}$, respectively. In line with this upper temperature bound predicting stable exciton formation, the data presented in Figure 4.3 shows the emergence of an exciton resonance from the steep continuum absorption onset for temperatures $T < 150 \text{ K}$. This is visually well resolved by comparing the 100 K- with the 150 K-spectra in the bottom right inset of Figure 4.3. While the 100 K spectrum (bright blue) clearly allows the assignment of a bulge-like feature, no bulge is observable in the 150 K absorption spectrum (bright rose). Towards higher temperatures excitonic features have fully disappeared, affirming that the probability of thermally induced exciton dissociation increases, resulting in a plasma of free but Coulomb-correlated e-h pairs, rather than excitons.⁸² These give rise to continuum band to band transitions,⁸⁹ as elaborated above in the context of Figure 4.2.

4.2 Circularly Polarized Optical Spectra

From their achiral constituents and symmetric crystal structure, CsPbI₃ NCs are not expected to exhibit chirality. As this work is concerned with spin phenomena in these NCs, it is nevertheless important to exclude intrinsic chirality. Therefore, the CsPbI₃ NCs used in the scope of this thesis (dispersed in solution (hexane)) were examined via CD spectroscopy. The recorded CD spectrum is shown in Figure 4.4. It reveals a signal comparable to the baseline, confirming the achiral nature of these CsPbI₃ NCs. To exclude that the measurement was faulty, a knowingly chiral sample was measured with the same device settings, showing a strong chiral signal at the same y-scale.

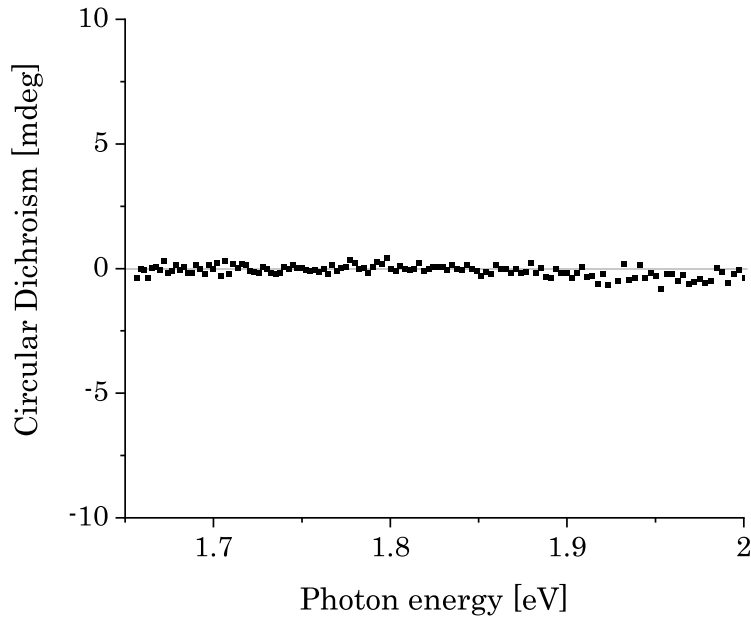


Figure 4.4: CD spectrum of CsPbI₃ NCs. The recorded data points (black dots) lie on the baseline (gray zero-line) for the shown spectral range. This indicates that the examined CsPbI₃ NCs are achiral by nature and do not exhibit any intrinsic CD.

4.3 Recombination Dynamics

Charge carrier recombination dynamics in CsPbI₃ NCs are examined by DTS. Figure 4.5 shows the DTS signal decay over a time delay as long as 1000 ps. Both signals, resulting from a different combination of pump and probe polarizations ($\sigma^+\sigma^+$ and $\sigma^+\sigma^-$) decay synchronous. Only at small delay time the signals are markedly different. This reveals, that consequences due to different polarizations are only significant within the first few picoseconds, but are absent for longer delay times. Charge carrier recombination is thus attested to be considerably slower than spin relaxation. In numbers, $k_{rec} = 0.0041 \text{ ps}^{-1}$ is two orders of magnitude smaller than the spin relaxation rate at RT, which will be elaborated in Section 5.1. k_{rec} is an extracted fitting parameter from the fit function (black curve in Figure 4.5) after its normalization. The decay dynamic based on charge carrier recombination is consistent with previous reports on LHPs.^{70,161}

Moreover, it is important to note that the charge carrier recombination dynamics in Figure 4.5 are of bimolecular nature. There are two indications of this: one, the decay follows Equation 4.2, which describes bimolecular recombination and will be introduced just below. And two, the recombination is non-exponential as is particularly obvious on the logarithmic y-scale in the

inset, which reveals a non-linear decay, rather than a linear one, where the latter would be expected if the recombination was monomolecular. Both indicates bimolecular recombination of free electrons and holes, rather than monomolecular recombination of excitons (exponential decay).^{70,161} It, i.e. if the recombining species were excitons.

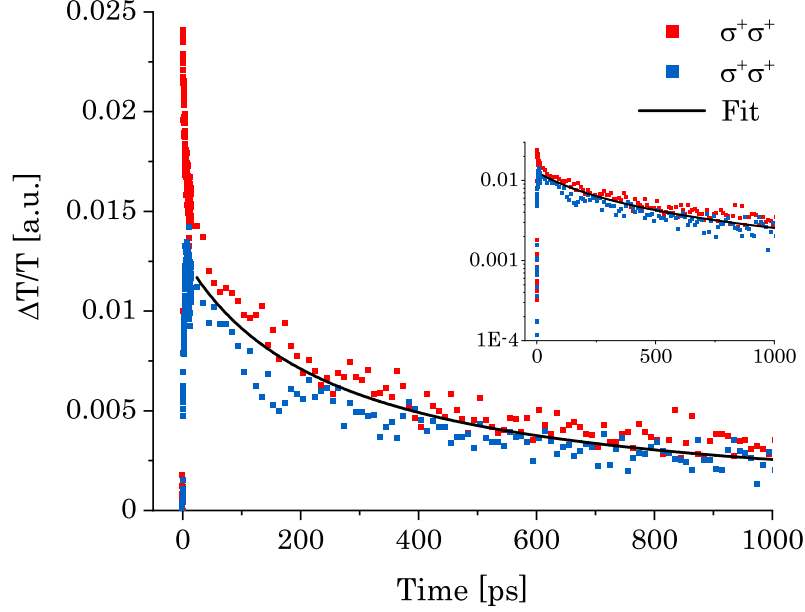


Figure 4.5: Charge carrier recombination dynamics in CsPbI₃ NCs at RT. DT transients reveal the temporal evolution of occupied VB/CB states. The data is fitted with Equation 4.2. In the inset, the equivalent graph is plotted on a logarithmic y-axis, uncovering that the decay is non-exponential.

Bimolecular recombination is derived from the following rate equations

$$\begin{aligned}
 \text{holes: } \dot{N}_{VB}(t) &= -k_{rec} N_{VB}(t) N_{CB}(t) \\
 \text{electrons: } \dot{N}_{CB}(t) &= -k_{rec} N_{VB}(t) N_{CB}(t) \\
 \Rightarrow \dot{N}(t) &= -k_{rec} N^2(t), \quad \text{where } N_{VB} = N_{CB} \equiv N.
 \end{aligned} \tag{4.1}$$

During photoexcitation, an equal number of CB electrons and VB holes are generated, justifying the last line in Equation 4.1. The solution to this rate equation is

$$N(t) = \frac{1}{1/N_{balance} + k_{rec}t}, \tag{4.2}$$

whereupon the fit is created in Figure 4.5. The fitting parameter $N_{balance} \equiv N(t=0)$ defines the starting magnitude from where on $N(t)$ reduces as t increases and converges zero due to charge carrier recombination.

CHAPTER 5

Spin Relaxation in CsPbI₃ Nanocubes

Spin-dependent charge carrier dynamics in CsPbI₃ NCs were investigated through polarization dependent DTS. As described in Section 3.3, circular polarizations of pump and probe rays can be individually regulated in the DTS setup. While the pump is kept σ^+ polarized for all experiments conducted in the scope of this thesis, the probe, which follows the pump excitation at a variable time delay, is either co- (σ^+) or counter-polarized (σ^-) with respect to the pump pulse polarization. With the inversion of circular probe polarization being the only parameter changed between otherwise equivalent experiments, their comparison allows to draw conclusions about optical orientation in CsPbI₃ and intrinsic spin dynamics. This procedure represents the heart of polarization dependent DTS as used here.

The pump pulse excitation density of $5.8 \mu\text{J}/\text{cm}^2$ undercuts the optical gain condition, i.e. population inversion, and thus amplified stimulated emission (ASE) is avoided.^{162,163} At such low excitation density also other unwanted non-linear optical effects are strongly suppressed and therefore disregarded during DTS data interpretation (c.f. Section 3.3).

5.1 Spin Relaxation Dynamics of Free Charge Carriers

Spectra and transients recorded at RT via polarization dependent DTS are displayed in Figure 5.1 a and b, respectively. The spectra are shown at 1 ps delay time. Both, $(\Delta T/T)^{\sigma^+\sigma^+}$ (red) and $(\Delta T/T)^{\sigma^+\sigma^-}$ (blue) spectra exhibit a dominant positive feature peaking at 1.89 eV. This feature is commonly referred to as ground state bleach (GSB). It results from phase space

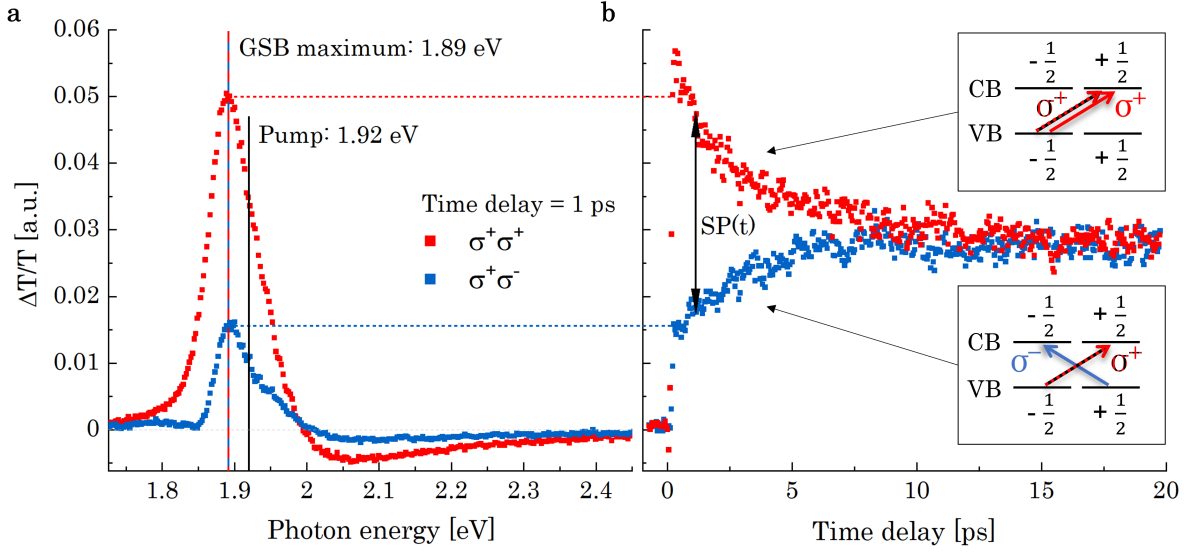


Figure 5.1: Polarization dependent DT spectra and corresponding transients of CsPbI₃ NCs at RT. Pump pulse excitation only slightly exceeds the GSB maximum in energy and can thus be regarded as quasi-resonant. Measurement data recorded with co-polarized pump and probe pulses ($\sigma^+\sigma^+$) is displayed as red squares, while that recorded with counter-polarized pump and probe pulses ($\sigma^+\sigma^-$) is shown as blue squares. The corresponding induced optical interband transitions are represented in the upper and lower inset in (b). (a) DT spectra at 1 ps delay time. (b) Temporal evolution of both GSB magnitudes. The spacing between red and blue curve is denoted as time-dependent spin polarization SP(t).

filling (i.e. Pauli blocking) and stimulated emission at the band gap as discussed in Section 3.3 and justifies Equation 3.6. The pump energy is 1.92 eV and indicated by a vertical black line, visualizing that it is only slightly exceeding the energy of the GSB maximum and therefore nearly resonant with it.

At the low-energy side of the GSB the $(\Delta T/T)^{\sigma^+\sigma^-}$ spectrum shows a little dip at ≈ 1.85 eV. In fact, the time trace at this energy (not shown here) reveals a hesitation for the first ≈ 2 ps before the spectrum rises into a symmetric GSB feature. This is in contrast to the $(\Delta T/T)^{\sigma^+\sigma^+}$ spectrum, which instantaneously rises at the low-energy side of the GSB. The spectrally broad features at the high-energy side of the GSB (negative $\Delta T/T$) manifest photoinduced absorption. These are present for both, $(\Delta T/T)^{\sigma^+\sigma^+}$ and $(\Delta T/T)^{\sigma^+\sigma^-}$. Both features, those at the low- and high-energy side of the GSB, are not subject of investigation here, as the focus is put on those phenomena causing the dominant GSB. However, for the sake of curiosity, I will briefly outline interpretations of the said features based on literature in a bit.

The striking difference between the magnitudes of $(\Delta T/T)^{\sigma^+\sigma^+}$ and $(\Delta T/T)^{\sigma^+\sigma^-}$ at the GSB maximum indicates that significant circular dichroism has been photoinduced into the CsPbI₃ NCs by the σ^+ polarized pump pulse. The corresponding DT transients in Figure 5.1 b show the temporal evolution of the respective GSB magnitude. During an initial step

slope within the first 0.3 ps, $(\Delta T/T)^{\sigma^+\sigma^+}$ rises vastly more than $(\Delta T/T)^{\sigma^+\sigma^-}$, consistent with the massively different GSB magnitudes in Figure 5.1 a. At this instant in time a maximum spin polarization of $SP_{max} \approx 0.043 a.u.$ is reached, where I define spin polarization as $SP \equiv (\Delta T/T)^{\sigma^+\sigma^+} - (\Delta T/T)^{\sigma^+\sigma^-}$. From then on it decreases, because $(\Delta T/T)^{\sigma^+\sigma^+}$ and $(\Delta T/T)^{\sigma^+\sigma^-}$ behave inversely, i.e. the former (latter) exponentially decreases (increases) until both have fully merged at ≈ 10 ps. Hence, the intrinsically achiral CsPbI₃ NCs show CD at the band gap after photoexcitation through the σ^+ pump pulse, which is retained for as long as $SP \neq 0$, that is until $(\Delta T/T)^{\sigma^+\sigma^+}$ and $(\Delta T/T)^{\sigma^+\sigma^-}$ have merged. Note, that pumping with σ^- polarization would equally result in photoinduced CD at the band gap. I have experimentally verified, that the $(\Delta T/T)^{\sigma^-\sigma^-}$ ($(\Delta T/T)^{\sigma^-\sigma^+}$) signal is essentially indistinguishable from the displayed $(\Delta T/T)^{\sigma^+\sigma^+}$ ($(\Delta T/T)^{\sigma^-\sigma^+}$) curve. This is a consequence of the CsPbI₃ NC's intrinsic achirality, which is responsible for their indifference towards circular polarization handedness (c.f. Figure 4.4).

Despite not subject of investigation in this work, I want to briefly comment on what causes the features at the low- and high-energy side of the GSB. The former hesitates to rise into a symmetric GSB feature for the first ≈ 2 ps. This hesitation is possibly caused by the formation of short lived, i.e. rapidly ionized, bi-excitons, lying energetically within the band gap, i.e. below the CB by the amount of their attractive binding energy.¹⁴⁰ Bonding bi-excitons can only be present for the case $\sigma + \sigma^-$, as all four band gap states are occupied (c.f. Figure 5.3), allowing for the formation of a bound pair of excitons, containing two electrons with opposing spins and two holes with opposing spins. This is not possible in the $\sigma + \sigma^+$ measurement as all electrons (holes) have the same spin.

The photoinduced absorption at the high-energy side of the GSB may be predominantly caused by the Moss-Burstein effect.¹⁶⁴ It causes a blue-shift of the band gap due to charge carriers occupying the VB and CB edges. This causes the band gap to blue-shift and gives rise to the observed negative DT signals at the high energy side of the GSB.

The origin of both, high- and low-energy features, is, however, currently still under debate.²⁷

So far, the spectra and corresponding GSB transients in Figure 5.1 are visually analysed and described above. From here on, they shall be quantitatively evaluated and interpreted at the GSB maximum.

Intrinsically, at the CsPbI₃ band gap, σ^+ (σ^-) polarized excitation promotes an electron from $|\frac{1}{2}, -\frac{1}{2}\rangle_{VB}$ ($|\frac{1}{2}, +\frac{1}{2}\rangle_{VB}$) into $|\frac{1}{2}, +\frac{1}{2}\rangle_{CB}$ ($|\frac{1}{2}, -\frac{1}{2}\rangle_{CB}$), as required by the conservation of angular momentum during photon absorption (c.f. Subsection 2.2.3). Thus, upon σ^+ -excitation through

the pump pulse, $|\frac{1}{2}, -\frac{1}{2}\rangle_{VB}$ states are occupied by holes, and simultaneously $|\frac{1}{2}, +\frac{1}{2}\rangle_{CB}$ states are occupied by electrons. This is visualized in Figure 5.2.

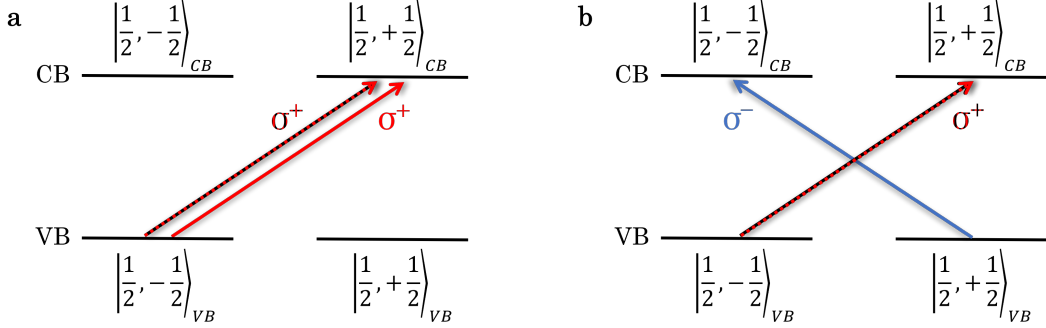


Figure 5.2: Photoinduced optical transitions at the LHP band gap in polarization dependent DTS. To begin with, the semiconductor is optically oriented by a σ^+ polarized pump pulse (red-black dotted). The WL probe pulses are either σ^+ (red), or σ^- (blue) polarized and target optical transitions between the same or the degenerate energy bands. (a) Pump and probe pulses are co-polarized. (b) Pump and probe pulses are counter-polarized.

Subsequently, these photoinduced occupations decrease in the process of intraband spin-flipping. To be precise, VB holes undergo intraband m_j -flipping from $|\frac{1}{2}, -\frac{1}{2}\rangle_{VB}$ to $|\frac{1}{2}, +\frac{1}{2}\rangle_{VB}$ at a rate k_h , and analogously, CB electrons undergo intraband m_j -flipping from $|\frac{1}{2}, +\frac{1}{2}\rangle_{CB}$ to $|\frac{1}{2}, -\frac{1}{2}\rangle_{CB}$ at a rate k_e . The process of intraband spin-flipping is indicated by yellow arrows in Figure 5.3.

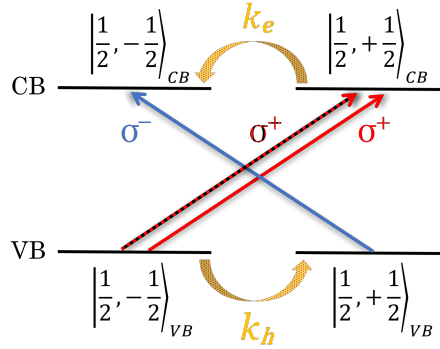


Figure 5.3: Induced optical transitions at the band gap during polarization dependent DTS including intraband spin-flip transition rates. Optical transitions are induced by a σ^+ polarized pump pulse (red-black dotted) and σ^+ (red) or σ^- (blue) polarized probe pulse. Intraband m_j -flipping dynamics are indicated by yellow arrows. VB holes spin flip at a rate k_h and CB electrons at a rate k_e .

From here on, I will mainly focus on population dynamics from the moment on, when the respective states have been populated by the pump pulse. To begin with, I will treat the transient of $(\Delta T/T)^{\sigma^+\sigma^+}$. It witnesses the depopulation of the pump-induced holes and electrons populating $|\frac{1}{2}, -\frac{1}{2}\rangle_{VB}$ (in the following abbreviated as $|\frac{1}{2}, -\frac{1}{2}\rangle_{VB}$) and $|\frac{1}{2}, +\frac{1}{2}\rangle_{CB}$ (in the

following abbreviated as $|+\frac{1}{2}\rangle_{CB}$), respectively. These dynamics can be described by the following rate equations.

$$\text{holes: } \dot{N}_{|-\frac{1}{2}\rangle_{VB}} = -k_h (N_{|-\frac{1}{2}\rangle_{VB}} - N_{|+\frac{1}{2}\rangle_{VB}}) \quad (5.1)$$

$$\text{electrons: } \dot{N}_{|+\frac{1}{2}\rangle_{CB}} = -k_e (N_{|+\frac{1}{2}\rangle_{CB}} - N_{|-\frac{1}{2}\rangle_{CB}}), \quad (5.2)$$

where N denotes the time-dependent number density of holes or electrons occupying the given state. These rate equations account for an ongoing intraband spin-flipping process for as long as there exists a population imbalance between $|-\frac{1}{2}\rangle_{VB}$ and $|+\frac{1}{2}\rangle_{VB}$, or equivalently between $|-\frac{1}{2}\rangle_{CB}$ and $|+\frac{1}{2}\rangle_{CB}$, which is insured by the terms in brackets in Equation 5.1 and Equation 5.2, respectively.

The solutions to these rate equations are

$$\text{holes: } N_{|-\frac{1}{2}\rangle_{VB}} = \frac{N_{max} - N_{balance}}{2} e^{-2k_h t} + \frac{N_{balance}}{2} \quad (5.3)$$

$$\text{electrons: } N_{|+\frac{1}{2}\rangle_{CB}} = \frac{N_{max} - N_{balance}}{2} e^{-2k_e t} + \frac{N_{balance}}{2}. \quad (5.4)$$

N_{max} defines the initial number density of holes and electrons occupying $|-\frac{1}{2}\rangle_{VB}$ and $|+\frac{1}{2}\rangle_{CB}$, respectively. Also see N_{max} denoted in Figure 5.4 below.

Furthermore, the total number of holes, $N_h = N_{|-\frac{1}{2}\rangle_{VB}}(t) + N_{|+\frac{1}{2}\rangle_{VB}}(t) = N_{balance}$, and the total number of electrons, $N_e = N_{|-\frac{1}{2}\rangle_{CB}}(t) + N_{|+\frac{1}{2}\rangle_{CB}}(t) = N_{balance}$, is identical, as equal numbers of holes and electrons are created in an absorption process of a photon. Moreover, they are constant at all times, as charge carrier recombination can be disregarded. This has been justified in Section 4.3, where k_{rec} was calculated to be 100-fold smaller than what will be found for the spin relaxation rate. Signs of recombination are also practically absent in Figure 5.1: within the first 10 – 20 ps, when spin relaxation takes place, a decrease in DT amplitude due to recombination is not perceivable. Recombination dynamics can therefore be neglected in the examination and evaluation of spin relaxation in the CsPbI₃ NCs.

Since DTS is an additive measurement of hole and electron occupations (c.f. Section 3.3), I define $N^{\sigma^+\sigma^+} = N_{|-\frac{1}{2}\rangle_{VB}} + N_{|+\frac{1}{2}\rangle_{CB}}$, which traces the depopulation of the pump-induced hole and electron populations. Hence, the addition of Equation 5.3 and Equation 5.4 gives

$$N^{\sigma^+\sigma^+}(t) = \frac{N_{max} - N_{balance}}{2} (e^{-2k_h t} + e^{-2k_e t}) + N_{balance}. \quad (5.5)$$

At the same time, the transient signal $(\Delta T/T)^{\sigma^+\sigma^-}$ witnesses the population of the initially unoccupied states $|+\frac{1}{2}\rangle_{VB}$ and $|-\frac{1}{2}\rangle_{CB}$. The corresponding rate equations can be found analogously to the ones above.

$$\text{holes: } \dot{N}_{|+\frac{1}{2}\rangle_{VB}} = +k_h (N_{|-\frac{1}{2}\rangle_{VB}} - N_{|+\frac{1}{2}\rangle_{VB}}) \quad (5.6)$$

$$\text{electrons: } \dot{N}_{|-\frac{1}{2}\rangle_{CB}} = +k_e (N_{|+\frac{1}{2}\rangle_{CB}} - N_{|-\frac{1}{2}\rangle_{CB}}), \quad (5.7)$$

Except for $N_{min} = N^{\sigma^+\sigma^-}(t=0)$ replacing $N_{max} = N^{\sigma^+\sigma^+}(t=0)$ (both are denoted in Figure 5.4 below), the solutions to these rate equations are the same as in Equation 5.3 and Equation 5.4. I will therefore continue directly with the equation describing their joint occupation, which is

$$N^{\sigma^+\sigma^-}(t) = \frac{N_{min} - N_{balance}}{2} (e^{-2k_h t} + e^{-2k_e t}) + N_{balance}. \quad (5.8)$$

Up to this point, hole and electron spin relaxation rates are treated separately, as they generally differ. However, in DTS, the occupation of electrons and holes cannot be distinguished, because it is always the sum of electrons and holes that is measured in terms of $N^{\sigma^+\sigma^+}$ and $N^{\sigma^+\sigma^-}$. Therefore, at this point it is not possible to distinguish between the spin relaxation rates of holes, k_h , and electrons, k_e . Instead, a global spin relaxation rate $k_{e\&h}$ is defined, assuming similar individual rates. Inserting $k_{e\&h}$ in Equation 5.5 results in an equivalent equation (Equation 5.10) as beginning once again with a rate equation

$$\begin{aligned} \dot{N}^{\sigma^+\sigma^+}(t) &= -k_{e\&h} (N_{|-\frac{1}{2}\rangle_{VB}} - N_{|+\frac{1}{2}\rangle_{VB}} + N_{|+\frac{1}{2}\rangle_{CB}} - N_{|-\frac{1}{2}\rangle_{CB}}) \\ &= -2k_{e\&h} (N_{|-\frac{1}{2}\rangle_{VB}} + N_{|+\frac{1}{2}\rangle_{CB}} - N_{balance}) \\ &= -2k_{e\&h} (N^{\sigma^+\sigma^+}(t) - N_{balance}), \end{aligned} \quad (5.9)$$

The solution to this rate equation is

$$N^{\sigma^+\sigma^+}(t) = (N_{max} - N_{balance}) e^{-2k_{e\&h} t} + N_{balance}. \quad (5.10)$$

Analogous to this derivation, it is straight forward to find

$$N^{\sigma^+\sigma^-}(t) = (N_{min} - N_{balance}) e^{-2k_{e\&h} t} + N_{balance}. \quad (5.11)$$

Equation 5.10 and Equation 5.11 are used to fit all transients in this chapter. As an illustration, Figure 5.4 shows the data presented in Figure 5.1 b fitted with Equation 5.10 (red) and Equation 5.11 (blue).

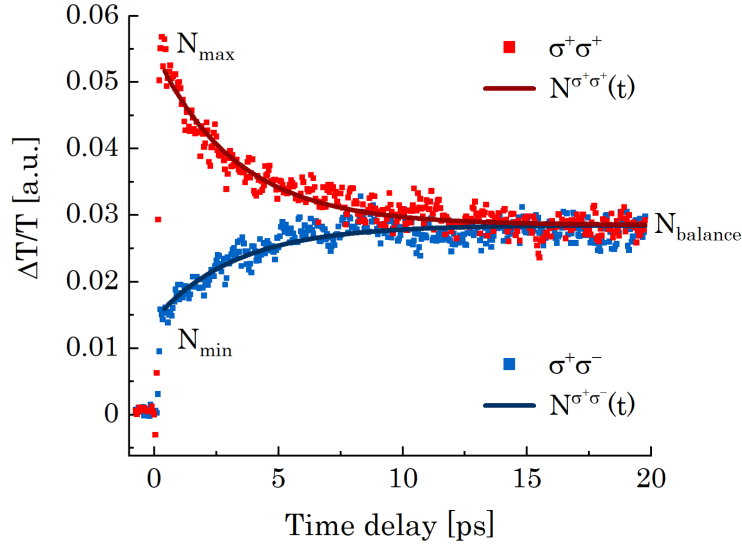


Figure 5.4: Polarization dependent DT transients fitted. The temporal evolution of $(\Delta T/T)^{\sigma^+\sigma^+}$ (red) and $(\Delta T/T)^{\sigma^+\sigma^-}$ (blue), as already shown in Figure 5.1 b, are here additionally fitted with Equation 5.10 (red curve) and Equation 5.11 (blue curve), respectively. The parameters N_{max} , N_{min} , and $N_{balance}$ are indicated.

At this point, it is natural to ask what causes the $(\Delta T/T)^{\sigma^+\sigma^+}$ (red) and $(\Delta T/T)^{\sigma^+\sigma^-}$ (blue) curves to merge. In other words, what causes the non-equilibrium spin polarization of the pump-induced charge carrier population to relax into spin-balance?

To begin with, the role of carrier-carrier interaction on spin relaxation is examined via excitation intensity dependent DTS. This will be described in the following section.

5.2 The Role of Excitation Intensity

Carrier-carrier interaction, in particular electron-hole Coulomb exchange interaction, has been identified to provide an efficient channel for spin-relaxation in doped III-V direct gap compounds,^{125,132} e.g. in n- and p- modulation doped GaAs quantum wells,¹¹² as well as in perovskites,^{36,117,165} e.g. in high-quality CsPbBr₃ single-crystalline films¹¹⁷. Spin relaxation through Coulomb exchange interaction is described by the BAP mechanism (c.f. Section 2.4).¹³²

Whether spin relaxation is governed by electron-hole exchange interaction may be tested by varying the concentration of charge carriers in the semiconductor. This is for example

achievable through diverse doping concentrations, or different photoexcitation intensities. The latter method is used here to investigate, whether Coulomb exchange interaction dominates spin relaxation in CsPbI₃ NCs.

This experiment is conducted with quasi-resonant photoexcitation of 1.92 eV pump pulse energy (c.f. Figure 5.1 a). The excitation intensity of one pump pulse, i.e. its radiative flux, ranges from 2.3 $\mu\text{J}/\text{cm}^2$ to 11.5 $\mu\text{J}/\text{cm}^2$ and induces carrier concentrations (number of photons or electron-hole pairs per cm^2) of $\frac{\text{radiative flux}}{\text{photon energy}} = 7.5 \cdot 10^{12} \text{ cm}^{-2}$ to $3.7 \cdot 10^{13} \text{ cm}^{-2}$, respectively, within the illuminated area on the CsPbI₃ sample. The experiment is conducted at RT, as well as at 50 K. The spin relaxation rates resulting from this experiment are shown in Figure 5.5.

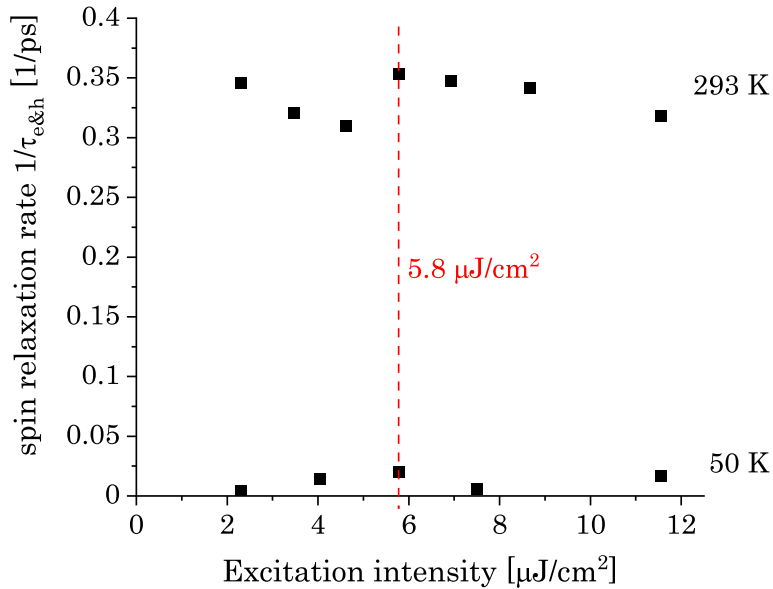


Figure 5.5: Spin relaxation rates obtained from DTS with various photoexcitation intensities. Upper (lower) data points result from DTS at RT (50 K). The dashed vertical line indicates the pump intensity used for all other DTS experiments presented in this thesis.

For both temperatures, the spin relaxation rates shown in Figure 5.5 are largely unaffected by the excitation intensity and do not follow any trend within the investigated intensity range. For all other DTS experiments presented in this thesis, an intermediate excitation intensity of 5.8 $\mu\text{J}/\text{cm}^2$ was chosen (dashed vertical line). This experiment demonstrates, that 5.8 $\mu\text{J}/\text{cm}^2$ induces a small enough charge carrier density within the investigated CsPbI₃ NCs, rendering many-body effects, such as Coulomb exchange interaction, Auger recombination and ASE insignificant, as already predicted and commented on in the beginning of Section 5.1.

This result is in contrast to the examples given above, where spin relaxation has been found to exhibit a significant dependency on excitation density. To be precise, in n- and p- modulation

doped GaAs quantum wells, the spin relaxation time increased three-fold as the excitation density is increased from $2 \cdot 10^9 \text{ cm}^{-2}$ to $1 \cdot 10^{10} \text{ cm}^{-2}$.¹¹² Note, that these densities are three orders of magnitude smaller, than those in my experiment, suggesting that an effect on the spin relaxation time in CsPbI₃ NCs would be detectable provided there is one. The authors qualitatively explain their finding with increased screening, i.e. increased relative permittivity, $\epsilon_r(\nu)$, as a result of increased carrier density (c.f. Section 2.3). This causes the exciton binding energy to decrease and simultaneously the exciton radius to increase. Consequently, the overlap between the electron and hole wavefunctions reduces, which leads to a reduction in the exchange interaction. Thus, spin relaxation occurs slower at high excitation density.

Moreover, in CsPbBr₃ high-quality single-crystalline films spin relaxation has been found to exhibit a large dependency on excitation density.¹¹⁷ However, the spin decay time behaves inversely and decreased drastically from $\approx 10 \text{ ps}$ to $\approx 1 \text{ ps}$ at pump fluences of $0.2 \mu\text{J}/\text{cm}^2$ and $90 \mu\text{J}/\text{cm}^2$, respectively. In this study, spin relaxation is not exclusively attributed to exchange interaction within one exciton, but also to inter-excitonic couplings. These provide an additional spin relaxation channel, primarily through the e-e and h-h spin-spin interaction among neighbouring excitons. This way, the authors claim, spin relaxation is accelerated at high densities.

In the here presented study on CsPbI₃ NCs, spin relaxation dynamics are identified to be independent of the excitation density (Figure 5.5). It can thus be concluded, that within the investigated density range Coulomb exchange interaction between electron and hole of the same exciton, as well as e-e and h-h spin-spin inter-excitonic interactions are insignificant in CsPbI₃ NCs. In attempt to explain the seeming discrepancy, between this and the above described studies, I want to draw attention to the fact that in CsPbI₃ NCs free (Coulomb-correlated) e-h pairs dominate at RT,⁸² as opposed to excitons. Excitons are, however, dominant in strongly quantum confined structures or large band gap LHPs, such as CsPbCl₃ ($B_X \approx 75 \text{ meV}$ in NCs)²⁰ and CsPbBr₃ ($B_X \approx 40 \text{ meV}$ in NCs)²⁰. In comparison, the exciton binding energy in CsPbI₃ NCs is $B_X \approx 20 - 23.3 \text{ meV}$ as discussed in Section 4.1. Consequently, exchange interaction between electron and hole in CsPbI₃ NCs, which, besides, show no signs of relevant size quantization (Section 4.1), is minor to begin with. Exchange interaction, i.e. the BAP mechanism, as the principal channel for spin relaxation is thus unlikely in CsPbI₃ NCs. This may provide an explanation of the contrasting experimental results discussed above. Moreover, the presented insensitivity towards excitation flux in CsPbI₃ NCs is in line with the prediction of only weak exchange interaction in polycrystalline films of the hybrid perovskite $\text{CH}_3\text{NH}_3\text{PbCl}_x\text{I}_{3-x}$, which exhibits an exciton binding energy of $B_X \approx 16 \text{ meV}$.¹⁶⁵

5.3 How LO Phonon Absorption and Emission Contributes to Spin Relaxation

The experiment and discussion in the previous section brought forward evidences against Coulomb exchange interaction, and thus the BAP mechanism, to be the primary channel for spin relaxation in CsPbI₃ NCs. This section is concerned with the role of carrier - LO phonon scattering on spin relaxation, as this interaction is a fundamental part of the two remaining most important spin relaxation theories: the EY and DP mechanism.

5.3.1 The Role of Excess Energy

Electrons (holes) may be photoexcited resonantly, as done in the experiments presented so far, or they can be excited higher up (lower down) into the CB (VB) with respect to the CB minimum (VB maximum) through excess photon energy. The question then arises: what are

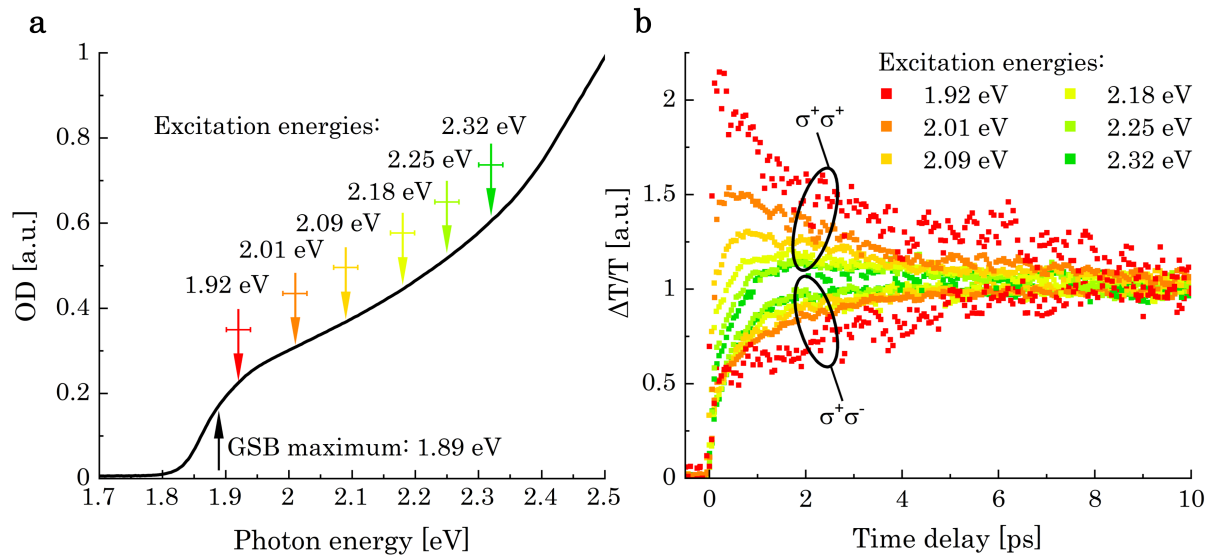


Figure 5.6: Photoexcitation energy and polarization dependent DTS. (a) Indication of the excitation (pump) energies used in this experiment. The black line is the static absorption spectrum (c.f. Figure 4.2). (b) Corresponding DTS transients of the excitation energies indicated in (a). The experiment is conducted at RT. Pump and probe polarizations are $\sigma^+\sigma^+$ (upper curves) or $\sigma^+\sigma^-$ (lower curves), as indicated by the black ovals. In order to establish comparability, all curves are normalized to a time delay of 10 ps.

the consequences of excess energy on charge carrier spin relaxation dynamics? This question is addressed by studying the dependence of $(\Delta T/T)^{\sigma^+\sigma^+}$ and $(\Delta T/T)^{\sigma^+\sigma^-}$ on the pump pulse energy at RT. As indicated in Figure 5.6 a, the pump pulse energy is gradually increased from

1.92 eV to 2.32 eV. The corresponding DT transients, all tracing the temporal evolution of the GSB maximum (1.89 eV), are shown in Figure 5.6 b.

Although similar in decay time, the DT transients exhibit major differences. Most intriguingly, SP_{max} , i.e. the maximally reached gap reached between $(\Delta T/T)^{\sigma^+\sigma^+}$ and $(\Delta T/T)^{\sigma^+\sigma^-}$, decreases dramatically with increasing excitation energy. This correlation is qualitatively well visible in Figure 5.6 b and its quantitative evaluation is plotted in Figure 5.7 a. What it reveals is that a decreasing number of carriers arrive at the respective band edge with their initial pump-induced spin polarization as the excitation energy is increased. In other words, the initial photoinduced spin imbalance of the charge carrier ensemble diminishes drastically in the process of cooling towards the band edge.

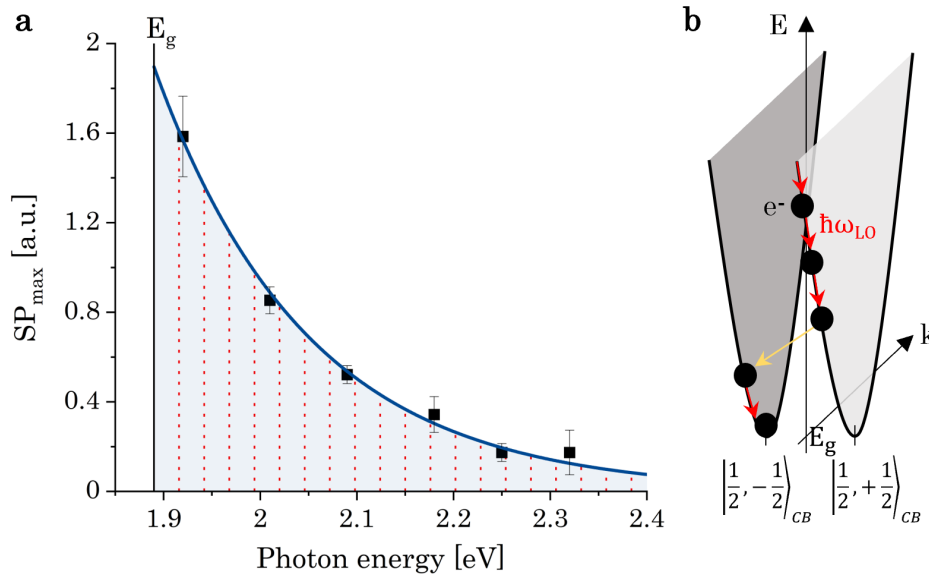


Figure 5.7: Evaluation and interpretation of photoexcitation energy dependent DT transients.

(a) SP_{max} values (black squares) are extracted from Figure 5.6 b and plotted against the corresponding photoexcitation energy. These data points are fitted with an exponential decay curve exhibiting a characteristic decay energy of 158.3 ± 6.8 meV. Vertical lines (red, dotted) are distanced from the band gap $E_g = 1.89$ eV (vertical black line) by integer multiples of 26 meV (CsPbI₃ LO phonon energy)⁸². (b) Schematic of the cooling process of an electron (black sphere), which was σ^+ photoexcited into the CB corresponding to $|\frac{1}{2}, +\frac{1}{2}\rangle_{CB}$. Red arrows indicate the emission of LO phonons. The cooling electrons statistically undergo an m_j -flip (yellow arrow) into $|\frac{1}{2}, -\frac{1}{2}\rangle_{CB}$ after every fourth to eighth phonon emission. Both conduction bands are degenerate in energy and lie at the same position in k-space.

Carrier cooling in LHPs occurs predominantly through the emission of LO phonons. To be precise, in LHPs, charge carrier - LO phonon scattering via Fröhlich interaction has been identified to dominate over other scattering processes, with acoustic phonon scattering even negligible at RT.^{70,85,120} Therefore, the strong dependence of SP_{max} on the carrier excess energy, as perceivable in Figure 5.6 b and Figure 5.7 a, unambiguously shows that carrier cooling via

LO phonon emission contributes significantly to spin depolarization.¹¹³ Furthermore, the JDOS is larger at higher energy, as it obeys a square-root dependence on energy (c.f. Equation 2.30). Consequently, energetically high excited charge carriers scatter with LO phonons at an increased rate. The ratio of LO phonon scattering type, i.e. spontaneous emission, stimulated emission or even absorption, with respect to energy in CsPbI₃ at RT is shown in Figure 2.8. It clarifies that already from $E/\hbar\omega_{LO} \geq 1.2$ on towards higher carrier energies phonon emission (spontaneous plus stimulated) markedly exceeds phonon absorption.

A schematic visualizing the process of spin depolarization during phonon emission, i.e. cooling, is depicted exemplarily for CB electrons (black spheres) in Figure 5.7 b and can be respectively understood for VB holes. This schematic aids to describe the step-by-step process of charge carrier spin-flipping during cooling: the σ^+ polarized pump pulse photoexcites electrons into $|\frac{1}{2}, +\frac{1}{2}\rangle_{CB}$ ¹, with the height depending on the excess pulse energy with respect to the band gap energy. Subsequent cooling via LO phonon emission is indicated in Figure 5.7 a by dotted red lines with a spacing of the LO phonon energy of $E_{LO} \approx 26.3 \pm 7.0 meV$ (as characteristic for CsPbI₃ NCs⁸²) and in Figure 5.7 b by red arrows. With every LO phonon emission the magnitudes of the electron's energy and wave vector reduce according to that of the emitted LO phonon. In other words, the cooling electron distributes its excess energy to the crystal in form of LO lattice vibrations and thus successively approaches the band edge. This successive arrival of both, electrons and holes, at the respective band edges is traced by the initial rise of the $(\Delta T/T)^{\sigma^+\sigma^+}$ transients in Figure 5.6 b. The fast rise at low excitation energy signifies almost immediate occupation of the $|\frac{1}{2}, +\frac{1}{2}\rangle_{CB}$ and $|\frac{1}{2}, -\frac{1}{2}\rangle_{VB}$ band edges. Toward higher excitation energies, the initial fast rise of $(\Delta T/T)^{\sigma^+\sigma^+}$ flattens, indicating only gradual occupation of the band edge states, which is determined by the speed of cooling.⁷⁰

During the cooling process, an electron transitions from the $|\frac{1}{2}, +\frac{1}{2}\rangle_{CB}$ to the degenerate $|\frac{1}{2}, -\frac{1}{2}\rangle_{CB}$ band after a statistical amount of n LO phonon emissions. This spin flip, i.e. to be precise, m_j -flip, is represented by a yellow arrow in Figure 5.7 b. In order to evaluate n , first the total number of LO phonon emissions necessary to reach the band edge is calculated for lowest and highest excitation energy, respectively.

$$\frac{1.92 eV - 1.89 eV}{0.0263 \pm 0.007 eV} = 1.1 \pm 0.5 \text{ cumulative LO phonon emissions from e and h.}$$

$$\text{This corresponds to } 0.6 \pm 0.3 \text{ LO phonon emissions individually from e and h.} \quad (5.12)$$

¹This state is strictly speaking only exact at the CB band edge, i.e. at $\vec{k} = 0$. For wave vectors deviating from the zone center ($\vec{k} \neq 0$) spin up and spin down states begin to mix as a consequence of SOC.¹⁰⁵ (c.f. Section 2.5.) However, for the purpose of clarity, here, the entire band will be referred to by its band edge state.

$$\frac{2.32 \text{ eV} - 1.89 \text{ eV}}{0.0263 \pm 0.007 \text{ eV}} = 16.3 \pm 6 \text{ cumulative LO phonon emissions from e and h.}$$

$$\text{This corresponds to } 8.2 \pm 3 \text{ LO phonon emissions individually from e and h.} \quad (5.13)$$

Figure 5.6 b shows that $SP_{max} \neq 0$ for all excitation energies, i.e. a gap exists between $(\Delta T/T)^{\sigma^+\sigma^+}$ and $(\Delta T/T)^{\sigma^+\sigma^-}$ transients for all excitation energies and most notably even for the highest one of 2.32 eV. This implies that not every carrier - LO phonon scattering event inevitably involves spin-flipping. Rather, multiple emissions are statistically necessary for a carrier's spin to flip.

At this point it is important to specify the term “spin-flip”. Recall, that the CB electron's degree of spin polarization is $-1/3$ of its degree of total angular momentum orientation (Subsection 2.1.3). Therefore, the term “spin-flip” refers to m_j -flip, rather than m_s -flip. In the case of holes $m_j = m_s$, which implies no differentiation between m_j - and m_s -flip is necessary. The correlation between SP_{max} and photoexcitation energy is of exponential nature as evident by the exponential decay curve fitted to the data in Figure 5.7 a. Its characteristic decay energy resulting from the best fit is $0.158 \pm 0.007 \text{ eV}$. This energy corresponds to 6 ± 2 cumulative LO phonon emissions from CB electrons and VB holes. Hence, the exponential SP_{max} decay in the CsPbI₃ NCs is characterized by four to eight LO phonon emissions in the process of carrier cooling. Ultimately, this implies that the exponential decay of photoinduced spin polarization is characterized by four to eight LO phonon emissions.

The majority of charge carriers have cooled down to the band edges at the instant when $(\Delta T/T)^{\sigma^+\sigma^+}$ in Figure 5.6 b finishes growing and reaches its peak magnitude. From this instant on, spin relaxation as seen in Figure 5.1 b commences until the photoinduced non-equilibrium spin polarization is balanced, i.e. until the $(\Delta T/T)^{\sigma^+\sigma^+}$ and $(\Delta T/T)^{\sigma^+\sigma^-}$ transients have merged. The corresponding spin relaxation rates have been extracted through curve fitting (as described in Section 5.1 and shown in Figure 5.4). These are plotted against the photoexcitation energy in Figure 5.8. Spin relaxation rates for all excitation energies excluding the highest (which will be addressed later) exhibit similar magnitudes, i.e. within a narrow interval $0.35 \text{ ps}^{-1} \leq k_{e\&h} \leq 0.45 \text{ ps}^{-1}$ (shaded area). However, at magnified scale, as shown in the inset, a trend towards higher spin relaxation rates with increasing excitation energy is unambiguously observable. If spin relaxation is driven by phonon scattering via the EY mechanism, this trend is not surprising: as a consequence of carrier cooling, a large non-equilibrium phonon population enlarges the carrier - phonon scattering cross-section and

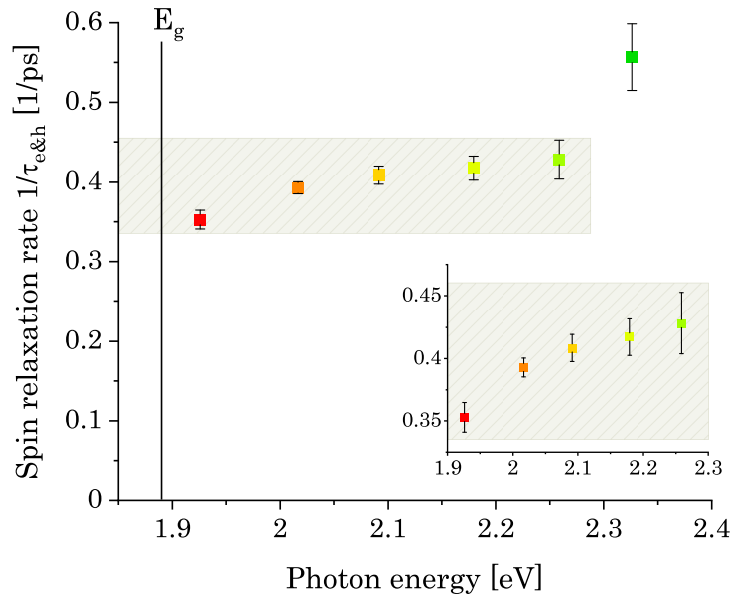


Figure 5.8: Influence of excess photoexcitation energy on spin relaxation rate. Charge carrier spin relaxation rate is extracted from Figure 5.6 b and plotted against the respective photoexcitation energy. The inset shows an enlargement of the shaded area.

thus accelerates EY spin relaxation.¹¹² Explicitly, the scattering cross-section increases with increasing phonon density, because then phonon absorption (as opposed to emission during carrier cooling) becomes more likely. It is much smaller for a phonon occupation number solely determined by the lattice temperature. Therefore, spin relaxation rates increase for those charge carriers, which were originally excited with large photon energies.

Moreover, optical phonons created near the zone center have low dispersion and therefore small group velocities, such that the vast majority remains within the photoexcited volume. This provokes re-absorption of emitted LO phonons by carriers, a phenomena well known as the “hot-phonon effect”. Another evidence, that this effect is indeed present in the examined CsPbI₃ NCs, can be deduced from fact that the slopes of the initial rise of $(\Delta T/T)^{\sigma^+\sigma^+}$ decrease with increasing excitation energies. It suggests that charge carrier cooling slows down for high excitation energies, which can be explained through re-absorption of emitted LO phonons, i.e. the hot-phonon effect. In fact, this effect is long known to be present in GaAs and has also been observed previously in LHPs.^{70,164,166}

The here detected hot-phonon effect in CsPbI₃ NCs, in combination with the determination of increasing spin relaxation rates resulting from elevated excitation energies (Figure 5.8) shows once more, that LO phonon scattering contributes significantly to spin relaxation in these NCs. The EY spin relaxation rate increases with a higher carrier scattering rate according

to $\frac{1}{\tau_{EY}} \propto \frac{1}{\tau_m}$ (Equation 2.80), while it decreases in the DP model as $\frac{1}{\tau_{DP}} \propto \tau_m$ (c.f. Section 2.4). This suggests that spin relaxation in CsPbI₃ NCs is driven by the EY, rather than the DP mechanism.

A short remark on the somewhat remote data point in Figure 5.8 at highest excitation energy. The following considerations are an attempt to speculatively reason why it does not follow the trend of all remaining data points in the same graph. As visible in the static absorption spectrum in Figure 5.6 a, at the largest photon energy of 2.32 eV the OD curve no longer exhibits square root dependence. Consequently, parabolic band approximation is no longer justified. Moreover, valleys of the electronic band structure at other crystal symmetry points may be populated by such hot charge carriers (c.f. Figure 2.1).¹⁶⁷ All this affects spin relaxation dynamics and might explain why the discussed data point does not follow the trend of the data points at lower energies.

To summarize the findings of the experiments shown and evaluated in this section, the EY mechanism appears suitable once more to explain spin relaxation in CsPbI₃ NCs. To even further test this hypothesis, the effect of carrier-LO phonon scattering on spin dynamics was further investigated through temperature dependent DTS and is presented in the next section.

5.3.2 Freezing Out Phonon Scattering and Spin Relaxation

In this section, spin relaxation dynamics are studied through temperature dependent DTS for temperatures in the range $4\text{ K} \leq T \leq 300\text{ K}$. Upon temperature reduction, a red-shift of the band gap energy E_g is observed in the CsPbI₃ NCs as common in LHPs (c.f. Subsection 2.1.1).^{78–83} The shift in my experiment amounts to $E_g(300\text{ K}) - E_g(4\text{ K}) = 77\text{ meV}$, similar to what has been reported previously.⁸² Meanwhile, the black-phase γ -CsPbI₃ is maintained, as no crystal phase transitions occur within this temperature range.^{75,93} Due to the band gap red-shift upon temperature reduction the absolute values of the pump laser energies were adjusted accordingly for all temperatures in order to precisely retain the resonant pumping condition. All transients are evaluated at their temperature-specific GSB maximum.

Spin-related effects due to carrier cooling, as examined in the last section, are eliminated in the resonant pumping condition. Consequently, if carrier cooling is absent, no accompanied LO phonon emission takes place and the LO phonon occupation is determined by lattice temperature. To be precise, the LO phonon occupation number, $n_{LO}(T)$, is determined by Bose-Einstein statistics (c.f. Equation 2.56 and Figure 2.7) and is thus accessible and adjustable by varying the temperature. As opposed to LO phonon emission, which requires the charge

carrier to have excess energy with respect to the band edge, LO phonon absorption is in principle always possible, i.e. as long as LO phonon modes are thermally excited in the material. Because $n_{LO}(T)$ is reduced at low temperatures, the probability of LO phonon absorption by a charge carrier is reduced accordingly. If spin relaxation is governed by carrier - LO phonon scattering via the EY mechanism, then a reduction of scattering events through a drop of the LO phonon occupation number is expected to prolong spin relaxation. Note, that scattering refers to both, LO phonon emission and absorption, where the effect of the former on spin relaxation was examined in the last section, while the effect of the latter on spin relaxation will be elaborated in this section's experiment.

Figure 5.9 a shows $SP(t)$ for two representative temperatures, 50 K and 250 K, on a logarithmic scale. The decay of $SP_{250 K}(t)$ is monoexponential. In contrast, that of $SP_{50 K}(t)$ shows an initial fast decay promptly converting into a slow decay after approximately 3 ps. Detailed data analysis reveals a linear plus exponential decay, i.e.

$$SP(t) = SP_{lin} \cdot \left(-\frac{t}{\tau_{lin}}\right) \Big|_{t \lesssim 3 \text{ ps}} + SP_{exp} \cdot \exp\left(-\frac{t}{\tau_{exp}}\right) \Big|_{t \gtrsim 3 \text{ ps}}. \quad (5.14)$$

Because $SP(t)$ is a measure of merging dynamics of the $(\Delta T/T)^{\sigma^+\sigma^+}$ and $(\Delta T/T)^{\sigma^+\sigma^-}$ transients, $1/\tau$ in Equation 5.14 connotes the decay rate of the photoinduced spin imbalance and therefore the rate of spin relaxation. This motivates to attest the different decay functions different underlying spin relaxation mechanisms: one, which dominates for the first ≈ 3 ps and another one which dominates thereafter.

From here on the focus will be put on the exponential spin polarization decay, i.e. that occurring in the regime $t \gtrsim 3$ ps and its dependence on temperature will be elaborated.

Figure 5.9 a shows that for $t \gtrsim 3$ ps a striking gap opens between $SP_{50 K}(t)$ and $SP_{250 K}(t)$. At 50 K, the corresponding DTS transients do not merge for several tens of picoseconds, whereas at 250 K they merge within ≈ 11 ps. In fact, the spin relaxation time, τ_{exp} , is more than one order of magnitude larger at 50 K ($\tau_{exp} = 32$ ps) than at 250 K ($\tau_{exp} = 3$ ps). Quantitatively, this is also well resolved in Figure 5.9 b, which shows that the slopes of $SP_{50 K}(t)$ and $SP_{250 K}(t)$ differ substantially, with the former significantly smaller than the latter in absolute magnitude.

The spin relaxation rates $1/\tau_{exp}$ at all measured temperatures are plotted in Figure 5.10 and are comparable to those of other publications on LHPs.^{134–136,165} The graph reveals that $1/\tau_{exp}$ diminishes upon temperature reduction. In other words, spin relaxation is prolonged as the phonon occupation, $n_{LO}(T)$, is diminished. The above stated expectation has thus been

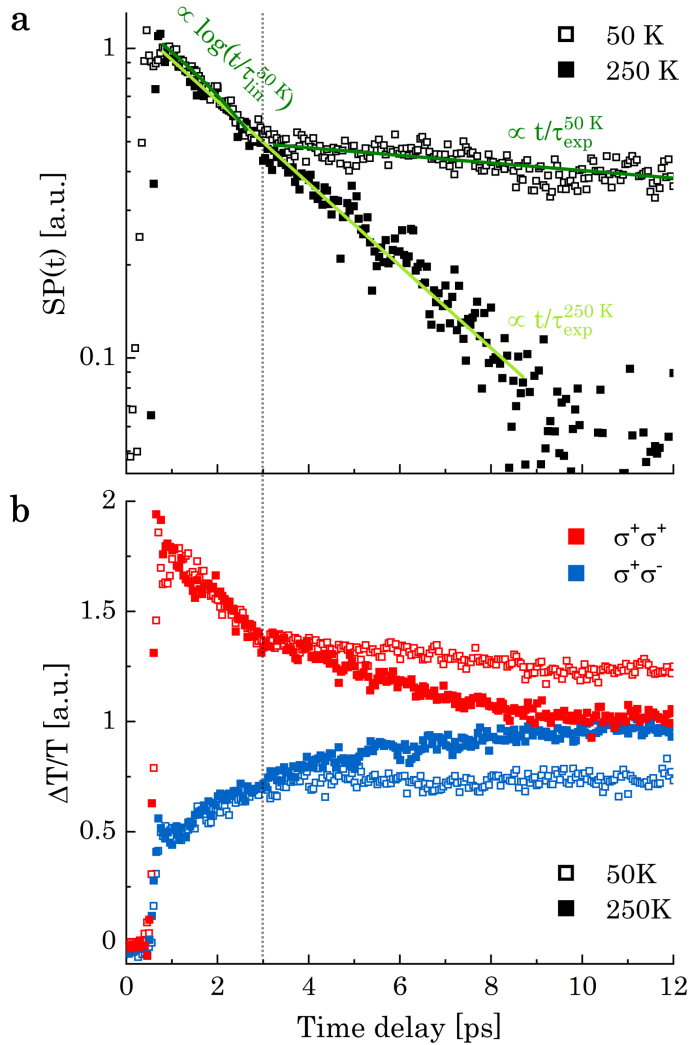


Figure 5.9: Spin polarization decay at 50 K and 250 K. (a) $SP(t)$ is plotted on a logarithmic scale against time. The data corresponding to 50 K (open squares) is fitted logarithmically for $t \leq 3$ ps and linearly for $t \geq 3$ ps (dark green lines). The dotted vertical line at $t = 3$ ps is a guide to the eye for differentiating between the two distinct spin relaxation regimes. Data corresponding to 250 K (filled squares) is fitted linearly throughout both regimes (bright green line). (b) Normalized DTS transients at 50 K (open squares) and 250 K (filled squares). $\sigma^+\sigma^+$ polarized transients are represented in red, those with $\sigma^+\sigma^-$ polarization are represented in blue.

fulfilled and it can be inferred that spin relaxation in CsPbI₃ NCs is strongly influenced by LO phonon absorption – in addition to LO phonon emission (c.f. Subsection 5.3.1). To consider this qualitative statement more quantitatively, the spin relaxation rates shown in Figure 5.10 are compared to theoretical predictions. Clearly, the lattice temperature of the CsPbI₃ NCs strongly affects intrinsic spin relaxation, because the data points follow the functionality of LO phonon occupation, $n_{LO}(T)$, as dictated by Bose-Einstein statistics (light gray dotted line). As derived in Section 2.5, spin relaxation as a consequence of carrier - LO phonon scattering

may be described by the EY theory. The corresponding EY spin relaxation rate is

$$\frac{1}{\tau_{EY}} = \gamma \frac{1}{\tau_m} \left(1 - \frac{m^*}{m_0}\right)^2 \left(\frac{E}{E_g}\right)^2 \frac{2\eta^2(2-\eta)^2}{(3-\eta)^2}. \quad (5.15)$$

Concentrating on those terms depending on temperature, Equation 5.15 reduces to

$$\frac{1}{\tau_{EY}} \propto \frac{1}{\tau_m} T^2. \quad (5.16)$$

The momentum scattering rate $1/\tau_m$, which is given in Equation 2.60, contains one term describing LO phonon absorption and the other term describing LO phonon emission. For resonant photoexcitation, the emission term can be omitted, as the charge carriers are induced at the band edge, below the threshold for LO phonon emission, i.e. $\frac{E}{\hbar\omega_{LO}} < 1$. In this case it

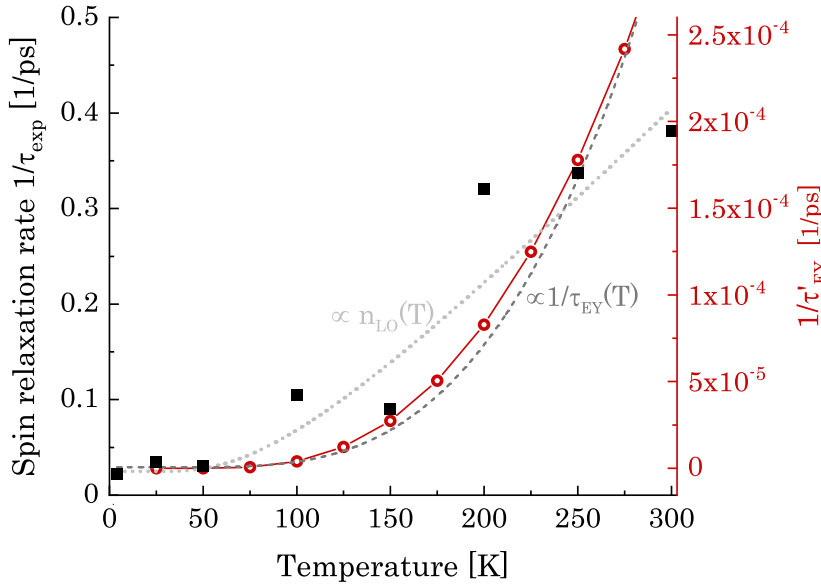


Figure 5.10: Spin relaxation rates versus temperature including theoretical model predictions. Spin relaxation rates (black data points) were determined from the decay of $SP_{exp}(t)$. The following functions are fitted to the data: LO phonon occupation number, $n_{LO}(T)$, Equation 2.56 (light gray dotted line), the prediction of EY spin relaxation taking into account exclusively phonon absorption, while disregarding phonon emission, $1/\tau_{EY} \propto n_{LO} T^2$, Equation 2.80 and Equation 2.81 (dark gray dashed line), and the numerically calculated EY spin relaxation rate, $1/\tau'_{EY}$, Figure 5.11 (linked red open circles) corresponding to the y-scale on the right.

is easily observable from Figure 2.8 that only LO phonon absorption contributes to carrier - LO phonon scattering. From the underlying function given in Equation 2.58, as well as from Equation 2.60 it can be deduced that $1/\tau_m(T) \propto n_{LO}(T)$ for $\frac{E}{\hbar\omega_{LO}} < 1$, as already discussed in Section 2.3. With this, the temperature dependency of the EY spin relaxation rate for resonant

photoexcitation becomes

$$\frac{1}{\tau_{EY}}(T) \propto n_{LO}(T) T^2, \quad \text{for } \frac{E}{\hbar\omega_{LO}} < 1. \quad (5.17)$$

This functionality is fitted to the measured spin relaxation rates and shown as a dark gray dashed line in Figure 5.10.

Strictly speaking, Equation 5.15 is valid only for elastic scattering processes, as discussed in Section 2.5. Nevertheless, this equation has been used extensively in the literature to describe also highly non-elastic processes, such as polar optical phonon scattering.^{10,125,148} The use of this equation to describe spin relaxation, which is predominantly driven by polar phonon scattering, as in the present case, may therefore be done only with great caution. It is therefore interesting to furthermore consider the numeric solution of the EY spin relaxation rate, which takes inelastic momentum scattering into account here. The derivation in Section 2.5 leads to

$$\frac{1}{\tau'_{EY}} = W_0 \frac{\hbar^2 \omega_{LO}^2}{E_g^2 \sqrt{\pi} (k_B T)^{3/2}} \frac{\eta^2 (2 - \eta)^2}{(3 - \eta)^2} \int e^{-\frac{E}{k_B T}} [n_{LO} A(E) + (n_{LO} + 1) B(E)] \sqrt{E} dE. \quad (5.18)$$

For description of the variables please refer to Equation 2.82 ff. in Section 2.5. Equation 5.18 still includes an integral, which cannot be treated analytically and thus requires a numerical procedure to be solved. The numerical solution for the EY spin relaxation rate in GaAs, which I have found is shown in Figure 5.11 (squares) and is in close accordance with the originally published graph¹²². In addition, I have repeated the same numerical procedure for CsPbI₃ by exchanging all values specific for the GaAs CB with those specific for the CsPbI₃ VB. All intermediate results needed for the numerical calculations are given in Section A.1. The numerically obtained EY spin relaxation rates for CsPbI₃ (circles) are plotted against temperature in Figure 5.11, together with those obtained for GaAs.

Although the generated graph for CsPbI₃ is in accordance with that of GaAs, $\tau'_{EY, CsPbI_3}$ must nevertheless be used with caution to predict EY spin relaxation in CsPbI₃, because the derivations resulting in Equation 5.15 and Equation 5.18 were done for GaAs and not for LHPs. Simply assuming an inverted band structure of both materials, while disregarding all other differences, such as for example the larger ionicity in the LHP lattice, might be too unmindful. However, the tentative usage of $\tau'_{EY, CsPbI_3}$ might be still of value, in the same way as Equation 5.15 has been used extensively to describe polar phonon mediated EY spin relaxation.

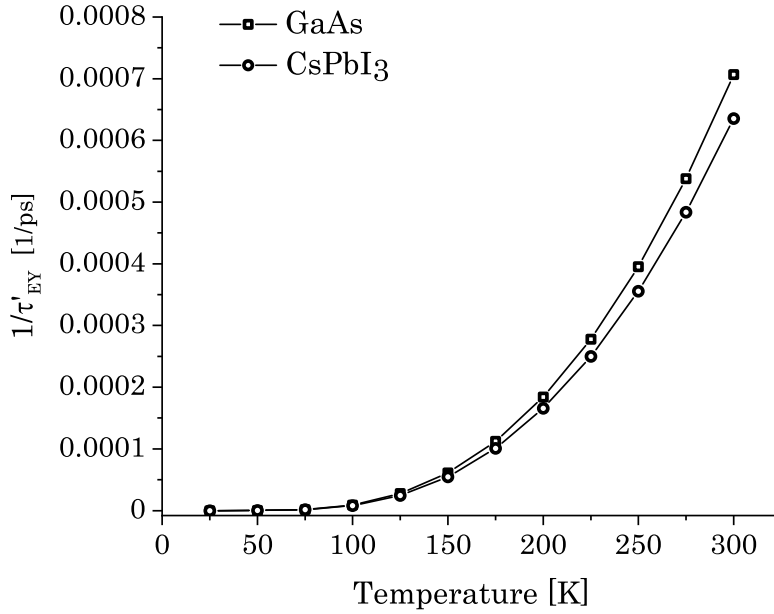


Figure 5.11: Numerically generated EY spin relaxation rate. The cause for spin relaxation includes inelastic momentum scattering. Data points are numerically generated solutions of Equation 5.18.

Finally, the numerically determined EY spin relaxation rates, $1/\tau'_{EY}(T)$, calculated for absent LO phonon emission, i.e. $B(E) = 0$, are included in Figure 5.10 (red open circles). A separate y-scale (red axis on the right) is necessary, because the numerically determined rates deviate roughly three orders of magnitude from the ones measured in CsPbI₃ NCs. This major deviation reveals that spin relaxation occurs roughly 1000-times faster in LHPs than predicted from Equation 5.18, which was derived for GaAs. Speculatively, I assign it to the orthorhombic (or quasi-cubic) crystal structure of CsPbI₃, compared to the zinc blende crystal structure of GaAs, as well as to the significant mechanical softness and ionicity of the LHP crystal lattice. A precise examination of the underlying reason for the large deviation is, however, unfortunately, beyond the scope of this thesis and requires further comparative experiments between the two material classes. It is, however, still worthwhile, to include this numerical prediction into Figure 5.10, because it opens the opportunity of comparing the functionalities of measured and calculated spin relaxation rates.

Further analyzing Figure 5.10, it is apparent, that the measured spin relaxation rates converge to an offset value greater than zero, i.e. $\approx 0.03 \text{ ps}^{-1}$ as $T \rightarrow 0$. The fit functions $\propto n_{LO}(T)$ and $\propto 1/\tau_{EY}$, as well as the y-scale corresponding to $1/\tau'_{EY}$ (red axis on the right) are therefore given an offset of the same magnitude. This offset suggests that small but measurable temperature-independent spin relaxation is present, which could be caused by defects in the CsPbI₃ crystal

lattice.¹³⁰ Impurities are reported to be almost negligible with regard to optical properties in inorganic LHPs.⁸² This could explain the small magnitude of the offset, or render impurities, as opposed to crystal defects of other kind, insignificant.

The measured spin relaxation rates clearly follow the functionality of LO phonon occupation (light gray line). A reduction of the phonon occupation by lowering the temperature comes along with prolonged band edge spin relaxation. Therefore, it can be concluded that the number of LO phonon modes available for absorption by charge carriers directly relates to the rate of charge carrier spin relaxation in CsPbI₃ NCs. This is consistent with the effect of the quantity of LO phonon emissions on the magnitude of residual band edge spin polarization (c.f. Subsection 5.3.1). Both, analytically (dark gray dashed line) and numerically (red open joint circles) determined EY spin relaxation is predicted to accelerate with increasing temperature alike the measured rates and fit them adequately.

Besides the EY mechanism, also the DP spin relaxation mechanism contains a dependency on the LO phonon scattering, as it is inversely proportional to the momentum scattering rate, i.e. $\frac{1}{\tau_{DP}}(T) \propto \frac{1}{n_{LO}(T)} T^3$ (c.f. Section 2.4). It is thus instructive to compare also its functionality to the data, which is shown in Figure 5.12 (turquoise dash-dotted line). Evidently, the spin relaxation rates measured in CsPbI₃ NCs cannot be described through the prediction of the DP

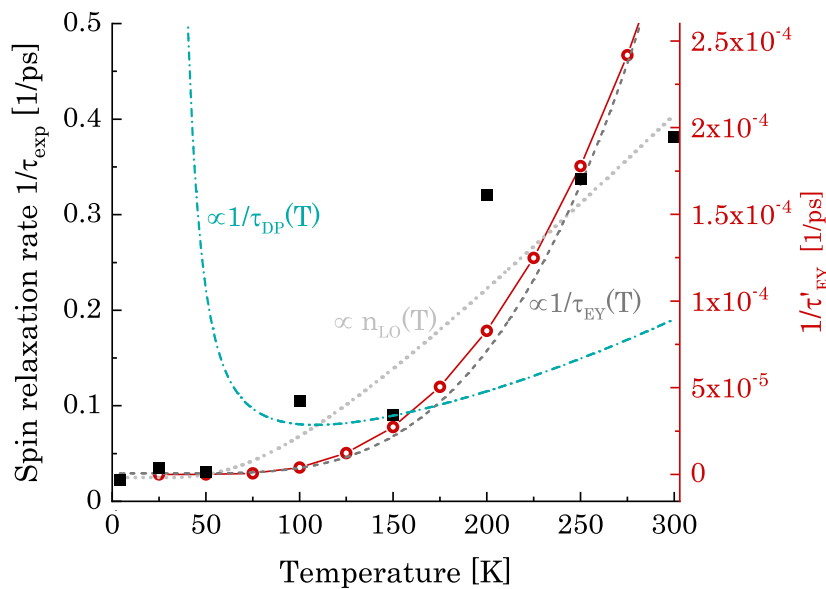


Figure 5.12: Incapability of the DP mechanism to describe the measured spin relaxation rates. This is the equivalent graph as already shown in Figure 5.10. However, here, the functionality of the DP spin relaxation is included, i.e. $\frac{1}{\tau_{DP}}(T) \propto \frac{1}{n_{LO}(T)} \cdot T^3$ (turquoise dash-dotted line). Clearly, it is incapable of describing the measured spin relaxation rates (solid black squares) in CsPbI₃ NCs.

model. Especially those spin relaxation rates at $T \lesssim 75 \text{ K}$, which converge towards a constant offset of $\approx 0.03 \text{ ps}^{-1}$, are worst represented by the DP functionality. At these low temperatures the dominant term in the DP functionality is $\frac{1}{n_{LO}(T)}$, which causes the steep rise as $T \rightarrow 0$. In contrast, towards higher temperature, it is the T^3 -term, which dominates and, without fitting the data well, at least shows the same upwards trend as the data. Nevertheless, it is clear, that the DP theory is incapable of describing spin relaxation in CsPbI₃ NCs. With this, not only theoretical arguments as given in Section 2.4 render the DP mechanism unsuitable, but also experimental evidence, as has been shown now.

Despite beyond the scope of this thesis, I want to briefly consider the origin of the linear spin polarization decay, i.e. that occurring for low temperatures, $T < 100 \text{ K}$, within the first few picoseconds, $t \lesssim 3 \text{ ps}$ (Figure 5.9). Figure 5.13 a shows the decay of $SP(t)$ at $T = 4 \text{ K}$, 25 K and 50 K on a logarithmic scale. Linear fits are depicted as solid lines and appear logarithmically on a logarithmic scale. The individual spin relaxation rates were extracted from these fits and are plotted in Figure 5.13 b. They increase drastically with decreasing temperature, i.e. as $T = 50 \text{ K} \rightarrow 4 \text{ K}$. In other words, spin relaxation accelerates drastically and its rate increases by $\approx 35\%$. This behaviour cannot be explained by carrier - LO phonon scattering via the EY mechanism, because LO phonons are scarce at these low temperatures (c.f. Figure 2.7).^{38,82}

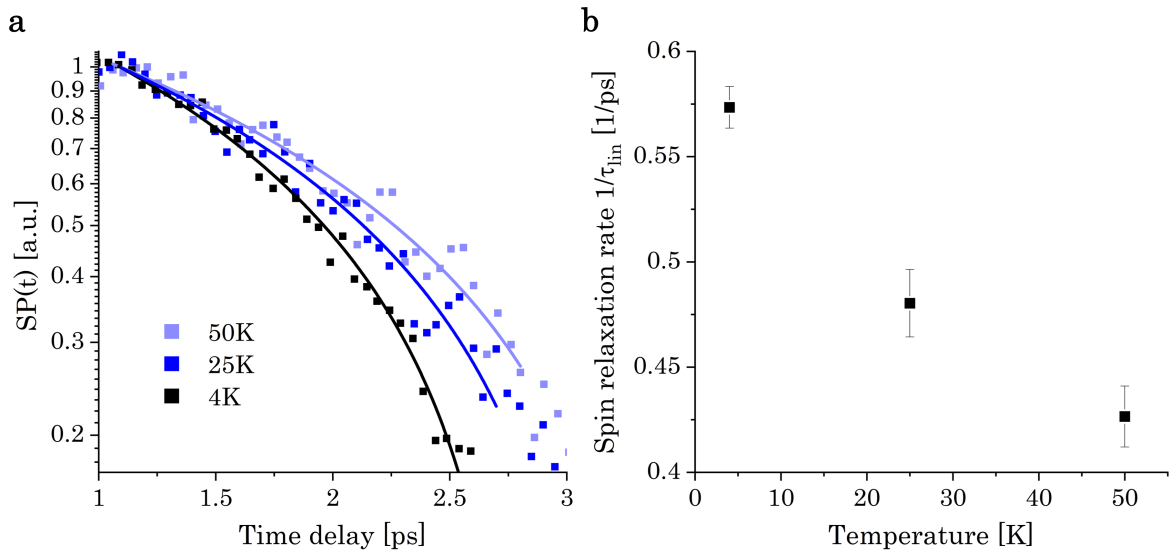


Figure 5.13: Linear spin polarization decay occurring in the temporal regime $t \lesssim 3 \text{ ps}$ and for temperatures $T=4 \text{ K}$, 25 K and 50 K . (a) Normalized $SP(t)$ is plotted on a logarithmic scale against time. Linear fits (solid lines) appear logarithmically on logarithmic scale. (b) Corresponding spin relaxation rates reveal a vast acceleration of spin relaxation dynamics as $T = 50 \text{ K} \rightarrow 4 \text{ K}$. Note that the y-scale begins at 0.4 ps^{-1} .

Hence, I infer that the underlying process must be governed by a different spin relaxation mechanism within this regime.

It may be interpreted as an excitonic response, as the ratio of excitons to free carriers increases with decreasing temperature, because thermally assisted exciton dissociation ceases. In the case of excitons, spin relaxation is caused by other mechanisms, for example through Coulomb-mediated exchange interaction between the Coulomb-bound electron and hole via the BAP mechanism.^{131,132} Alternatively, the described increase in spin relaxation rate could be explained through hyperfine interaction between the charge carrier spin and the spin of the nucleus. It was shown that in CsPbBr₃ NCs hyperfine interaction is the main cause for spin dephasing at temperatures $T < 50\text{ K}$.⁴² Moreover, hyperfine interaction between predominantly hole and nucleus spins is found to dominate low temperature ($T < 100\text{ K}$) spin dephasing in CsPbBr₃ single crystals.³⁶ Nevertheless, the described spin dynamics have not been analysed and reported to the same precision as I have observed them in CsPbI₃ NCs and are thus still subject of current research.

Summarizing this section, spin polarization dynamics were quantitatively studied with excitation energy and temperature. Thereby, the EY mechanism was identified to dominate spin relaxation in CsPbI₃ NCs (except for $T \leq 50\text{ K}$ at $t \lesssim 3\text{ ps}$). Meanwhile DP spin relaxation was shown to be incapable of reproducing the measurement data.

The results of this chapter are shown in my first-author publication, which was released in 2020.¹¹³ Since then it was cited several times, indicating that the community builds on it. Notably, two review publications explicitly re-published Figure 5.9 b, including the above elaborated interpretation and conclusion on spin relaxation in CsPbI₃ NCs.^{39,168} With the aim of understanding the big picture of intrinsic charge carrier spin dynamics, the mentioned reviews and several further publications use the knowledge gained from my results and compare it to their results in other investigated materials, such as CsPbBr₃¹⁶⁹, CsPb(Cl_{0.56}Br_{0.44})₃¹⁷⁰, or magnetic manganese hybrid organic–inorganic crystals¹⁷¹. All in all, the current knowledge about spin dynamics in LHPs and related materials is that there is not one mechanism explaining spin relaxation in all. Rather, different mechanisms are dominant in different materials - a wonderful situation for phrasing the question: “what is the reason for the diverse behaviour of charge carrier spin in different materials?” and to learn about the interplay between spin and material properties.

CHAPTER 6

Distinction between Electron and Hole Spin Relaxation

In the previous chapter, spin relaxation dynamics were evaluated jointly for electrons and holes. Recognizing that spin relaxation dynamics in general differ for different (quasi-) particles, i.e. electron, hole, exciton, and others, is a prerequisite for obtaining an in depth comprehension of the intrinsic properties of LHPs. However, DTS, by its nature, does not allow the distinction between CB electrons and VB holes, as it is an additive measurement technique of the respective occupancies, f_e and f_h . To be precise, $(\Delta T/T) \approx (f_e + f_h) \alpha_{WL} l$ (Equation 3.8).

Therefore, in this chapter, the acceptor material PCBM is employed, which acts as an electron scavenger in combination with CsPbI₃ NCs. This is a consequence of the type II heterojunction between PCBM and CsPbI₃ (c.f. Figure 3.1).¹⁵¹ Thus, photoexcited electrons are scavenged by PCBM and physically leave CsPbI₃, while holes remain on CsPbI₃, as described in detail in Subsection 3.1.2. My co-authors and I were the first ones to employ this material system for the study of spin relaxation dynamics in CsPbI₃ NCs.¹⁵⁴ It enabled us to unambiguously separate electron and hole spin relaxation rates. This chapter shows the results obtained from examination and comparison of pure CsPbI₃ NCs and the CsPbI₃ NC : PCBM blend through polarization dependent DTS at RT.

6.1 Spin-Independent Characterization of CsPbI₃ NCs versus CsPbI₃ NC : PCBM

DTS experiments in this chapter were again executed meeting the resonant pumping condition in order to eliminate spin-related effects of carrier cooling (c.f. Subsection 5.3.1). The recorded spectra were evaluated at the GSB maximum.

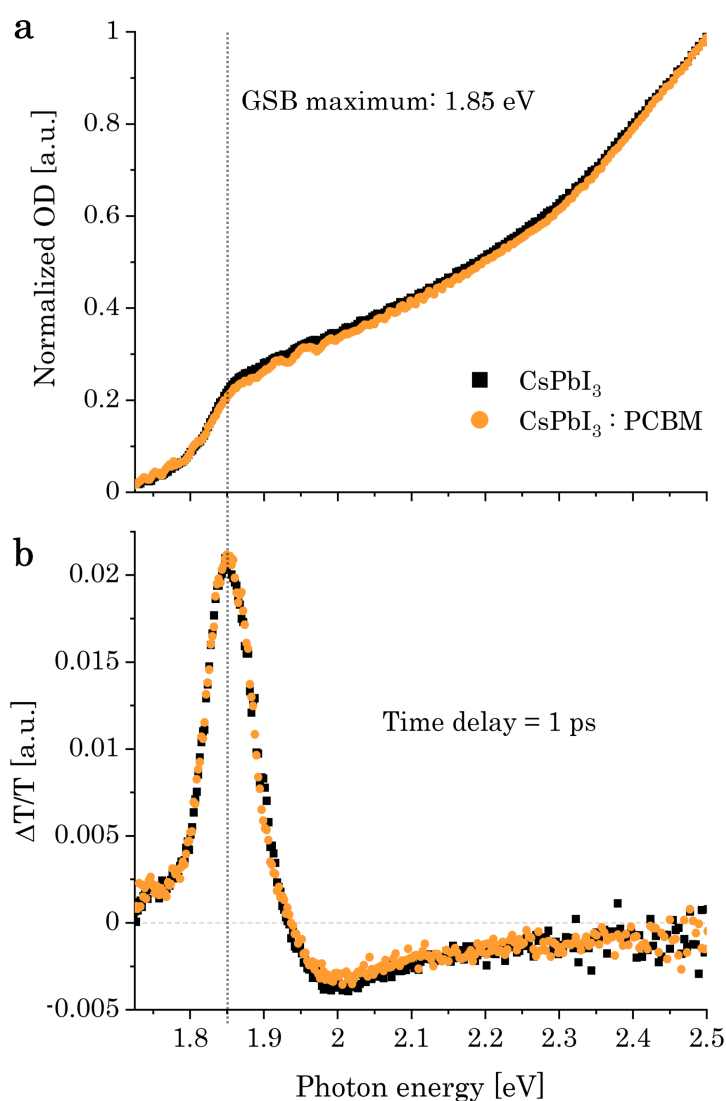


Figure 6.1: Static absorption and DT spectra of pure CsPbI₃ NCs and the CsPbI₃ NC:PCBM blend. (a) Static absorption spectra (unpolarized) of pure CsPbI₃ (black squares) and CsPbI₃:PCBM blend (orange circles) are nearly identical. The spectra are base-line corrected and normalized for best comparability. (b) Linearly polarized DT spectra at 1 ps time delay. These are also nearly identical for both samples. The GSB maximum at 1.85 eV is indicated by a vertical black dotted line, which extends into graph (a).

Figure 6.1 shows that static absorption spectra (a) and DT spectra (b) are nearly identical for both, pure CsPbI₃ NCs (black squares) and the CsPbI₃ NC : PCBM blend (orange circles). This is to be expected, because PCBM, by its nature, barely absorbs at energies relevant for CsPbI₃ band gap absorption.^{172,173} Importantly, the extraordinary similarity between the spectra of both samples is a strong indication that PCBM does not chemically affect the CsPbI₃ NCs. Rather, it suggests that PCBM simply settles on the surface of the CsPbI₃ NCs without altering the NCs themselves (c.f. Figure 3.1 b and Subsection 3.1.2). As depicted in Figure 6.1 b, the GSB maximum of both, pure and blend sample, is located at the same energy of 1.85 eV¹.

In contrast to the just discussed static spectra, the temporal evolution of the spectral GSB maximum, shown in Figure 6.2 a, differs substantially for CsPbI₃ (black squares) and CsPbI₃:PCBM (orange circles). The linearly polarized DT transient of the blend decays significantly faster compared to that of pure CsPbI₃ NCs. The pronounced differences in decay dynamics are of no surprise and even intended. The decay of CsPbI₃ NCs originates solely from charge carrier recombination, while that of CsPbI₃:PCBM results from both, charge carrier recombination in CsPbI₃ NCs and electron transfer to PCBM. Clearly, the latter process occurs on a much faster time scale than the former, as it dominates the steep decay within the first 100 ps. The electron transfer process is even better resolved in Figure 6.2 b, where the difference between the CsPbI₃ and CsPbI₃:PCBM curves in a, i.e. $(\Delta T/T)_{CsPbI_3} - (\Delta T/T)_{CsPbI_3:PCBM}$, is plotted. From this, it can be inferred that the fast electron transfer process dominates the slower recombination dynamics initially and becomes insignificant at larger time delays: The initial steep rise occurs within ≈ 25 ps (best visible in the inset) and manifests that $k_{e \rightarrow PCBM} > k_{rec}$. Thereafter, data points lie horizontally, implying that electron transfer dynamics and charge carrier recombination dynamics are on par. As time progresses the magnitude of the data points declines, implying that charge carrier recombination dominates over electron transfer dynamics, rendering the latter insignificant at large time delays.

k_{rec} is determined from fitting $(\Delta T/T)_{CsPbI_3}$ with Equation 4.2, which yields $k_{rec} = 0.0040$ ps⁻¹. (This value is in good accordance with $k_{rec} = 0.0041$ ps⁻¹, extracted for the CsPbI₃ NCs sample evaluated in Chapter 4.) To determine the magnitude of $k_{e \rightarrow PCBM}$, an equation has to be found, which explains the data in Figure 6.2 b for $t \leq 100$ ps. Therefore, the spin-independent rate equations for electron and hole occupations in CsPbI₃ are formulated.

¹ The GSB maximum is slightly shifted ($\Delta_{GSB_{max}} = 0.04$ eV) with respect to that of the CsPbI₃ sample used for the experiments shown in Chapter 4 and Chapter 5. The reason for this is that the synthesis procedure, in particular the substitution process of Br with I, can lead to slightly different band gap energies. However, this is of no concern for this experiment, because both samples, CsPbI₃ and CsPbI₃:PCBM, are produced from the same batch of synthesized CsPbI₃ NCs and thus allow precise comparison between them.

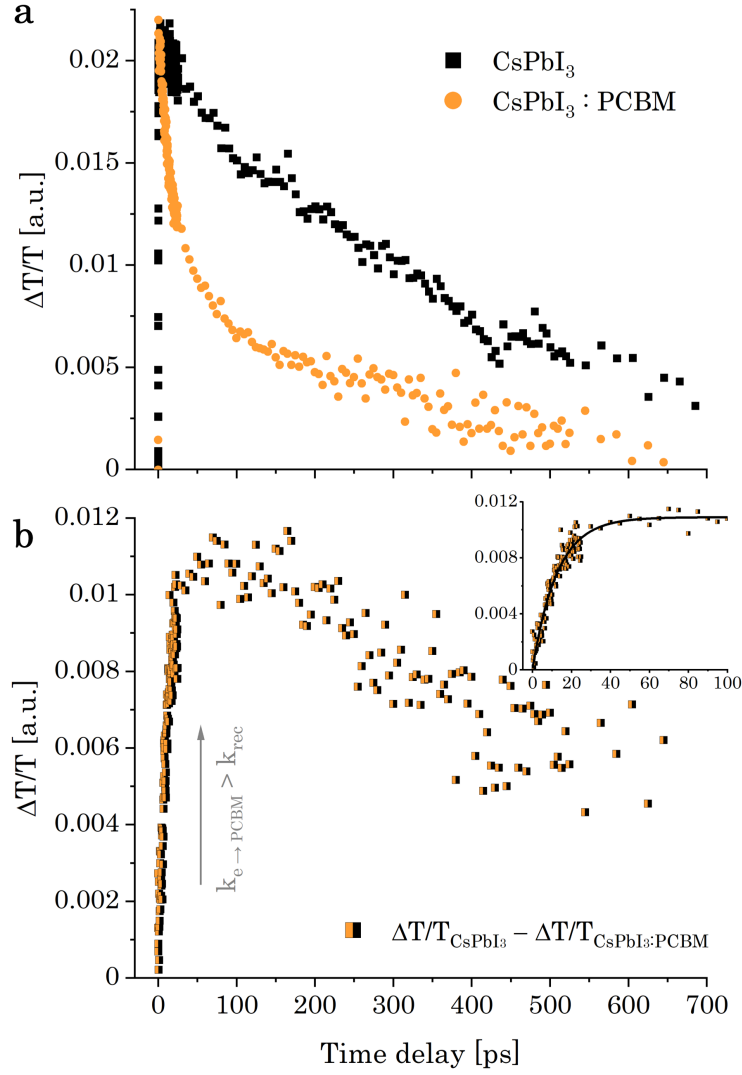


Figure 6.2: Linear polarization DT transients of pure CsPbI₃ NCs and CsPbI₃ NC:PCBM. (a) The signal decay of CsPbI₃ NCs (black squares) is significantly slower and appears to differ in functionality compared to that of CsPbI₃:PCBM (orange circles). (b) Difference between the CsPbI₃ and CsPbI₃:PCBM curves in (a), i.e. $(\Delta T/T)_{\text{CsPbI}_3} - (\Delta T/T)_{\text{CsPbI}_3:\text{PCBM}}$. The step increase within the first ≈ 25 ps is a consequence of $k_{e \rightarrow \text{PCBM}} > k_{\text{rec}}$. The data in this temporal region is shown enlarged in the inset and fitted with Equation 6.4.

$$\begin{aligned}
 \text{holes: } \dot{N}_{VB}(t) &= -k_{\text{rec}} N_{CB}(t) N_{VB}(t) \\
 \text{electrons: } \dot{N}_{CB}(t) &= -k_{\text{rec}} N_{CB}(t) N_{VB}(t) - k_{e \rightarrow \text{PCBM}} N_{CB}(t)
 \end{aligned} \tag{6.1}$$

The attempt to solve these equations leads to a second-order non-linear differential equation. I therefore make use of an approximation. Based on the above made assessment that $k_{e \rightarrow \text{PCBM}} > k_{\text{rec}}$, it is justified to take $k_{\text{rec}} \approx 0$ within the first 100 ps when electron transfer

dynamics from CsPbI₃ to PCBM dominates. With that, Equation 6.1 simplifies to

$$\begin{aligned} \text{holes: } \dot{N}_{VB} &\approx 0 \\ \text{electrons: } \dot{N}_{CB}(t) &\approx -k_{e \rightarrow PCBM} N_{CB}(t). \end{aligned} \quad (6.2)$$

From this, the linearly polarized DT decays of CsPbI₃ and CsPbI₃ : PCBM (Figure 6.2 a) can be derived.

$$\begin{aligned} N_{CsPbI_3}^{\pi \text{ polarized}} &\approx N_{balance} \\ N_{CsPbI_3:PCBM}^{\pi \text{ polarized}}(t) &\approx N_{CB}(t) + N_{VB}(t) = \frac{N_{balance}}{2} (1 + e^{-k_{e \rightarrow PCBM} t}) \end{aligned} \quad (6.3)$$

Their subtraction results in

$$N_{CsPbI_3}^{\pi \text{ polarized}} - N_{CsPbI_3:PCBM}^{\pi \text{ polarized}}(t) \approx \frac{N_{balance}}{2} (1 - e^{-k_{e \rightarrow PCBM} t}), \quad (6.4)$$

which is used to fit the data in Figure 6.2 b (inset). It fits the data well and yields $k_{e \rightarrow PCBM} \approx 0.079 \pm 0.004 \text{ ps}^{-1}$. Indeed, as predicted, this rate is much larger, i.e. ≈ 20 times, than that of charge carrier recombination, $k_{rec} = 0.0040 \text{ ps}^{-1}$. In fact, the determined value of $k_{e \rightarrow PCBM}$ is a lower bound of the electron transfer rate and might actually be even larger. The reason for this is a slower charge carrier recombination rate in CsPbI₃:PCBM compared with that in pure CsPbI₃, which is well resolved by the descending data in Figure 6.2 b from 100 ps onwards. This is a direct consequence of the scavenged electrons by PCBM, which are then missing for recombination at the band gap of CsPbI₃. Another important implication of the relatively large value of $k_{e \rightarrow PCBM}$ is that it manifests efficient electron transfer dynamics from CsPbI₃ NCs to PCBM – a prerequisite for this section's experiment. This is also supported by strong PL quenching of CsPbI₃:PCBM compared to pure CsPbI₃.¹⁵⁴ In comparison to the determined RT spin relaxation rate, $k_{e\&h} \approx 0.35 \text{ ps}^{-1}$, the electron transfer rate, $k_{e \rightarrow PCBM} \approx 0.079 \text{ ps}^{-1}$ (lower bound value) is similar, as these values differ only by a factor of ≈ 4 . This renders the CsPbI₃:PCBM material system suitable for examining electron and hole spin relaxation rates separately, which will be pursued in the following section.

6.2 Extraction of Individual Spin Relaxation Rates for Electrons and Holes

Polarization dependent DT transients were recorded for both, CsPbI₃ NCs and CsPbI₃ NC:PCBM and are shown in Figure 6.3. As before, the transients $(\Delta T/T)^{\sigma^+\sigma^+}$ and $(\Delta T/T)^{\sigma^+\sigma^-}$ are respectively coloured red and blue. Data of CsPbI₃ is displayed as squares and is in accordance with that presented in Figure 5.1². Data of CsPbI₃:PCBM is displayed as circles incorporating an orange core. Visually it clearly deviates from that of pure CsPbI₃ NCs. Evaluating both, I found that the merging dynamics of $(\Delta T/T)_{CsPbI_3}^{\sigma^+\sigma^+}$ and $(\Delta T/T)_{CsPbI_3}^{\sigma^+\sigma^-}$, as well as of $(\Delta T/T)_{CsPbI_3:PCBM}^{\sigma^+\sigma^+}$ and $(\Delta T/T)_{CsPbI_3:PCBM}^{\sigma^+\sigma^-}$ with themselves are independent of whether PCBM is present or not and complete within ≈ 10 ps.

Within the displayed 25 ps, not only $(\Delta T/T)^{\sigma^+\sigma^+}$ and $(\Delta T/T)^{\sigma^+\sigma^-}$ of both samples fully merge, but in fact, also most of the electron transfer process from CsPbI₃ NCs to PCBM takes place. There are two evidences for this:

- One, at 25 ps the decay curves $(\Delta T/T)_{CsPbI_3:PCBM}$ (independent of polarization) reach one fourth of the originally photoinduced spin polarization (SP_{max}). This indicates that the majority of CB electrons have transferred to PCBM, leaving only VB holes behind in CsPbI₃. Hence, because hole polarization has already equilibrated at that time (merging dynamics are completed), the only carriers detectable at the CsPbI₃ band gap are half of the photoexcited holes, i.e. one fourth of all initially σ^+ -polarized pump-induced charge carriers. In contrary, at 25 ps the decay curves of pure CsPbI₃, $(\Delta T/T)_{CsPbI_3}$, reach one half of the originally photoinduced spin polarization, because spin equilibrated holes (half of all initial σ^+ -induced VB holes), as well as spin equilibrated electrons (half of all initial σ^+ -induced CB electrons) are measured.
- And two, the steep increase in Figure 6.2 b saturates after ≈ 25 ps (best visible in the inset). This implies that the majority of electron transfer from CsPbI₃ NCs to PCBM takes place within this time period (c.f. discussion of Figure 6.2 b in Section 6.1).

For quantitative assessment of the transients presented in Figure 6.3, population and depopulation dynamics of the four CsPbI₃ band gap states (Figure 5.3) have to be evaluated. Upon σ^+ -excitation by the pump pulse, holes and electrons respectively populate $|\frac{1}{2}, -\frac{1}{2}\rangle_{VB}$ (in the

² Throughout this thesis, the presented absolute $\Delta T/T$ magnitudes vary to some extent for different experiments. This originates from small variabilities in optical density of the freshly prepared samples. Within one experimental study, however, it is ensured that all examined samples have consistent optical characteristics.

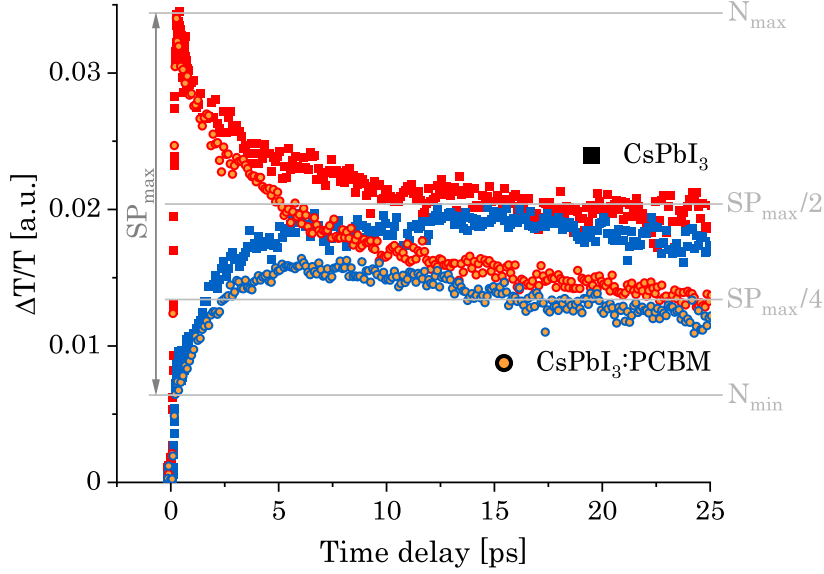


Figure 6.3: Polarization dependent DT transients of CsPbI₃ and CsPbI₃:PCBM. For both, CsPbI₃ (squares) and CsPbI₃:PCBM (circles with orange core), $(\Delta T/T)^{\sigma+\sigma+}$ (red) and $(\Delta T/T)^{\sigma+\sigma-}$ (blue) merge at ≈ 10 ps. Towards 25 ps the transients approach $\Delta T/T = (N_{max} - N_{min})/2 = N_{balance} = SP_{max}/2$ for CsPbI₃ and $\Delta T/T = (N_{max} - N_{min})/4 = SP_{max}/4$ for CsPbI₃:PCBM, as indicated in gray.

following abbreviated as $|-1/2\rangle_{VB}$) and $|1/2, +1/2\rangle_{CB}$ (in the following abbreviated as $|+1/2\rangle_{CB}$). Subsequently, in both samples, CsPbI₃ and CsPbI₃:PCBM, hole and electron populations decrease in the process of intraband spin-flipping at rates k_h and k_e , respectively, as investigated in Chapter 5. Additionally, in CsPbI₃:PCBM, CB electrons transfer to PCBM at rate $k_{e \rightarrow PCBM}$. (Recombination and any higher order relaxation mechanisms are disregarded, for the same reasons outlined in the previous chapter.) The spin-flipping processes at the band gap of pure CsPbI₃ NCs have been elaborated in Chapter 5. In contrast, in CsPbI₃:PCBM spin-flipping and transferring dynamics occur simultaneously and appropriate rate equations still need to be elaborated. I propose

$$\text{holes: } \dot{N}_{|-1/2\rangle_{VB}} = -k_h (N_{|-1/2\rangle_{VB}} - N_{|+1/2\rangle_{VB}}) \quad (6.5)$$

$$\text{electrons: } \dot{N}_{|+1/2\rangle_{CB}} = -k_e (N_{|+1/2\rangle_{CB}} - N_{|-1/2\rangle_{CB}}) - k_{e \rightarrow PCBM} N_{|+1/2\rangle_{CB}}, \quad (6.6)$$

where N denotes the time-dependent number density of holes or electrons occupying a given state. To be precise, $N = N(t)$, however, the indication of time-dependency was dropped for the purpose of clarity. Here, I have presupposed that $k_{e \rightarrow PCBM}$ is insensitive to electron spin orientation and that PCBM molecules, which merely physically attach to the CsPbI₃ NCs, do not introduce additional spin relaxation channels for photoexcited charge carriers, as there is

no evidence for this. The rate equations formulated in Equation 6.5 and Equation 6.6 describe the emptying of $|\frac{1}{2}\rangle_{VB}$ and $|\frac{1}{2}\rangle_{CB}$ states, which were initially populated by σ^+ -polarized pump excitation. They account for an ongoing spin-flipping process for as long as there exists a population imbalance between the states belonging to the same band (insured by the terms in brackets in Equation 6.5 and Equation 6.6), synonymous to Equation 5.1 and Equation 5.2. Electron transfer to the energetically favourable LUMO level of PCBM, on the other hand, continues until the total electron population is depleted (last term in Equation 6.6). Importantly, these two rate equations (Equation 6.5 and Equation 6.6) are now different for holes and electrons due to the term specifying electron transfer dynamics to PCBM. This way, hole and electron spin relaxation rates are now distinguishable. The solutions to the above formulated rate equations are

$$\text{holes: } N_{|\frac{1}{2}\rangle_{VB}} = \frac{N_{max} - N_{balance}}{2} e^{-2k_h t} + \frac{N_{balance}}{2} \quad (6.7)$$

$$\text{electrons: } N_{|\frac{1}{2}\rangle_{CB}} = \frac{N_{max} - N_{balance}}{2} e^{-(2k_e + k_{e \rightarrow PCBM})t} + \frac{N_{balance}}{2} e^{-k_{e \rightarrow PCBM}t}, \quad (6.8)$$

where it was used that the total number of holes, $N_h = N_{|\frac{1}{2}\rangle_{VB}} + N_{|\frac{1}{2}\rangle_{CB}} = N_{balance}$, is constant at all times. The total number of electrons in CsPbI₃, however, decreases due to electron transfer to PCBM and is given by

$$\begin{aligned} \dot{N}_e(t) &= -k_{e \rightarrow PCBM} N_e(t) \\ \Rightarrow N_e(t) &= N_{balance} e^{-k_{e \rightarrow PCBM}t}. \end{aligned} \quad (6.9)$$

Constants in Equation 6.7 and Equation 6.8 are fixed by demanding that

$N_{|\frac{1}{2}\rangle_{VB}}(t=0) = N_{|\frac{1}{2}\rangle_{CB}}(t=0) \stackrel{!}{=} \frac{N_{max}}{2}$, which comes from the fact that photon absorption produces a pair comprising of VB hole and CB electron and thus an equal amount of both charge carrier species.

Analogous to the calculation procedure carried out in Section 5.1, the depopulation of pump-induced hole and electron populations are jointly defined as $N^{\sigma^+\sigma^+} = N_{|\frac{1}{2}\rangle_{VB}} + N_{|\frac{1}{2}\rangle_{CB}}$, because DTS only allows for an additive measurement of hole and electron occupations (c.f. Section 3.3).

$$N^{\sigma^+\sigma^+}(t) = \frac{N_{max} - N_{balance}}{2} \left(e^{-2k_h t} + e^{-(2k_e + k_{e \rightarrow PCBM})t} \right) + \frac{N_{balance}}{2} \left(1 + e^{-k_{e \rightarrow PCBM}t} \right) \quad (6.10)$$

Simultaneously to the depopulation of initially occupied states, the initially empty states $|\frac{1}{2}\rangle_{VB}$ and $|\frac{1}{2}\rangle_{CB}$, as well as the LUMO of PCBM become occupied. Equations describing

these filling dynamics are found analogously as described in Chapter 5, i.e. essentially by replacing N_{max} by N_{min} . Other than that the solutions to the respective rate equations are the same as in Equation 6.7 and Equation 6.8. This again allows for the calculation of their combined occupation, $N^{\sigma^+\sigma^-} = N_{|+\frac{1}{2}\rangle_{VB}} + N_{|-\frac{1}{2}\rangle_{CB}}$, which results in

$$N^{\sigma^+\sigma^-}(t) = \frac{N_{min} - N_{balance}}{2} \left(e^{-2k_h t} + e^{-(2k_e + k_{e \rightarrow PCBM})t} \right) + \frac{N_{balance}}{2} \left(1 + e^{-k_{e \rightarrow PCBM}t} \right). \quad (6.11)$$

Note, that for $k_{e \rightarrow PCBM} = 0$ Equation 6.10 and Equation 6.11 respectively reduce to Equation 5.5 and Equation 5.8 calculated for pure CsPbI₃, testifying logical consistency.

Equation 6.10 and Equation 6.11 are now used to globally fit all four DT transients presented in Figure 6.3. Data and best fits (black curves) are collectively shown in Figure 6.4.

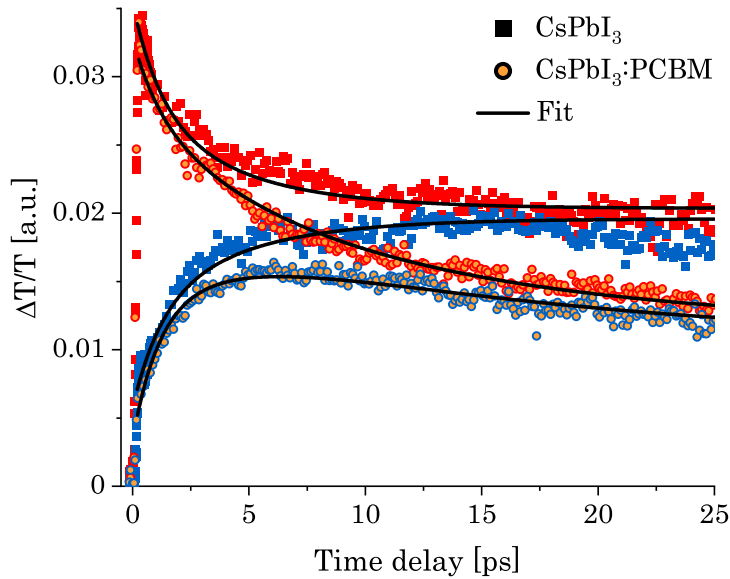


Figure 6.4: Polarization dependent DT transients of CsPbI₃ and CsPbI₃:PCBM including fitting curves. The data shown is equivalent to that already presented in Figure 6.3. It is fitted with Equation 6.10 and Equation 6.11. A global fit of all four DT transients allows for the extraction of precise k_e and k_h values.

The best global fit returns $k_e = 0.409 \pm 0.030 \text{ ps}^{-1}$ and $k_h = 0.116 \pm 0.004 \text{ ps}^{-1}$. These results suggest, that the spin flip rate of CB electrons is faster by a factor of ≈ 3.5 compared to that of VB holes. With this, electron and hole spin relaxation rates were successfully separated and assigned individual spin relaxation rates. Despite an important achievement for me and the research community, it must be pointed out, that these results are preliminary, as they

serve for proving the concept only. Dr. Amrita Dey continued to pursue this project and executed further precise measurements and data evaluation in the same manner as presented above. She obtained $k_e = 2.5 \pm 0.2 \text{ ps}^{-1}$ and $k_h = 0.200 \pm 0.003 \text{ ps}^{-1}$, which suggests the rate of electron spin relaxation to exceed that of holes by a factor of ≈ 12.5 . These results are shared with the community in our follow-up publication, which was previously released (end of 2022).¹⁵⁴

Although different in magnitude, the results of both studies testify fast electron and slow hole spin relaxation. In the following I want to comment on this and provide reasons evidencing its validity.

Considering that the CB in LHPs has p-symmetry and is strongly influenced by SOC, electrons at the band gap (R-point) occupy mixed spin states (Equation 2.13). As a consequence, electrons are expected to obey ultra fast spin randomization. This is derived from the analogy between CB states in LHPs and VB states in III-V compounds, as has been elucidated in detail in Section 2.5.^{38,105,145} Meanwhile, VB states have s-symmetry in LHPs and are thus pure in spin at the band gap (Equation 2.12). Deviating from the zone center, i.e. at $\vec{k} \neq 0$, spin up and spin down states commence to mix as a consequence of SOC. Holes in CsPbI₃ NCs are thus presumed to be subject to slow EY spin relaxation (c.f. Section 2.5). For this reason, I expect k_e to significantly exceed k_h in magnitude. To some extent, this is the case for the preliminary results, while well reflecting those published, strengthening the credibility of the latter.

An electron spin relaxation rate as fast as $k_e = 2.5 \pm 0.2 \text{ ps}^{-1}$ would imply that the measurement curves presented in Figure 5.1 and Figure 6.4 mainly show the spin equilibration dynamics of CsPbI₃ holes with only minor influence of that of electrons. The determined global spin relaxation rate, $k_{e\&h}$, would thus take a value, which is predominantly influenced by hole spin relaxation. The only slightly larger magnitude of $k_{e\&h} \approx 0.35 \text{ ps}^{-1}$ with respect to $k_h = 0.200 \pm 0.003 \text{ ps}^{-1}$ supports this hypothesis. In my first-author publication,¹¹³ $k_{e\&h}$ was attributed to EY spin relaxation. This is consistent with the presented theoretical considerations on CsPbI₃ VB holes (c.f. Section 2.5), suggesting hole spin relaxation to be governed by the EY mechanism. Hence, this is one more indication that the presented polarization dependent DT transients predominantly show spin equilibration dynamics of holes, which is governed by the EY mechanism.

CHAPTER 7

Summary and Conclusion

This thesis provides fundamental insights into charge carrier spin dynamics in colloidal CsPbI₃ perovskite nanocrystals (NCs) and the theory they are based upon. Understanding the laws of spin relaxation in lead halide perovskites (LHPs) is pivotal for their use in the future-oriented and promising field Spintronics.^{1,39} Great effort has been put in unravelling spin phenomena in LHPs by various groups contributing to forefront contemporary research.^{39,47} Nonetheless, the gained insights are still at an early stage. In particular, precise experimental investigation of spin relaxation dynamics of free, as opposed to bound charge carriers, examined in a rather undisturbed crystal environment, i.e. without the exposure to an external magnetic field, and subsequent identification of their underlying mechanisms are essential puzzle pieces urgently required but still missing. This challenge has been tackled in the scope of this thesis resulting to two major findings: One, I revealed that free charge carrier spin relaxation in CsPbI₃ NCs is governed by carrier - LO phonon scattering via the Elliott-Yafet (EY) mechanism. And two, I was able to separate electron and hole spin relaxation rates and found that electrons flip their spin polarization considerably faster than holes.

Precise measurements through Polarization Dependent Differential Transmission Spectroscopy and careful analyses of these results have been presented in two consecutive parts in this thesis.

- In the first part, I showed that an ensemble of photoexcited, free charge carriers in CsPbI₃ NCs fully equilibrate their predefined spin polarization at room temperature in ≈ 10 ps, which corresponds to a spin relaxation rate of ≈ 0.4 ps⁻¹. Towards cryogenic

temperatures, spin relaxation rates were found to vastly decrease, reaching $\approx 0.03 \text{ ps}^{-1}$ at $T \leq 50 \text{ K}$. These were fitted with diverse model calculations, revealing a clear and adequate correlation to LO phonon occupation and the EY functionality, respectively, while ruling out spin relaxation via the D'yakonov-Perel' mechanism. Moreover, spin relaxation was found to be insensitive to photoexcitation flux in the range of $2.3 \mu\text{J}/\text{cm}^2$ to $11.5 \mu\text{J}/\text{cm}^2$. Thus, Coulomb exchange interaction between electron and hole as described by the Bir-Aronov-Pikus mechanism was found unlikely to be the principal channel for spin relaxation in CsPbI₃ NCs. I found that charge carrier spin polarization decreases in the process of carrier cooling towards the band edge due to the involved enhanced LO phonon emission. In addition, I identified that increasing photoexcitation energy accelerates band edge spin relaxation, which is caused by the presence of an increased non-equilibrium LO phonon population in the crystal stemming from carrier cooling and enlarging the carrier - LO phonon scattering cross-section.

In conclusion, all results obtained in the scope of this first part of my thesis concordantly suggest that free charge carrier spin relaxation in colloidal CsPbI₃ NCs is governed by carrier - LO phonon scattering via the EY mechanism.

- With the motivation to assign individual spin relaxation rates to electrons and holes, in the second part of this thesis, I studied the physical blend CsPbI₃ NCs:PCBM. In combination, CsPbI₃ and PCBM form a type II heterojunction, such that PCBM scavenges electrons from CsPbI₃ NCs, while holes remain in the NCs. It was a novel idea and the first time to study CsPbI₃ NCs:PCBM for the mentioned purpose. Through the derivation of suitable rate equations the measured spin relaxation and electron transfer rates were fitted and evaluated. Thus, it was possible to assign individual spin relaxation rates to electrons and holes. I revealed that spin relaxation of electrons is faster than that of holes, which is in line with theoretical predictions elaborated in detail in this thesis.

All in all, these results advance the fundamental understanding of spin relaxation dynamics in CsPbI₃ perovskite NCs and provide a basis for potential strategies to engineer desired spin properties. For example, modifying phonon energies through ion exchange, pressure, or shape control of the NCs may allow the prolongation of spin relaxation time.⁴² This would enable LHPs to bring spin-based applications to the next level.

I hope that my work presented in this thesis and the corresponding publications are inspiring to the community and trigger further research in this promising and future-oriented field of research.

References

- [1] J. Puebla, J. Kim, K. Kondou, and Y. Otani. “Spintronic devices for energy-efficient data storage and energy harvesting.” In: *Communications Materials* 1.1 (2020), p. 24. DOI: <https://doi.org/10.1038/s43246-020-0022-5> (cited on pages 1, 3, 109).
- [2] X. Li and J. Yang. “First-principles design of spintronics materials.” In: *National Science Review* 3.3 (2016), pp. 365–381. DOI: [10.1093/nsr/nww026](https://doi.org/10.1093/nsr/nww026) (cited on pages 1, 2).
- [3] S. Bhatti, R. Sbiaa, A. Hirohata, H. Ohno, S. Fukami, and S.N. Piramanayagam. “Spintronics based random access memory: a review.” In: *Materials Today* 20.9 (2017), pp. 530–548. DOI: <https://doi.org/10.1016/j.mattod.2017.07.007> (cited on page 1).
- [4] A. Hoffmann and S. D. Bader. “Opportunities at the Frontiers of Spintronics.” In: *Phys. Rev. Applied* 4.4 (2015), p. 047001. DOI: [10.1103/PhysRevApplied.4.047001](https://doi.org/10.1103/PhysRevApplied.4.047001) (cited on page 1).
- [5] M. Ellis. *Gadgets and Gigawatts: Policies for Energy Efficient Electronics*. Paris: OECD/IEA, 2009 (cited on page 1).
- [6] IEA. *World Energy Outlook 2020*. Paris: IEA, 2020 (cited on page 1).
- [7] S. A. Wolf, D. D. Awschalom, R. A. Buhrman, J. M. Daughton, S. von Molnár, M. L. Roukes, A. Y. Chtchelkanova, and D. M. Treger. “Spintronics: A Spin-Based Electronics Vision for the Future.” In: *Science* 294.5546 (2001), pp. 1488–1495. DOI: [10.1126/science.1065389](https://doi.org/10.1126/science.1065389) (cited on page 1).
- [8] C. Chappert, A. Fert, and F. Nguyen van Dau. “The emergence of spin electronics in data storage.” In: *Nanoscience and Technology*, pp. 147–157. DOI: [10.1142/9789814287005_0015](https://doi.org/10.1142/9789814287005_0015) (cited on page 1).
- [9] A. Hirohata, K. Yamada, Y. Nakatani, I. Prejbeanu, B. Diény, P. Pirro, and B. Hillebrands. “Review on spintronics: Principles and device applications.” In: *Journal of Magnetism and Magnetic Materials* 509 (2020), p. 166711. DOI: <https://doi.org/10.1016/j.jmmm.2020.166711> (cited on pages 1, 2).
- [10] I. Zutic, J. Fabian, and S. Das Sarma. “Spintronics: Fundamentals and applications.” In: *Rev. Mod. Phys.* 76.2 (2004), pp. 323–410. DOI: [10.1103/RevModPhys.76.323](https://doi.org/10.1103/RevModPhys.76.323) (cited on pages 1, 2, 53, 93).
- [11] D. Awschalom and N. Samarth. “Spintronics without magnetism.” In: *Physics* 2 50 (2009). DOI: [10.1103/Physics.2.50](https://doi.org/10.1103/Physics.2.50) (cited on page 2).
- [12] Y. Huang, V. Polojärvi, S. Hiura, P. Höjer, A. Aho, R. Isoaho, T. Hakkarainen, S. Guina M. Sato, J. Takayama, A. Murayama, I. A. Buyanova, and W. M. Chen. “Room-temperature electron spin polarization exceeding 90% in an opto-spintronic semiconductor nanostructure via remote spin filtering.” In: *Nature Photonics* (2021). DOI: [10.1038/s41566-021-00786-y](https://doi.org/10.1038/s41566-021-00786-y) (cited on page 2).
- [13] B. Behin-Aein, D. Datta, S. Salahuddin, and S. Datta. “Proposal for an all-spin logic device with built-in memory.” In: *Nature Nanotechnology* 5.4 (2010), pp. 266–270. DOI: <https://doi.org/10.1038/nnano.2010.31> (cited on page 2).
- [14] D. Marković, A. Mizrahi, D. Querlioz, and J. Grollier. “Physics for neuromorphic computing.” In: *Nature Reviews Physics* 2.9 (2020), p. 499. DOI: [10.1038/s42254-020-0208-2](https://doi.org/10.1038/s42254-020-0208-2) (cited on page 2).
- [15] *The Nobel Prize in Physics 2007*. URL: <https://www.nobelprize.org/prizes/physics/2007/summary/>. (accessed: 16.05.2021) (cited on page 2).
- [16] V.I. Perel’ and B.P. Zakharchenya. “Major Physical Phenomena in the Optical Orientation and Alignment in Semiconductors.” In: *Optical Orientation*. Ed. by F. Meier and B. P. Zakharchenya. Amsterdam: North-Holland Physics Publishing, 1984. Chap. 1, 1–10 (cited on page 2).
- [17] Y. Xu, Q. Chen, C. Zhang, R. Wang, H. Wu, X. Zhang, G. Xing, W. W. Yu, X. Wang, Y. Zhang, and M. Xiao. “Two-Photon-Pumped Perovskite Semiconductor Nanocrystal Lasers.” In: *Journal of the American Chemical Society* 138.11 (2016), pp. 3761–3768. DOI: [10.1021/jacs.5b12662](https://doi.org/10.1021/jacs.5b12662) (cited on page 2).

- [18] F. Hao, C. C. Stoumpos, D. H. Cao, R. P. H. Chang, and M. G. Kanatzidis. "Lead-free solid-state organic-inorganic halide perovskite solar cells." In: *Nature Photonics* 8.6 (2014), pp. 489–494. DOI: <https://doi.org/10.1038/nphoton.2014.82> (cited on page 2).
- [19] H. Cho, S. Jeong, M. Park, Y. Kim, C. Wolf, C. Lee, J. H. Heo, A. Sadhanala, N. Myoung, S. Yoo, S. H. Im, R. H. Friend, and T. Lee. "Overcoming the electroluminescence efficiency limitations of perovskite light-emitting diodes." In: *Science* 350.6265 (2015), pp. 1222–1225. DOI: [10.1126/science.aad1818](https://doi.org/10.1126/science.aad1818) (cited on page 2).
- [20] L. Protesescu, S. Yakunin, M. I. Bodnarchuk, F. Krieg, R. Caputo, C. H. Hendon, R. X. Yang, A. Walsh, and M. V. Kovalenko. "Nanocrystals of Cesium Lead Halide Perovskites (CsPbX₃, X = Cl, Br, and I): Novel Optoelectronic Materials Showing Bright Emission with Wide Color Gamut." In: *Nano Letters* 15.6 (2015), pp. 3692–3696. DOI: [10.1021/nl5048779](https://doi.org/10.1021/nl5048779) (cited on pages 2, 7, 9, 11, 13, 14, 55, 70–72, 83).
- [21] G. Xing, N. Mathews, S. Sun, S. S. Lim, Y. M. Lam, M. Grätzel, S. Mhaisalkar, and T. C. Sum. "Long-Range Balanced Electron- and Hole-Transport Lengths in Organic-Inorganic CH₃NH₃PbI₃." In: *Science* 342.6156 (2013), pp. 344–347. DOI: [10.1126/science.1243167](https://doi.org/10.1126/science.1243167) (cited on page 2).
- [22] A. Zakutayev, C. M. Caskey, A. N. Fioretti, D. S. Ginley, J. Vidal, V. Stevanovic, E. Tea, and S. Lany. "Defect Tolerant Semiconductors for Solar Energy Conversion." In: *The Journal of Physical Chemistry Letters* 5.7 (2014), pp. 1117–1125. DOI: [10.1021/jz5001787](https://doi.org/10.1021/jz5001787) (cited on page 2).
- [23] S. De Wolf, J. Holovsky, S. Moon, P. Löper, B. Niesen, M. Ledinsky, F. Haug, J. Yum, and C. Ballif. "Organometallic Halide Perovskites: Sharp Optical Absorption Edge and Its Relation to Photovoltaic Performance." In: *The Journal of Physical Chemistry Letters* 5.6 (2014), pp. 1035–1039. DOI: [10.1021/jz500279b](https://doi.org/10.1021/jz500279b) (cited on page 2).
- [24] S. D. Stranks, G. E. Eperon, G. Grancini, C. Menelaou, M. J. P. Alcocer, T. Leijtens, L. M. Herz, A. Petrozza, and H. J. Snaith. "Electron-Hole Diffusion Lengths Exceeding 1 Micrometer in an Organometal Trihalide Perovskite Absorber." In: *Science* 342.6156 (2013), pp. 341–344. DOI: [10.1126/science.1243982](https://doi.org/10.1126/science.1243982) (cited on page 2).
- [25] Y. Tong, E. Bladt, M. F. Aygüler, A. Manzi, K. Z. Milowska, V. A. Hintermayr, P. Docampo, S. Bals, A. S. Urban, L. Polavarapu, and J. Feldmann. "Highly Luminescent Cesium Lead Halide Perovskite Nanocrystals with Tunable Composition and Thickness by Ultrasonication." In: *Angewandte Chemie International Edition* 55.44 (2016), pp. 13887–13892. DOI: <https://doi.org/10.1002/anie.201605909> (cited on pages 2, 7, 11, 12, 55, 70).
- [26] H. J. Snaith. "Present status and future prospects of perovskite photovoltaics." In: *Nature Materials* 17.5 (2018), pp. 372–376. DOI: <https://doi.org/10.1038/s41563-018-0071-z> (cited on page 2).
- [27] J. S. Manser, J. A. Christians, and P. V. Kamat. "Intriguing Optoelectronic Properties of Metal Halide Perovskites." In: *Chemical Reviews* 116.21 (2016), pp. 12956–13008. DOI: [10.1021/acs.chemrev.6b00136](https://doi.org/10.1021/acs.chemrev.6b00136) (cited on pages 2, 5, 6, 42, 77).
- [28] V. A. Hintermayr, A. F. Richter, F. Ehrat, M. Döblinger, W. Vanderlinden, J. A. Sichert, Y. Tong, L. Polavarapu, J. Feldmann, and A. S. Urban. "Tuning the Optical Properties of Perovskite Nanoplatelets through Composition and Thickness by Ligand-Assisted Exfoliation." In: *Advanced Materials* 28.43 (2016), pp. 9478–9485. DOI: <https://doi.org/10.1002/adma.201602897> (cited on pages 2, 7).
- [29] Q. A. Akkerman, V. D'Innocenzo, S. Accornero, A. Scarpellini, A. Petrozza, M. Prato, and L. Manna. "Tuning the Optical Properties of Cesium Lead Halide Perovskite Nanocrystals by Anion Exchange Reactions." In: *Journal of the American Chemical Society* 137.32 (2015), pp. 10276–10281. DOI: [10.1021/jacs.5b05602](https://doi.org/10.1021/jacs.5b05602) (cited on pages 2, 7).
- [30] J. A. Sichert, Y. Tong, N. Mutz, M. Vollmer, S. Fischer, K. Z. Milowska, R. García Cortadella, B. Nickel, C. Cardenas-Daw, J. K. Stolarczyk, A. S. Urban, and J. Feldmann. "Quantum Size Effect in Organometal Halide Perovskite Nanoplatelets." In: *Nano Letters* 15.10 (2015), pp. 6521–6527. DOI: [10.1021/acs.nanolett.5b02985](https://doi.org/10.1021/acs.nanolett.5b02985) (cited on pages 2, 7).
- [31] L. Polavarapu, B. Nickel, J. Feldmann, and A. S. Urban. "Advances in Quantum-Confined Perovskite Nanocrystals for Optoelectronics." In: *Advanced Energy Materials* 7.16 (2017), p. 1700267. DOI: <https://doi.org/10.1002/aenm.201700267> (cited on page 2).

- [32] B. J. Bohn, Y. Tong, M. Gramlich, M. L. Lai, M. Döblinger, K. Wang, R. L. Z. Hoyer, P. Müller-Buschbaum, S. D. Stranks, A. S. Urban, L. Polavarapu, and J. Feldmann. “Boosting Tunable Blue Luminescence of Halide Perovskite Nanoplatelets through Postsynthetic Surface Trap Repair.” In: *Nano Letters* 18.8 (2018), pp. 5231–5238. DOI: 10.1021/acs.nanolett.8b02190 (cited on pages 2, 7).
- [33] L. M. Herz. “Charge-Carrier Dynamics in Organic-Inorganic Metal Halide Perovskites.” In: *Annual Review of Physical Chemistry* 67.1 (2016), pp. 65–89. DOI: 10.1146/annurev-physchem-040215-112222 (cited on pages 2, 35, 36, XIII).
- [34] J. Even, L. Pedesseau, J. Jancu, and C. Katan. “Importance of Spin–Orbit Coupling in Hybrid Organic/Inorganic Perovskites for Photovoltaic Applications.” In: *The Journal of Physical Chemistry Letters* 4.17 (2013), pp. 2999–3005. DOI: 10.1021/jz401532q (cited on pages 2, 7, 13, 14, 16, 43, XIII).
- [35] M. O. Nestoklon, S. V. Goupalov, R. I. Dzhioev, O. S. Ken, V. L. Korenev, Yu. G. Kusrayev, V. F. Sapega, C. de Weerd, L. Gomez, T. Gregorkiewicz, Junhao Lin, Kazutomo Suenaga, Yasufumi Fujiwara, L. B. Matyushkin, and I. N. Yassievich. “Optical orientation and alignment of excitons in ensembles of inorganic perovskite nanocrystals.” In: *Phys. Rev. B* 97.23 (2018), p. 235304. DOI: 10.1103/PhysRevB.97.235304 (cited on page 2).
- [36] V. V. Belykh, D. R. Yakovlev, M. M. Glazov, P. S. Grigoryev, M. Hussain, J. Rautert, D. N. Dirin, M. V. Kovalenko, and M. Bayer. “Coherent spin dynamics of electrons and holes in CsPbBr₃ perovskite crystals.” In: *Nature Communications* 10.1 (2019), p. 673. DOI: <https://doi.org/10.1038/s41467-019-08625-z> (cited on pages 2, 3, 33, 45, 81, 97).
- [37] P. Lane. “Chapter 4: Spin-Polarized Spectroscopies.” In: *Ultrathin magnetic structures I. An Introduction to the Electronic, Magnetic and Structural Properties*. Ed. by J. A. C. Bland and B. Heinrich. Vol. 9. Advanced Materials. Springer Berlin, 1994, pp. 844–845. DOI: <https://doi.org/10.1002/adma.19970091020> (cited on pages 3, 33).
- [38] M. Fox. *Optical Properties of Solids*. Second. Oxford Master Series in Condensed Matter Physics. New York: Oxford University Press Inc., 2010 (cited on pages 3, 7, 16, 19–22, 24, 26, 27, 32, 33, 38, 42, 47, 48, 59–61, 63, 96, 108, XIII).
- [39] A. Privitera, M. Righetto, F. Cacialli, and M. K. Riede. “Perspectives of Organic and Perovskite-Based Spintronics.” In: *Advanced Optical Materials* (), p. 2100215 (cited on pages 3, 33, 97, 109).
- [40] J. Li and P. M. Haney. “Optical spintronics in organic-inorganic perovskite photovoltaics.” In: *Phys. Rev. B* 93.15 (2016), p. 155432. DOI: 10.1103/PhysRevB.93.155432 (cited on pages 3, 33).
- [41] J. Wang, C. Zhang, H. Liu, R. McLaughlin, Y. Zhai, S. R. Vardeny, X. Liu, S. McGill, D. Semenov, H. Guo, R. Tsuchikawa, V. V. Deshpande, D. Sun, and Z. V. Vardeny. “Spin-optoelectronic devices based on hybrid organic-inorganic trihalide perovskites.” In: *Nature Communications* 10.1 (2019), p. 129. DOI: <https://doi.org/10.1038/s41467-018-07952-x> (cited on page 3).
- [42] M. J. Crane, L. M. Jacoby, T. A. Cohen, Y. Huang, C. K. Luscombe, and D. R. Gamelin. “Coherent Spin Precession and Lifetime-Limited Spin Dephasing in CsPbBr₃ Perovskite Nanocrystals.” In: *Nano Letters* 20.12 (2020), pp. 8626–8633. DOI: 10.1021/acs.nanolett.0c03329 (cited on pages 3, 97, 110).
- [43] G. Rose. “De Perowskite, Fossili Novo.” In: *De Novis Quibusdam Fossilibus Quae In Montibus Uraliis Inveniuntur*. Berlin: typis AG Schadii, 1839, pp. 3–5 (cited on page 5).
- [44] H. L. Wells. “Über die Cäsium- und Kalium-Bleihalogenide.” In: *Zeitschrift für anorganische Chemie* 3.1 (1893), pp. 195–210. DOI: <https://doi.org/10.1002/zaac.18930030124> (cited on page 5).
- [45] C. K. Møller. “Crystal Structure and Photoconductivity of Cæsium Plumbohalides.” In: *Nature* 182.4647 (1958), p. 1436. DOI: <https://doi.org/10.1038/1821436a0> (cited on page 5).
- [46] A. Kojima, K. Teshima, Y. Shirai, and T. Miyasaka. “Organometal Halide Perovskites as Visible-Light Sensitizers for Photovoltaic Cells.” In: *Journal of the American Chemical Society* 131.17 (2009), pp. 6050–6051. DOI: 10.1021/ja809598r (cited on page 5).

- [47] A. Dey, J. Ye, A. De, E. Debroye, S. K. Ha, E. Bladt, A. S. Kshirsagar, Z. Wang, J. Yin, Y. Wang, L. N. Quan, F. Yan, M. Gao, X. Li, J. Shamsi, T. Debnath, M. Cao, M. A. Scheel, S. Kumar, J. A. Steele, M. Gerhard, L. Chouhan, K. Xu, X. Wu, Y. Li, Y. Zhang, A. Dutta, C. Han, I. Vincon, A. L. Rogach, A. Nag, A. Samanta, B. A. Korgel, C. Shih, D. R. Gamelin, D. H. Son, H. Zeng, H. Zhong, H. Sun, H. V. Demir, I. G. Scheblykin, I. Mora-Seró, J. K. Stolarczyk, J. Z. Zhang, J. Feldmann, J. Hofkens, J. M. Luther, J. Pérez-Prieto, L. Li, L. Manna, M. I. Bodnarchuk, M. V. Kovalenko, M. B. J. Roeffaers, N. Pradhan, O. F. Mohammed, O. M. Bakr, P. Yang, P. Müller-Buschbaum, P. V. Kamat, Q. Bao, Q. Zhang, R. Krahne, R. E. Galian, S. D. Stranks, S. Bals, V. Biju, W. A. Tisdale, Y. Yan, R. L. Z. Hoye, and L. Polavarapu. “State of the Art and Prospects for Halide Perovskite Nanocrystals.” In: *ACS Nano* 0.0 (0), null. doi: 10.1021/acsnano.0c08903 (cited on pages 5, 109, XIII).
- [48] T. C. Sum, M. Righetto, and S. S. Lim. “Quo vadis, perovskite emitters?” In: *The Journal of Chemical Physics* 152.13 (2020), p. 130901. doi: 10.1063/1.5132366 (cited on page 5).
- [49] R. Wang, T. Huang, J. Xue, J. Tong, K. Zhu, and Y. Yang. “Prospects for metal halide perovskite-based tandem solar cells.” In: *Nature Photonics* 15.6 (2021), pp. 411–425. doi: <https://doi.org/10.1038/s41566-021-00809-8> (cited on page 5).
- [50] Q. A. Akkerman, M. Gandini, F. Di Stasio, P. Rastogi, F. Palazon, G. Bertoni, J. M. Ball, M. Prato, A. Petrozza, and L. Manna. “Strongly emissive perovskite nanocrystal inks for high-voltage solar cells.” In: *Nature Energy* 2.2 (2016), p. 16194. doi: <https://doi.org/10.1038/nenergy.2016.194> (cited on page 5).
- [51] B. Li, Y. Zhang, L. Fu, T. Yu, S. Zhou, L. Zhang, and L. Yin. “Surface passivation engineering strategy to fully-inorganic cubic CsPbI₃ perovskites for high-performance solar cells.” In: *Nature Communications* 9.1 (2018), p. 1076. doi: <https://doi.org/10.1038/s41467-018-03169-0> (cited on page 5).
- [52] J. Chen, C. Dong, H. Idriss, O. F. Mohammed, and O. M. Bakr. “Metal Halide Perovskites for Solar-to-Chemical Fuel Conversion.” In: *Advanced Energy Materials* 10.13 (2020), p. 1902433. doi: <https://doi.org/10.1002/aenm.201902433> (cited on page 5).
- [53] C. P. Veeramalai, S. Feng, X. Zhang, S. V. N. Pammi, V. Pecunia, and C. Li. “Lead–halide perovskites for next-generation self-powered photodetectors: a comprehensive review.” In: *Photon. Res.* 9.6 (2021), pp. 968–991 (cited on page 5).
- [54] X. Yu, H. N. Tsao, Z. Zhang, and P. Gao. “Miscellaneous and Pespicious: Hybrid Halide Perovskite Materials Based Photodetectors and Sensors.” In: *Advanced Optical Materials* 8.21 (2020), p. 2001095. doi: <https://doi.org/10.1002/adom.202001095> (cited on page 5).
- [55] D. Hao, J. Zou, and J. Huang. “Recent developments in flexible photodetectors based on metal halide perovskite.” In: *InfoMat* 2.1 (2020), pp. 139–169. doi: <https://doi.org/10.1002/inf2.12053> (cited on page 5).
- [56] I. Dursun, C. Shen, M. R. Parida, J. Pan, S. P. Sarmah, D. Priante, N. Alyami, J. Liu, M. I. Saidaminov, M. S. Alias, A. L. Abdelhady, T. K. Ng, O. F. Mohammed, B. S. Ooi, and O. M. Bakr. “Perovskite Nanocrystals as a Color Converter for Visible Light Communication.” In: *ACS Photonics* 3.7 (2016), pp. 1150–1156. doi: 10.1021/acsp Photonics.6b00187 (cited on page 5).
- [57] F. Paulus, C. Tyznik, O. D. Jurchescu, and Y. Vaynzof. “Switched-On: Progress, Challenges, and Opportunities in Metal Halide Perovskite Transistors.” In: *Advanced Functional Materials* (), p. 2101029. doi: <https://doi.org/10.1002/adfm.202101029> (cited on page 5).
- [58] M. A. Becker, R. Vaxenburg, G. Nedelcu, P. C. Sercel, A. Shabaev, M. J. Mehl, J. G. Michopoulos, S. G. Lambrakos, N. Bernstein, J. L. Lyons, T. Stöferle, R. F. Mahrt, M. V. Kovalenko, D. J. Norris, G. Rainò, and A. L. Efros. “Bright triplet excitons in caesium lead halide perovskites.” In: *Nature* 553.7687 (2018), pp. 189–193. doi: 10.1038/nature25147 (cited on page 6).
- [59] S. Boyer-Richard, C. Katan, B. Traoré, R. Scholz, J. Jancu, and J. Even. “Symmetry-Based Tight Binding Modeling of Halide Perovskite Semiconductors.” In: *The Journal of Physical Chemistry Letters* 7.19 (2016), pp. 3833–3840. doi: 10.1021/acs.jpcllett.6b01749 (cited on pages 6, 14–17, 31).
- [60] J. Shamsi, A. S. Urban, M. Imran, L. De Trizio, and L. Manna. “Metal Halide Perovskite Nanocrystals: Synthesis, Post-Synthesis Modifications, and Their Optical Properties.” In: *Chemical Reviews* 119.5 (2019), pp. 3296–3348. doi: 10.1021/acs.chemrev.8b00644 (cited on pages 7, 8, 14).

- [61] K. T. Butler, J. M. Frost, and A. Walsh. “Band alignment of the hybrid halide perovskites $\text{CH}_3\text{NH}_3\text{PbCl}_3$, $\text{CH}_3\text{NH}_3\text{PbBr}_3$ and $\text{CH}_3\text{NH}_3\text{PbI}_3$.” In: *Materials Horizons* 2.2 (2015), pp. 228–231. doi: 10.1039/C4MH00174E (cited on page 7).
- [62] L. C. Schmidt, A. Pertegás, S. González-Carrero, O. Malinkiewicz, S. Agouram, G. Mínguez Espallargas, H. J. Bolink, R. E. Galian, and J. Pérez-Prieto. “Nontemplate Synthesis of $\text{CH}_3\text{NH}_3\text{PbBr}_3$ Perovskite Nanoparticles.” In: *Journal of the American Chemical Society* 136.3 (2014), pp. 850–853. doi: 10.1021/ja4109209 (cited on page 7).
- [63] F. Zhang, H. Zhong, C. Chen, X. Wu, X. Hu, H. Huang, J. Han, B. Zou, and Y. Dong. “Brightly Luminescent and Color-Tunable Colloidal $\text{CH}_3\text{NH}_3\text{PbX}_3$ (X = Br, I, Cl) Quantum Dots: Potential Alternatives for Display Technology.” In: *ACS Nano* 9.4 (2015), pp. 4533–4542. doi: 10.1021/acsnano.5b01154 (cited on page 7).
- [64] N. Droseros, G. Longo, J. C. Brauer, M. Sessolo, H. J. Bolink, and N. Banerji. “Origin of the Enhanced Photoluminescence Quantum Yield in MAPbBr_3 Perovskite with Reduced Crystal Size.” In: *ACS Energy Letters* 3.6 (2018), pp. 1458–1466. doi: 10.1021/acsenerylett.8b00475 (cited on page 7).
- [65] Y. Shi, P. Duan, S. Huo, Y. Li, and M. Liu. “Endowing Perovskite Nanocrystals with Circularly Polarized Luminescence.” In: *Advanced Materials* 30.12 (2018), p. 1705011. doi: <https://doi.org/10.1002/adma.201705011> (cited on page 7).
- [66] Y. Kim, Y. Zhai, E. A. Gaubing, S. N. Habisreutinger, T. Moot, B. A. Rosales, H. Lu, A. Hazarika, R. Brunecky, L. M. Wheeler, J. J. Berry, M. C. Beard, and J. M. Luther. “Strategies to Achieve High Circularly Polarized Luminescence from Colloidal Organic–Inorganic Hybrid Perovskite Nanocrystals.” In: *ACS Nano* 14.7 (2020), pp. 8816–8825. doi: 10.1021/acsnano.0c03418 (cited on page 7).
- [67] S. Sun, D. Yuan, Y. Xu, A. Wang, and Z. Deng. “Ligand-Mediated Synthesis of Shape-Controlled Cesium Lead Halide Perovskite Nanocrystals via Reprecipitation Process at Room Temperature.” In: *ACS Nano* 10.3 (2016), pp. 3648–3657. doi: 10.1021/acsnano.5b08193 (cited on page 7).
- [68] S. Seth and A. Samanta. “A Facile Methodology for Engineering the Morphology of CsPbX_3 Perovskite Nanocrystals under Ambient Condition.” In: *Scientific Reports* 6.1 (2016), p. 37693 (cited on page 7).
- [69] Q. A. Akkerman, S. G. Motti, A. R. Srimath Kandada, E. Mosconi, V. D’Innocenzo, G. Bertoni, S. Marras, B. A. Kamino, L. Miranda, F. De Angelis, A. Petrozza, M. Prato, and L. Manna. “Solution Synthesis Approach to Colloidal Cesium Lead Halide Perovskite Nanoplatelets with Monolayer-Level Thickness Control.” In: *Journal of the American Chemical Society* 138.3 (2016), pp. 1010–1016. doi: 10.1021/jacs.5b12124 (cited on page 7).
- [70] V. A. Hintermayr, L. Polavarapu, A. S. Urban, and J. Feldmann. “Accelerated Carrier Relaxation through Reduced Coulomb Screening in Two-Dimensional Halide Perovskite Nanoplatelets.” In: *ACS Nano* 12.10 (2018), pp. 10151–10158. doi: 10.1021/acsnano.8b05029 (cited on pages 7, 73, 74, 85, 86, 88).
- [71] M. Fox. *Optical Properties of Solids*. Second. Oxford Master Series in Condensed Matter Physics. New York: Oxford University Press Inc., 2010, pp. 141–142 (cited on pages 7, 9).
- [72] Q. Zhao, A. Hazarika, L. T. Schelhas, J. Liu, E. A. Gaubing, G. Li, M. Zhang, M. F. Toney, P. C. Sercel, and J. M. Luther. “Size-Dependent Lattice Structure and Confinement Properties in CsPbI_3 Perovskite Nanocrystals: Negative Surface Energy for Stabilization.” In: *ACS Energy Letters* 5.1 (2020), pp. 238–247. doi: 10.1021/acsenerylett.9b02395 (cited on pages 7–9, 12, 13, 70–72).
- [73] P. C. Sercel, J. L. Lyons, D. Wickramaratne, R. Vaxenburg, N. Bernstein, and A. L. Efros. “Exciton Fine Structure in Perovskite Nanocrystals.” In: *Nano Letters* 19.6 (2019), pp. 4068–4077. doi: 10.1021/acsnanolett.9b01467 (cited on pages 7–9, 14, 16, 17).
- [74] M. Fox. *Optical Properties of Solids*. Second. Oxford Master Series in Condensed Matter Physics. New York: Oxford University Press Inc., 2010, pp. 95–98 (cited on pages 9, 10).
- [75] Z. Yang, A. Surrente, K. Galkowski, A. Miyata, O. Portugall, R. J. Sutton, A. A. Haghighirad, H. J. Snaith, D. K. Maude, P. Plochocka, and R. J. Nicholas. “Impact of the Halide Cage on the Electronic Properties of Fully Inorganic Cesium Lead Halide Perovskites.” In: *ACS Energy Letters* 2.7 (2017), pp. 1621–1627. doi: 10.1021/acsenerylett.7b00416 (cited on pages 9–11, 34, 72, 89).

- [76] M. Fox. *Optical Properties of Solids*. Second. Oxford Master Series in Condensed Matter Physics. New York: Oxford University Press Inc., 2010, pp. 157–158 (cited on page 9).
- [77] H. Huang, L. Polavarapu, J. A. Sichert, A. S. Susha, A. S. Urban, and A. L. Rogach. “Colloidal lead halide perovskite nanocrystals: synthesis, optical properties and applications.” In: *NPG Asia Materials* 8.11 (2016), p. 328 (cited on page 10).
- [78] W. Shcherbakov-Wu, P. C. Sercel, F. Krieg, M. V. Kovalenko, and W. A. Tisdale. “Temperature-Independent Dielectric Constant in CsPbBr₃ Nanocrystals Revealed by Linear Absorption Spectroscopy.” In: *The Journal of Physical Chemistry Letters* 12.33 (2021), pp. 8088–8095. doi: 10.1021/acs.jpcclett.1c01822 (cited on pages 10, 34, 89).
- [79] A. Francisco-López, B. Charles, O. J. Weber, M. I. Alonso, M. Garriga, M. Campoy-Quiles, M. T. Weller, and A. R. Goñi. “Equal Footing of Thermal Expansion and Electron–Phonon Interaction in the Temperature Dependence of Lead Halide Perovskite Band Gaps.” In: *The Journal of Physical Chemistry Letters* 10.11 (2019), pp. 2971–2977. doi: 10.1021/acs.jpcclett.9b00876 (cited on pages 10, 89).
- [80] S. Singh, C. Li, F. Panzer, K. L. Narasimhan, A. Graeser, T. P. Gujar, A. Köhler, M. Thelakkat, S. Huettner, and D. Kabra. “Effect of Thermal and Structural Disorder on the Electronic Structure of Hybrid Perovskite Semiconductor CH₃NH₃PbI₃.” In: *The Journal of Physical Chemistry Letters* 7.15 (2016), pp. 3014–3021. doi: 10.1021/acs.jpcclett.6b01207 (cited on pages 10, 26, 71, 89).
- [81] J. M. Frost, K. T. Butler, F. Brivio, C. H. Hendon, M. van Schilfhaarde, and A. Walsh. “Atomistic Origins of High-Performance in Hybrid Halide Perovskite Solar Cells.” In: *Nano Letters* 14.5 (2014), pp. 2584–2590. doi: 10.1021/nl500390f (cited on pages 10, 11, 15, 89).
- [82] R. Saran, A. Heuer-Jungemann, A. G. Kanaras, and R. J. Curry. “Giant Bandgap Renormalization and Exciton–Phonon Scattering in Perovskite Nanocrystals.” In: *Advanced Optical Materials* 5.17 (2017), p. 1700231. doi: <https://doi.org/10.1002/adom.201700231> (cited on pages 10, 35, 38, 40, 53, 70, 72, 83, 85, 86, 89, 95, 96, XIII).
- [83] C. L. Davies, M. R. Filip, J. B. Patel, T. W. Crothers, C. Verdi, A. D. Wright, R. L. Milot, F. Giustino, M. B. Johnston, and L. M. Herz. “Bimolecular recombination in methylammonium lead triiodide perovskite is an inverse absorption process.” In: *Nature Communications* 9.1 (2018), p. 293. doi: 10.1038/s41467-017-02670-2 (cited on pages 10, 71, 89, XIII).
- [84] Y.P. Varshni. “Temperature dependence of the energy gap in semiconductors.” In: *Physica* 34.1 (1967), pp. 149–154. doi: [https://doi.org/10.1016/0031-8914\(67\)90062-6](https://doi.org/10.1016/0031-8914(67)90062-6) (cited on page 10).
- [85] B. J. Bohn, T. Simon, M. Gramlich, A. F. Richter, L. Polavarapu, A. S. Urban, and J. Feldmann. “Dephasing and Quantum Beating of Excitons in Methylammonium Lead Iodide Perovskite Nanoplatelets.” In: *ACS Photonics* 5.2 (2018), pp. 648–654. doi: 10.1021/acsp Photonics.7b01292 (cited on pages 10, 85).
- [86] Z. Yang, A. Surrente, K. Galkowski, N. Bruyant, D. K. Maude, A. A. Haghighirad, H. J. Snaith, P. Plochocka, and R. J. Nicholas. “Unraveling the Exciton Binding Energy and the Dielectric Constant in Single-Crystal Methylammonium Lead Triiodide Perovskite.” In: *The Journal of Physical Chemistry Letters* 8.8 (2017), pp. 1851–1855. doi: 10.1021/acs.jpcclett.7b00524 (cited on pages 10, 11, 71).
- [87] T. Baikie, Y. Fang, J. M. Kadro, M. Schreyer, F. Wei, S. G. Mhaisalkar, M. Graetzel, and T. J. White. “Synthesis and crystal chemistry of the hybrid perovskite (CH₃NH₃)PbI₃ for solid-state sensitised solar cell applications.” In: *J. Mater. Chem. A* 1 (2013), pp. 5628–5641. doi: 10.1039/c3ta10518k (cited on pages 10, 11).
- [88] A. Poglitsch and D. Weber. “Dynamic disorder in methylammoniumtrihalogenoplumbates (II) observed by millimeter-wave spectroscopy.” In: *The Journal of Chemical Physics* 87.11 (1987), pp. 6373–6378. doi: 10.1063/1.453467 (cited on page 10).
- [89] L. M. Herz. “How Lattice Dynamics Moderate the Electronic Properties of Metal-Halide Perovskites.” In: *The Journal of Physical Chemistry Letters* 9.23 (2018), pp. 6853–6863. doi: 10.1021/acs.jpcclett.8b02811 (cited on pages 10, 11, 33–35, 37, 40, 72).
- [90] J. Even, L. Pedesseau, and C. Katan. “Analysis of Multivalley and Multibandgap Absorption and Enhancement of Free Carriers Related to Exciton Screening in Hybrid Perovskites.” In: *The Journal of Physical Chemistry C* 118.22 (2014), pp. 11566–11572. doi: 10.1021/jp503337a (cited on pages 10, 11).

- [91] G. R. Berdiyrov, A. Kachmar, F. El-Mellouhi, M. A. Carignano, and M. El-Amine Madjet. "Role of Cations on the Electronic Transport and Optical Properties of Lead-Iodide Perovskites." In: *The Journal of Physical Chemistry C* 120.30 (2016), pp. 16259–16270. doi: 10.1021/acs.jpcc.6b01818 (cited on pages 10, 34).
- [92] C. C. Stoumpos and M. G. Kanatzidis. "The Renaissance of Halide Perovskites and Their Evolution as Emerging Semiconductors." In: *Accounts of Chemical Research* 48.10 (2015), pp. 2791–2802. doi: 10.1021/acs.accounts.5b00229 (cited on pages 11, 13).
- [93] R. J. Sutton, M. R. Filip, A. A. Haghighirad, N. Sakai, B. Wenger, F. Giustino, and H. J. Snaith. "Cubic or Orthorhombic? Revealing the Crystal Structure of Metastable Black-Phase CsPbI₃ by Theory and Experiment." In: *ACS Energy Letters* 3.8 (2018), pp. 1787–1794. doi: 10.1021/acsenerylett.8b00672 (cited on pages 11, 13, 89).
- [94] R. J. Sutton, G. E. Eperon, L. Miranda, E. S. Parrott, B. A. Kamino, J. B. Patel, M. T. Hörantner, M. B. Johnston, A. A. Haghighirad, D. T. Moore, and H. J. Snaith. "Bandgap-Tunable Cesium Lead Halide Perovskites with High Thermal Stability for Efficient Solar Cells." In: *Advanced Energy Materials* 6.8 (2016), p. 1502458. doi: <https://doi.org/10.1002/aenm.201502458> (cited on pages 11, 13).
- [95] C. J. Thomas, Y. Zhang, A. Guillaussier, K. Bdeir, O. F. Aly, H. G. Kim, J. Noh, L. C. Reimnitz, J. Li, F. L. Deepak, D. Smilgies, D. J. Milliron, and B. A. Korgel. "Thermal Stability of the Black Perovskite Phase in Cesium Lead Iodide Nanocrystals Under Humid Conditions." In: *Chemistry of Materials* 31.23 (2019), pp. 9750–9758. doi: 10.1021/acs.chemmater.9b03533 (cited on pages 11, 13).
- [96] M. V. Kovalenko, L. Manna, A. Cabot, Z. Hens, D. V. Talapin, C. R. Kagan, V. I. Klimov, A. L. Rogach, P. Reiss, D. J. Milliron, P. Guyot-Sionnest, G. Konstantatos, W. J. Parak, T. Hyeon, B. A. Korgel, C. B. Murray, and W. Heiss. "Prospects of Nanoscience with Nanocrystals." In: *ACS Nano* 9.2 (2015), pp. 1012–1057. doi: 10.1021/nm506223h (cited on page 12).
- [97] T. Hahn, ed. *International Tables for Crystallography Volume A: Space-Group Symmetry*. Springer 2005, 2002, pp. 720–731 (cited on page 12).
- [98] R. J. D. Tilley, ed. *Crystals and Crystal Structures*. Wiley, 2006, pp. 93–98 (cited on page 12).
- [99] Y. Tong, B. J. Bohn, E. Bladt, K. Wang, P. Müller-Buschbaum, S. Bals, A. S. Urban, L. Polavarapu, and J. Feldmann. "From Precursor Powders to CsPbX₃ Perovskite Nanowires: One-Pot Synthesis, Growth Mechanism, and Oriented Self-Assembly." In: *Angewandte Chemie International Edition* 56.44 (2017), pp. 13887–13892. doi: <https://doi.org/10.1002/anie.201707224> (cited on pages 13, 55).
- [100] A. Marronnier, G. Roma, S. Boyer-Richard, L. Pedesseau, J. Jancu, Y. Bonnassieux, C. Katan, C. C. Stoumpos, M. G. Kanatzidis, and J. Even. "Anharmonicity and Disorder in the Black Phases of Cesium Lead Iodide Used for Stable Inorganic Perovskite Solar Cells." In: *ACS Nano* 12.4 (2018), pp. 3477–3486. doi: 10.1021/acsnano.8b00267 (cited on page 13).
- [101] A. Swarnkar, A. R. Marshall, E. M. Sanehira, B. D. Chernomordik, D. T. Moore, J. A. Christians, T. Chakrabarti, and J. M. Luther. "Quantum dot-induced phase stabilization of α -CsPbI₃ perovskite for high-efficiency photovoltaics." In: *Science* 354.6308 (2016), pp. 92–95. doi: 10.1126/science.aag2700 (cited on page 13).
- [102] M. Fox. *Optical Properties of Solids*. Second. Oxford Master Series in Condensed Matter Physics. New York: Oxford University Press Inc., 2010, p. 19 (cited on page 13).
- [103] N. N. Greenwood and A. Earnshaw. *Chemistry of the Elements*. 2nd ed. Butterworth-Heinemann, Oxford, UK, 1998 (cited on page 13).
- [104] P. Y. Yu and M. Cardona. *Fundamentals of Semiconductors. Physics and Materials Properties*. 4th ed. Graduate Texts in Physics. Springer, Berlin, Heidelberg, 2010 (cited on pages 13–19, 21–26, 30, 31, 35, 37).
- [105] B. K. Ridley. *Quantum Processes in Semiconductors*. 5th ed. Oxford university press, New York, USA, 2013 (cited on pages 15–17, 24, 30, 31, 36–42, 47–53, 86, 108, XIII).
- [106] A. Banerjee and G. Paul. "Room-temperature Magnetoresistance in Hybrid Halide Perovskites: Effect of Spin-Orbit Coupling." In: *Phys. Rev. Applied* 14.6 (2020), p. 064018. doi: 10.1103/PhysRevApplied.14.064018 (cited on pages 16, 33).

- [107] G. Baym. *Lectures on Quantum Mechanics*. Westview Press, 1990 (cited on pages 16, 25–29).
- [108] R. Shankar. *Principles of Quantum Mechanics, 2nd edition*. Plenum Press, New York, 1994 (cited on page 17).
- [109] E. R. Cohen. “TABLES OF THE CLEBSCH-GORDAN COEFFICIENTS.” In: *North American Rockwell Science Center* (1974) (cited on page 17).
- [110] C. F. Klingshirn. *Semiconductor Optics*. fourth edition. Graduate Texts in Physics (GTP). Springer, 2012 (cited on page 21).
- [111] J. Singleton. *Band theory and electronic properties of solids*. Vol. 2. Oxford University Press, 2001 (cited on pages 24, 34, 35).
- [112] J. Shah. *Ultrafast Spectroscopy of Semiconductors and Semiconductor Nanostructures*. Second Enlarged Edition. Springer Series in Solid-State Sciences. Springer, Berlin, Heidelberg, 1999. doi: 10.1007/978-3-662-03770-6 (cited on pages 26, 35–38, 40, 41, 81, 83, 88).
- [113] S. Strohmair, A. Dey, Y. Tong, L. Polavarapu, B. J. Bohn, and J. Feldmann. “Spin Polarization Dynamics of Free Charge Carriers in CsPbI₃ Nanocrystals.” In: *Nano Letters* 20.7 (2020), pp. 4724–4730. doi: 10.1021/acs.nanolett.9b05325 (cited on pages 26, 33, 47, 86, 97, 108, XIII).
- [114] M. Saba, M. Cadelano, D. Marongiu, F. Chen, V. Sarritsu, N. Sestu, C. Figus, M. Aresti, R. Piras, A. Geddo Lehmann, C. Cannas, A. Musinu, F. Quochi, A. Mura, and G. Bongiovanni. “Correlated electron–hole plasma in organometal perovskites.” In: *Nature Communications* 5.1 (2014), p. 5049. doi: 10.1038/ncomms6049 (cited on pages 26, 71).
- [115] M. D. Sturge. “Optical Absorption of Gallium Arsenide between 0.6 and 2.75 eV.” In: *Phys. Rev.* 127 (3 Aug. 1962), pp. 768–773. doi: 10.1103/PhysRev.127.768 (cited on page 26).
- [116] M.I. Dyakonov and V.I. Perel’. “Theory of Optical Spin Orientation of Electrons and Nuclei in Semiconductors.” In: *Optical Orientation*. Ed. by F. Meier and B. P. Zakharchenya. Amsterdam: North-Holland Physics Publishing, 1984. Chap. 2, 11–69 (cited on page 31).
- [117] W. Zhao, R. Su, Y. Huang, J. Wu, C. F. Fong, J. Feng, and Q. Xiong. “Transient circular dichroism and exciton spin dynamics in all-inorganic halide perovskites.” In: *Nature Communications* 11.1 (2020), p. 5665. doi: 10.1038/s41467-020-19471-9 (cited on pages 33, 81, 83).
- [118] M. A. Pérez-Osorio, R. L. Milot, M. R. Filip, J. B. Patel, L. M. Herz, M. B. Johnston, and F. Giustino. “Vibrational Properties of the Organic–Inorganic Halide Perovskite CH₃NH₃PbI₃ from Theory and Experiment: Factor Group Analysis, First-Principles Calculations, and Low-Temperature Infrared Spectra.” In: *The Journal of Physical Chemistry C* 119.46 (2015), pp. 25703–25718. doi: 10.1021/acs.jpcc.5b07432 (cited on page 34).
- [119] J. Even, S. Paofai, P. Bourges, A. Letoublon, S. Cordier, O. Durand, and C. Katan. “Carrier scattering processes and low energy phonon spectroscopy in hybrid perovskites crystals.” In: *Physics, Simulation, and Photonic Engineering of Photovoltaic Devices V*. Ed. by Alexandre Freundlich, Laurent Lombez, and Masakazu Sugiyama. Vol. 9743. International Society for Optics and Photonics. SPIE, 2016, pp. 78–85. doi: 10.1117/12.2213623 (cited on page 35).
- [120] A. D. Wright, C. Verdi, R. L. Milot, G. E. Eperon, M. A. Pérez-Osorio, H. J. Snaith, F. Giustino, M. B. Johnston, and L. M. Herz. “Electron–phonon coupling in hybrid lead halide perovskites.” In: *Nature Communications* 7.1 (2016), p. 11755. doi: 10.1038/ncomms11755 (cited on pages 35, 85).
- [121] C.L. Collins and P.Y. Yu. “Generation of nonequilibrium optical phonons in GaAs and their application in studying intervalley electron-phonon scattering.” In: *Phys. Rev. B* 30.8 (1984), pp. 4501–4515 (cited on page 36).
- [122] A. Dyson and B. K. Ridley. “Spin relaxation in cubic III-V semiconductors via interaction with polar optical phonons.” In: *Phys. Rev. B* 69.12 (2004), p. 125211. doi: 10.1103/PhysRevB.69.125211 (cited on pages 36, 47, 48, 52, 53, 93, XIII).
- [123] Y. Chang, C. H. Park, and K. Matsuishi. “First-principles study of the Structural and the electronic properties of the lead-Halide-based inorganic-organic perovskites (CH₃NH₃) PbX₃ and CsPbX₃ (X= Cl, Br, I).” In: *Journal-Korean Physical Society* 44 (2004), pp. 889–893 (cited on pages 40, XIII).

- [124] M. Afsari, A. Boochani, and M. Hantezadeh. “Electronic, optical and elastic properties of cubic perovskite CsPbI₃: Using first principles study.” In: *ELSEVIER Optik* 127.23 (2016), pp. 11433–11443. DOI: <https://doi.org/10.1016/j.ijleo.2016.09.013> (cited on pages 40, XIII).
- [125] G. E. Pikus and A. N. Titkov. “Spin Relaxation under Optical Orientation in Semiconductors.” In: *Optical Orientation*. Ed. by F. Meier and B. P. Zakharchenya. Amsterdam: North-Holland Physics Publishing, 1984. Chap. 3, 73–131 (cited on pages 41, 42, 45–47, 53, 81, 93).
- [126] R. J. Elliott. “Spin-Orbit Coupling in Band Theory-Character Tables for Some Double Space Groups.” In: *Phys. Rev.* 96.2 (1954), pp. 280–287. DOI: [10.1103/PhysRev.96.280](https://doi.org/10.1103/PhysRev.96.280) (cited on page 42).
- [127] Y. Yafet. “g Factors and Spin-Lattice Relaxation of Conduction Electrons.” In: ed. by Frederick Seitz and David Turnbull. Vol. 14. *Solid State Physics*. Academic Press, 1963, pp. 1–98. DOI: [https://doi.org/10.1016/S0081-1947\(08\)60259-3](https://doi.org/10.1016/S0081-1947(08)60259-3) (cited on page 42).
- [128] M.I. D’yakonov and V.I. Perel’. In: *Sov. Phys. JETP* 33 (1971), p. 1053 (cited on page 42).
- [129] M.I. D’yakonov and V.I. Perel’. In: *Sov. Phys. JETP Lett.* 15 (1971), p. 144 (cited on page 42).
- [130] M.M. Glazov. *Electron and Nuclear Spin Dynamics in Semiconductor Nanostructures*. Oxford University Press, Oxford, UK, 2018 (cited on pages 42, 95).
- [131] G.L. Bir, A.G. Aronov, and G.E. Pikus. “Spin relaxation of electrons scattered by holes.” In: *Zh. Eksp. Teor. Fiz.* 69.4 (1975), p. 1382 (cited on pages 42, 97).
- [132] G.L. Bir, A.G. Aronov, and G.E. Pikus. “Spin relaxation of electrons due to scattering by holes.” In: *Sov. Phys. Journal of Experimental and Theoretical Physics* 42 (1976). English translation, p. 705 (cited on pages 42, 81, 97).
- [133] A. W. Overhauser. “Paramagnetic Relaxation in Metals.” In: *Phys. Rev.* 89 (4 1953), pp. 689–700. DOI: [10.1103/PhysRev.89.689](https://doi.org/10.1103/PhysRev.89.689) (cited on pages 42, 45).
- [134] D. Giovanni, H. Ma, J. Chua, M. Grätzel, R. Ramesh, S. Mhaisalkar, N. Mathews, and T. C. Sum. “Highly Spin-Polarized Carrier Dynamics and Ultralarge Photoinduced Magnetization in CH₃NH₃PbI₃ Perovskite Thin Films.” In: *Nano Letters* 15.3 (2015), pp. 1553–1558. DOI: [10.1021/nl5039314](https://doi.org/10.1021/nl5039314) (cited on pages 43–45, 90).
- [135] M. Zhou, J. S. Sarmiento, C. Fei, X. Zhang, and H. Wang. “Effect of Composition on the Spin Relaxation of Lead Halide Perovskites.” In: *The Journal of Physical Chemistry Letters* 11.4 (2020), pp. 1502–1507. DOI: [10.1021/acs.jpcclett.0c00004](https://doi.org/10.1021/acs.jpcclett.0c00004) (cited on pages 43, 44, 90).
- [136] Y. Li, X. Luo, Y. Liu, X. Lu, and K. Wu. “Size- and Composition-Dependent Exciton Spin Relaxation in Lead Halide Perovskite Quantum Dots.” In: *ACS Energy Letters* 5.5 (2020), pp. 1701–1708. DOI: [10.1021/acsenerylett.0c00525](https://doi.org/10.1021/acsenerylett.0c00525) (cited on pages 43, 44, 90).
- [137] W. Liang, Y. Li, D. Xiang, Y. Han, Q. Jiang, W. Zhang, and K. Wu. “Efficient Optical Orientation and Slow Spin Relaxation in Lead-Free CsSnBr₃ Perovskite Nanocrystals.” In: *ACS Energy Letters* 6.5 (2021), pp. 1670–1676. DOI: [10.1021/acsenerylett.1c00413](https://doi.org/10.1021/acsenerylett.1c00413) (cited on pages 43, 44).
- [138] X. Zhang, J. Shen, and C. G. Van de Walle. “First-Principles Simulation of Carrier Recombination Mechanisms in Halide Perovskites.” In: *Advanced Energy Materials* 10.13 (2020), p. 1902830. DOI: <https://doi.org/10.1002/aenm.201902830> (cited on page 43).
- [139] X. Chen, H. Lu, Z. Li, Y. Zhai, P. F. Ndione, J. J. Berry, K. Zhu, Y. Yang, and M. C. Beard. “Impact of Layer Thickness on the Charge Carrier and Spin Coherence Lifetime in Two-Dimensional Layered Perovskite Single Crystals.” In: *ACS Energy Letters* 3.9 (2018), pp. 2273–2279. DOI: [10.1021/acsenerylett.8b01315](https://doi.org/10.1021/acsenerylett.8b01315) (cited on pages 43, 44).
- [140] D. Giovanni, W. K. Chong, Y. Y. F. Liu, H. A. Dewi, T. Yin, Y. Lekina, Z. X. Shen, N. Mathews, C. K. Gan, and T. C. Sum. “Coherent Spin and Quasiparticle Dynamics in Solution-Processed Layered 2D Lead Halide Perovskites.” In: *Advanced Science* 5.10 (2018), p. 1800664. DOI: <https://doi.org/10.1002/advs.201800664> (cited on pages 43, 44, 77).

- [141] T. Inoshita and H. Sakaki. “Electron-phonon interaction and the so-called phonon bottleneck effect in semiconductor quantum dots.” In: *Physica B: Condensed Matter* 227.1 (1996). Proceedings of the Third International Symposium on New Phenomena in Mesoscopic Structures, pp. 373–377. DOI: [https://doi.org/10.1016/0921-4526\(96\)00445-0](https://doi.org/10.1016/0921-4526(96)00445-0) (cited on page 44).
- [142] J. A. Gupta, D. D. Awschalom, Al. L. Efros, and A. V. Rodina. “Spin dynamics in semiconductor nanocrystals.” In: *Phys. Rev. B* 66 (12 2002), p. 125307. DOI: [10.1103/PhysRevB.66.125307](https://doi.org/10.1103/PhysRevB.66.125307) (cited on page 45).
- [143] X. Linpeng, T. Karin, M. V. Durnev, R. Barbour, M. M. Glazov, E. Y. Sherman, S. P. Watkins, S. Seto, and K. C. Fu. “Longitudinal spin relaxation of donor-bound electrons in direct band-gap semiconductors.” In: *Phys. Rev. B* 94.12 (2016), p. 125401. DOI: [10.1103/PhysRevB.94.125401](https://doi.org/10.1103/PhysRevB.94.125401) (cited on page 45).
- [144] S. D. Stranks and P. Plochocka. “The influence of the Rashba effect.” In: *Nature Materials* 17.5 (2018), pp. 381–382. DOI: [10.1038/s41563-018-0067-8](https://doi.org/10.1038/s41563-018-0067-8) (cited on page 46).
- [145] D. Awschalom, D. Loss, and N. Samarth. *Semiconductor Spintronics and Quantum Computation*. Springer Science & Business Media, 2002 (cited on pages 47, 48, 108).
- [146] E.O. Kane. “Energy band structure in p-type germanium and silicon.” In: *Journal of Physics and Chemistry of Solids* 1.1 (1956), pp. 82–99. DOI: [https://doi.org/10.1016/0022-3697\(56\)90014-2](https://doi.org/10.1016/0022-3697(56)90014-2) (cited on page 49).
- [147] E. O. Kane. “Band structure of indium antimonide.” In: *Journal of Physics and Chemistry of Solids* 1.4 (1957), pp. 249–261. DOI: [https://doi.org/10.1016/0022-3697\(57\)90013-6](https://doi.org/10.1016/0022-3697(57)90013-6) (cited on page 49).
- [148] W. Zawadzki and W. Szymańska. “Elastic Electron Scattering in InSb-Type Semiconductors.” In: *physica status solidi (b)* 45.2 (1971), pp. 415–432. DOI: <https://doi.org/10.1002/pssb.2220450206> (cited on pages 53, 93).
- [149] S. Sun, D. Yuan, Y. Xu, A. Wang, and Z. Deng. “Ligand-Mediated Synthesis of Shape-Controlled Cesium Lead Halide Perovskite Nanocrystals via Reprecipitation Process at Room Temperature.” In: *ACS Nano* 10.3 (2016), pp. 3648–3657. DOI: [10.1021/acsnano.5b08193](https://doi.org/10.1021/acsnano.5b08193) (cited on page 55).
- [150] Merck, supplier of chemicals and services. *[6,6]-Phenyl C₆₁ butyric acid methyl ester*. <https://www.sigmaaldrich.com/DE/en/product/aldrich/684457>, visited on 05.01.2023 (cited on page 56).
- [151] Y. G. Kim, T. Kim, J. H. Oh, K. S. Choi, Y. Kim, and S. Y. Kim. “Cesium lead iodide solar cells controlled by annealing temperature.” In: *Phys. Chem. Chem. Phys.* 19.8 (2017), pp. 6257–6263. DOI: [10.1039/C6CP08177K](https://doi.org/10.1039/C6CP08177K) (cited on pages 56, 99).
- [152] M. Ye, C. He, J. Iocozzia, X. Liu, X. Cui, X. Meng, M. Rager, X. Hong, X. Liu, and Z. Lin. “Recent advances in interfacial engineering of perovskite solar cells.” In: *Journal of Physics D: Applied Physics* 50.37 (2017), p. 373002. DOI: [10.1088/1361-6463/aa7cb0](https://doi.org/10.1088/1361-6463/aa7cb0) (cited on page 56).
- [153] E. Yao, B. J. Bohn, Y. Tong, H. Huang, L. Polavarapu, and J. Feldmann. “Exciton Diffusion Lengths and Dissociation Rates in CsPbBr₃ Nanocrystal–Fullerene Composites: Layer-by-Layer versus Blend Structures.” In: *Advanced Optical Materials* 7.8 (2019), p. 1801776. DOI: <https://doi.org/10.1002/adom.201801776> (cited on page 57).
- [154] A. Dey, S. Strohmair, F. He, Q. A. Akkerman, and J. Feldmann. “Fast electron and slow hole spin relaxation in CsPbI₃ nanocrystals.” In: *Applied Physics Letters* 121.20 (2022), p. 201106. DOI: [10.1063/5.0103102](https://doi.org/10.1063/5.0103102) (cited on pages 57, 99, 103, 108).
- [155] Applied Photophysics Ltd. *User Manual Chirascan Series Spectrometers*. English. Version Document 4207Q108C03.01. 133 pp. (cited on page 60).
- [156] Inc. Thorlabs. *Mounted Achromatic Wave Plates*. https://www.thorlabs.com/newgrouppage9.cfm?objectgroup_id=854, visited on 13.01.2023 (cited on pages 60, 61).
- [157] G. Ghosh. “Dispersion-equation coefficients for the refractive index and birefringence of calcite and quartz crystals.” In: *Optics Communications* 163.1 (1999), pp. 95–102. DOI: [https://doi.org/10.1016/S0030-4018\(99\)00091-7](https://doi.org/10.1016/S0030-4018(99)00091-7) (cited on page 61).
- [158] M. Polyanskiy. *Refractive index database*. <https://refractiveindex.info/?shelf=main&book=SiO2&page=Ghosh-e>, visited on 18.01.2023 (cited on page 61).

- [159] M. J. Dodge. "Refractive properties of magnesium fluoride." In: *Appl. Opt.* 23.12 (1984), pp. 1980–1985. doi: 10.1364/AO.23.001980 (cited on page 61).
- [160] M. Polyanskiy. *Refractive index database*. <https://refractiveindex.info/?shelf=main&book=MgF2&page=Dodge-e>, visited on 18.01.2023 (cited on page 61).
- [161] Y. Yamada, T. Nakamura, M. Endo, A. Wakamiya, and Y. Kanemitsu. "Photocarrier Recombination Dynamics in Perovskite $\text{CH}_3\text{NH}_3\text{PbI}_3$ for Solar Cell Applications." In: *Journal of the American Chemical Society* 136.33 (2014), pp. 11610–11613. doi: 10.1021/ja506624n (cited on pages 73, 74).
- [162] S. Yakunin, L. Protesescu, F. Krieg, M. I. Bodnarchuk, G. Nedelcu, M. Humer, G. De Luca, M. Fiebig, W. Heiss, and M. V. Kovalenko. "Low-threshold amplified spontaneous emission and lasing from colloidal nanocrystals of caesium lead halide perovskites." In: *Nature Communications* 6.1 (2015), p. 8056. doi: 10.1038/ncomms9056 (cited on page 75).
- [163] S. Wang, J. Yu, M. Zhang, D. Chen, C. Li, R. Chen, G. Jia, A. L. Rogach, and X. Yang. "Stable, Strongly Emitting Cesium Lead Bromide Perovskite Nanorods with High Optical Gain Enabled by an Intermediate Monomer Reservoir Synthetic Strategy." In: *Nano Letters* 19.9 (2019), pp. 6315–6322. doi: 10.1021/acs.nanolett.9b02436 (cited on page 75).
- [164] Y. Yang, D. P. Ostrowski, R. M. France, K. Zhu, J. Van de Lagemaat, J. M. Luther, and M. C. Beard. "Observation of a hot-phonon bottleneck in lead-iodide perovskites." In: *Nature Photonics* 10.1 (2016), pp. 53–59. doi: 10.1038/nphoton.2015.213 (cited on pages 77, 88).
- [165] P. Odenthal, W. Talmadge, N. Gundlach, R. Wang, C. Zhang, D. Sun, Z. Yu, Z. Vally Vardeny, and Y. S. Li. "Spin-polarized exciton quantum beating in hybrid organic–inorganic perovskites." In: *Nature Physics* 13.9 (2017), pp. 894–899. doi: 10.1038/nphys4145 (cited on pages 81, 83, 90).
- [166] W. Pötz. "Hot-phonon effects in bulk GaAs." In: *Phys. Rev. B* 36 (9 1987), pp. 5016–5019. doi: 10.1103/PhysRevB.36.5016 (cited on page 88).
- [167] A. Dey, A. F. Richter, T. Debnath, H. Huang, L. Polavarapu, and J. Feldmann. "Transfer of Direct to Indirect Bound Excitons by Electron Intervalley Scattering in $\text{Cs}_2\text{AgBiBr}_6$ Double Perovskite Nanocrystals." In: *ACS Nano* 14.5 (2020), pp. 5855–5861. doi: 10.1021/acsnano.0c00997 (cited on page 89).
- [168] B. Yu, Zhang C., Chen L., Qin Z., Huang X., Wang X., and Xiao M. "Ultrafast dynamics of photoexcited carriers in perovskite semiconductor nanocrystals." In: *Nanophotonics* 10.8 (2020), pp. 1943–1965. doi: 10.1515/nanoph-2020-0681 (cited on page 97).
- [169] P. S. Grigoryev, V. V. Belykh, D. R. Yakovlev, E. Lhuillier, and M. Bayer. "Coherent Spin Dynamics of Electrons and Holes in CsPbBr_3 Colloidal Nanocrystals." In: *Nano Letters* 21.19 (2021), pp. 8481–8487. doi: 10.1021/acs.nanolett.1c03292 (cited on page 97).
- [170] E. Kirstein, N. E. Kopteva, D. R. Yakovlev, E. A. Zhukov, E. V. Kolobkova, M. S. Kuznetsova, V. V. Belykh, I. A. Yugova, M. M. Glazov, M. Bayer, and A. Greilich. "Mode locking of hole spin coherences in $\text{CsPb}(\text{Cl}, \text{Br})_3$ perovskite nanocrystals." In: *Nature Communications* 14.1 (2023), p. 699. doi: 10.1038/s41467-023-36165-0 (cited on page 97).
- [171] H. Zheng, A. Ghosh, M. J. Swamynadhan, G. Wang, Q. Zhang, X. Wu, I. Abdelwahab, W. P. D. Wong, Q.-H. Xu, S. Ghosh, J. Chen, B. J. Campbell, A. Stroppa, J. Lin, R. Mahendiran, and K. P. Loh. "Electron Spin Decoherence Dynamics in Magnetic Manganese Hybrid Organic–Inorganic Crystals: The Effect of Lattice Dimensionality." In: *Journal of the American Chemical Society* 145.33 (2023), pp. 18549–18559. doi: 10.1021/jacs.3c05503 (cited on page 97).
- [172] Z. Jin and J. Wang. "PIN architecture for ultrasensitive organic thin film photoconductors." In: *Scientific Reports* 4.1 (2014), p. 5331. doi: 10.1038/srep05331 (cited on page 101).
- [173] T. Zhuang, X. Wang, T. Sano, Z. Hong, Y. Yang, and J. Kido. "Fullerene derivatives as electron donor for organic photovoltaic cells." In: *Applied Physics Letters* 103.20 (2013), p. 203301. doi: 10.1063/1.4830037 (cited on page 101).
- [174] J. S. Blakemore. "Semiconducting and other major properties of gallium arsenide." In: *Journal of Applied Physics* 53.10 (1982), R123–R181. doi: 10.1063/1.331665 (cited on page XIII).

Appendix

A.1 Appendix A

The following values specific for GaAs and CsPbI₃ are needed for the numerical treatment of Equation 2.82 resulting in Figure 5.11. I have calculated the bottom two values, respectively, based on material specific constants known from literature.^{34,82,105,122–124,174}

$$\begin{aligned}
 \hbar\omega_{LO,GaAs} &= 36.13 \text{ meV}, \\
 W_{0,GaAs} &= 7.526 \cdot 10^{12} \text{ s}^{-1}, \\
 \left(1 - \frac{m^*_{GaAs}}{m_0}\right) \frac{\eta_{GaAs}(2 - \eta_{GaAs})}{E_{g,GaAs}(3 - \eta_{GaAs})} &= 3.037 \text{ eV}. \\
 \\
 \hbar\omega_{LO,CsPbI_3} &= 26.3 \text{ meV}, \\
 W_{0,CsPbI_3} &= 1.297 \cdot 10^{14} \text{ s}^{-1}, \\
 \left(1 - \frac{m^*_{CsPbI_3}}{m_0}\right) \frac{\eta_{CsPbI_3}(2 - \eta_{CsPbI_3})}{E_{g,CsPbI_3}(3 - \eta_{CsPbI_3})} &= 9.680 \text{ eV}. \tag{A.1}
 \end{aligned}$$

A.2 Appendix B

The imaginary part of the dielectric function, a measure of a semiconductor's optical absorption, is derived in Subsection 2.2.1 and given by Equation 2.35 and Equation 2.36. For comparison to the experiment, those equations can be transformed to $OD(\omega)$ by using Equation 3.2, and Equation 2.19-Equation 2.21. With that, the absorption spectra of ideal semiconductors may principally be plotted. However, in order to bridge the gap between theoretical prediction and modelling of experimental data, the formulas have to be slightly adjusted.

To begin with, an empirically found Urbach rule accounts for an exponential decrease in absorption below the band gap, as seen in many direct-gap semiconductors.³⁸ LHPs are no exception to this rule as evident in this and other studies on LHPs.^{33,47,83,113} The so called Urbach tail is in contrast to an abrupt absorption edge as expected from the JDOS square root dependence (Equation 2.31), as well as to the non-zero asymptotic point in absorption (Equation 2.37), which Coulomb enhanced continuum absorption converges in the limit $\hbar\omega \rightarrow E_g$. The reason for below bandgap absorption lies in impurity transitions, which smear out the theoretical predictions made for continuum absorption of an ideal semiconductor.

Urbach's rule is given by³⁸

$$\alpha_{\text{Urbach}}(\omega) \propto e^{\left(\frac{\sigma(\hbar\omega - E_g)}{k_B T}\right)}, \tag{A.2}$$

where σ represents a phenomenological fitting constant.

In order to attach the Urbach tail to the contribution of continuum absorption (Equation 2.31) two equations, adjacent to one another in energy, can be formulated

$$\begin{aligned}\alpha_{\text{Urbach}}(\hbar\omega) &= A_u e^{\left(\frac{\sigma(\hbar\omega - E_g)}{k_B T}\right)} && \text{for } \hbar\omega < E_m, \\ \alpha_{\text{continuum}}(\hbar\omega) &= A_c \sqrt{\hbar\omega - E_g} + \text{offset}_m && \text{for } \hbar\omega > E_m.\end{aligned}\quad (\text{A.3})$$

A_c , A_u and offset_m are parameters, whereof the latter two will be fixed in the next steps through appropriate boundary conditions. The energy at which the two equations merge continuously and continuously differentiable is denoted as E_m , with $E_m \geq E_g$.

A continuous curve is assured by demanding

$$\alpha_{\text{Urbach}}(\hbar\omega = E_m) \stackrel{!}{=} \alpha_{\text{continuum}}(\hbar\omega = E_m). \quad (\text{A.4})$$

With this the parameter offset_m is fixed

$$\text{offset}_m = A_c \left(\frac{k_B T}{2\sigma\sqrt{E_m - E_g}} - \sqrt{E_m - E_g} \right). \quad (\text{A.5})$$

A smooth transition between the two functions is assured by demanding continuous differentiability, i.e.

$$\left. \frac{d\alpha_{\text{Urbach}}(\hbar\omega)}{d(\hbar\omega)} \right|_{\hbar\omega=E_m} \stackrel{!}{=} \left. \frac{d\alpha_{\text{continuum}}(\hbar\omega)}{d(\hbar\omega)} \right|_{\hbar\omega=E_m} \quad (\text{A.6})$$

Thus, an expression for A_u is obtained and reads

$$A_u = A_c \frac{k_B T}{2\sigma\sqrt{E_m - E_g}} e^{-\left(\frac{\sigma(E_m - E_g)}{k_B T}\right)} \quad (\text{A.7})$$

The expression for excitonic bound state absorption (Equation 2.35) is

$$\alpha(\omega) = g_o + A_X \frac{Ry_X^{3/2}}{\omega^2} \sum_{n=1}^{\infty} \frac{1}{n^3} \delta\left(\hbar\omega - E_g + \frac{Ry_X}{n^2}\right), \quad (\text{A.8})$$

where g_o is a global offset, caused by surface reflection and scattering processes in the semiconductor layer during the measurement and A_X is a proportionality factor, which comprises of the pre-factor of Equation 2.35, including the conversion of $1/a_X^3$ to $Ry_X^{3/2}$.

The δ -function in Equation A.8, representing the exciton bound states, is approximated through

$$\delta(x) = \lim_{\Gamma \rightarrow \infty} \frac{1}{2\Gamma \cosh^2\left(\frac{x}{\Gamma}\right)}, \quad (\text{A.9})$$

where Γ is a broadening parameter, allowing excitonic states to have a finite width in energy.

By combining the expressions for the Urbach tail, continuum absorption and excitonic bound state absorption I find the final expression for modelling my experimental absorption data

$$\alpha(\omega) = g_o + A_X \frac{Ry_X^{3/2}}{\omega^2} \sum_{n=1}^{\infty} \frac{1}{n^3} \frac{1}{2\Gamma \cosh^2\left(\frac{\hbar\omega - E_g + Ry_X/n^2}{\Gamma}\right)} + \begin{cases} A_u e^{\left(\frac{\sigma(\hbar\omega - E_g)}{k_B T}\right)} & \text{for } \hbar\omega < E_m \\ A_c \sqrt{\hbar\omega - E_g} + \text{offset}_m & \text{for } \hbar\omega > E_m \end{cases} \quad (\text{A.10})$$

The parameters offset_m and A_u have been found above through the aid of appropriate boundary conditions and are given in Equation A.5 and Equation A.7, respectively.

List of Figures

2.1	Cubic APbX ₃	6
2.2	Visualization of the outermost s- and p-orbitals of neighbouring Pb and I atoms in CsPbI ₃	15
2.3	Comparison of the band structures and optical transitions in II-VI or III-V semiconductors and LHPs.	18
2.4	Surface and interior optical effects occurring upon light-matter interaction.	19
2.5	Optical transitions at the CsPbI ₃ band gap.	30
2.6	The process of carrier cooling according to the phonon-cascade model represented by one phonon emission event in a parabolic CB. ^{105,112}	37
2.7	Bose-Einstein distribution function plotted against temperature.	38
2.8	LO phonon scattering rate versus carrier energy.	40
3.1	Combination of CsPbI ₃ and PCBM.	57
3.2	Effect of a quarter wave plate on the electric field vector of EM radiation.	61
3.3	Laser pulse sequence in DTS.	63
3.4	DTS setup including alterations allowing for polarization dependent experiments.	67
4.1	HAADF-STEM images of the CsPbI ₃ NCs prepared and investigated in the scope of this thesis.	69
4.2	Static absorption and PL spectra of CsPbI ₃ NCs.	70
4.3	Temperature dependent static absorption spectra of CsPbI ₃ NCs.	71
4.4	CD spectrum of CsPbI ₃ NCs.	73
4.5	Charge carrier recombination dynamics in CsPbI ₃ NCs at RT.	74
5.1	Polarization dependent DT spectra and corresponding transients of CsPbI ₃ NCs at RT.	76
5.2	Photoinduced optical transitions at the LHP band gap in polarization dependent DTS.	78
5.3	Induced optical transitions at the band gap during polarization dependent DTS including intraband spin-flip transition rates.	78
5.4	Polarization dependent DT transients fitted.	81

5.5	Spin relaxation rates obtained from DTS with various photoexcitation intensities.	82
5.6	Photoexcitation energy and polarization dependent DTS.	84
5.7	Evaluation and interpretation of photoexcitation energy dependent DT transients.	85
5.8	Influence of excess photoexcitation energy on spin relaxation rate.	88
5.9	Spin polarization decay at 50 K and 250 K.	91
5.10	Spin relaxation rates versus temperature including theoretical model predictions.	92
5.11	Numerically generated EY spin relaxation rate.	94
5.12	Incapability of the DP mechanism to describe the measured spin relaxation rates.	95
5.13	Linear spin polarization decay occurring in the temporal regime $t \lesssim 3$ ps and for temperatures $T=4$ K, 25 K and 50 K.	96
6.1	Static absorption and DT spectra of pure CsPbI ₃ NCs and the CsPbI ₃ NC:PCBM blend.	100
6.2	Linear polarization DT transients of pure CsPbI ₃ NCs and CsPbI ₃ NC:PCBM.	102
6.3	Polarization dependent DT transients of CsPbI ₃ and CsPbI ₃ :PCBM.	105
6.4	Polarization dependent DT transients of CsPbI ₃ and CsPbI ₃ :PCBM including fitting curves.	107

List of Tables

- 2.1 Various types of polarization and corresponding relative amplitudes and phases. 27
- 2.2 Momentum and energy conservation in a carrier - LO phonon scattering event.¹⁰⁵ 36

List of Abbreviations

ADP	acoustic phonon deformation potential scattering
BAP	Bir-Aronov-Pikus
CB	conduction band
CD	circular dichroism
CEF	Coulomb enhancement factor
CPL	circular photoluminescence
DP	D'yakonov-Perel'
DTS	differential transmission spectroscopy
EM	electromagnetic
ESR	electron spin resonance
EY	Elliott-Yafet
GMR	giant magnetoresistance
GSB	ground state bleach
GT	Glan-Thompson polarizing prism
HAADF-STEM	high-angle annular dark-field scanning transmission electron microscopy
HH	heavy hole
HOMO	highest occupied molecular orbital
JDOS	joint density of doubly spin degenerate CB and VB states
L-CPL	left-handed circularly polarised light
LED	light-emitting diode
LH	light hole
LHP NCs	lead (tri-) halide perovskite nanocrystals
LO	longitudinal optical
LUMO	lowest unoccupied molecular orbital
MHP	metal trihalide perovskite
ND	neutral density
OD	optical density
OPA	optical parametric amplifier
PEM	photo-elastic modulator

PL	photoluminescence
PLQY	photoluminescence quantum yield
QW	quantum well
R-CPL	right-handed circularly polarised light
SOC	spin-orbit coupling
VB	valence band
WL	white light

Acknowledgments

At this point I want to acknowledge all, who have cooperated and accompanied me during my time as a PhD student at the Chair for Photonics and Optoelectronics.

Thank you,

Prof. Dr. Jochen Feldmann, for giving me the opportunity to do my PhD at your great chair and for your guidance and support during this time. Getting the chance to contribute to cutting-edge research by using the best research equipment and cutting-edge experimental setups was a great honour to me. The participation at various high-level conferences allowed me to develop professionally, as well as personally. Thank you!

Dr. Lakshminarayana Polavarapu, for your guidance in the preparation of perovskites and your supervision in the chemistry lab. The synthesis of highly functional perovskite nanocrystals was thanks to your profound knowledge and long-term experience.

Prof. Dr. Jacek Stolarczyk, for welcoming me warmly by integrating me in your group-meetings and for the insights into photocatalysis during my first months at the chair. I very much enjoyed your good mood and positive attitude whenever I talked to you.

PD Dr. Theobald Lohmüller, for the positive atmosphere you created in every room you that you entered. Your confident appearance and optimistic and entertaining way of communicating inspired me.

Dr. Amrita Dey, for the great collaboration, the valuable exchange of project-related experiences and your constructive feedback, which I could always rely on. I enjoyed having you as a colleague and friend.

Dr. Bernhard Bohn, for being awesome. You were my role model, my shield, and my advisor, which enhanced my life and work as a PhD student immensely. Thank you for being so lovely and caring.

Dr. Sebastian Rieger, for being the best office companion I could have wished for not least because of your cheerful and honest personality. You never stopped believing in my capabilities, you gave me a push when I needed it and you were always a great team mate in good and bad times. I am happy to have you as a friend.

Ilka Vinçon, for becoming my “chirality-companion”. I learned a lot from our knowledge exchange on circular polarization of laser light and from installing and testing the polarization detector. I am grateful that you shared your chemistry wisdom with me, whenever I had a

question.

to **all colleagues** at the Chair for Photonics and Optoelectronics for being part of the experiences during our time at the Nano-Institute, conferences, or lunch breaks, **Dr. Aurora Manzi, Dr. Alexander Richter, Dr. Nicola Kerschbaumer, Francis Schuknecht, Dr. Yu Tong, Dr. Stefanie Pritzl, Dr. Jiawen Fang, Dr. Yiou Wang, Dr. Tushar Debnath, Mariam Kurashvili, Anja Barfuß**er, and many more.

Gerlinde Adam, for loving us students. Talking to you was always a pleasure to me. I am very thankful for your help with administrative inquiries of all kinds.

Stefan Niedermaier, for helping me out whenever any technical problem arose. You seemed to always find a practical approach to all kinds of demands, which gave me a sense of safety.

Talee Barghouti, for your openness and kindness. I always felt welcome to ask any question regarding chemistry or laboratory equipment.

Dr. Max Warkentin, for more than words would allow me to say. Briefly, I am deeply grateful for you being part of my life, for your love and kindness, for being always there for me, for your brightness and for your personal and professional advices.

Philina for freeing my mind and for forcing me to leave my laptop. Your wonderfulness consistently reminded me of the true priorities in life.

Mama, Omi and Opi, for being always there for us in every regard. The time you gave me to pursue my PhD is invaluable.

